university of groningen / faculty of science and engineering

University of Groningen, Groningen

Faculty of science and engineering

Numerical investigation of the survival of cold gas clouds in low-redshift early-type galaxies

Master Thesis

Author:
Mark van der Keijl (S3201554)

Supervisors:
Prof. Dr. Filippo Fraternali
Dr. Asger Grønnow
Andrea Afruni

June 30, 2021

Abstract

Cold ($T \sim 10^4\,\mathrm{K}$) gas residing in the multiphase circumgalactic medium of galaxies plays an important role in sustaining star formation. For a long time, it was believed that passive galaxies were devoid of any cold gas, which would account for their lack of star formation activity. Relatively recent observations have, however, shown that ionized cold gas in the form of clouds do, in fact, also inhabit the halo regions of quiescent early-type galaxies (ETGs). Where this cold gas comes from and why it does not feed star formation is not fully understood. Recently, Afruni et al. 2019 have shown, with the help of a semi-analytical model, that this cold medium might be part of the accretion from the intergalactic medium (IGM) and have suggested that the clouds evaporate in the hot ($T \sim 10^{6-7}\mathrm{K}$) corona before reaching the inner regions of the galaxy. Yet, this evaporation occurs mainly via hydrodynamical instabilities that this analytical model cannot fully describe. To that end, we carry out 2D hydrodynamical simulations that include radiative cooling and thermal conduction to investigate the evolution of cold clouds travelling through a hot medium, which we then compare with the analytical model. Key parameters that we vary in our simulations are the suppression factor (f) for isotropic thermal conduction, the cloud metallicity, the cloud mass, and the radius at which the cloud starts its infall.

In accordance with the analytical model, we find that the clouds in all our simulations evaporate in the hot medium long before they could potentially feed star formation, with, on average, a survival time of $\bar{t} = 643\,\mathrm{Myr}$ and a travelled distance of $\bar{d} = 63\,\mathrm{kpc}$. We furthermore show that the cold gas mass is not lost at a constant exponential rate as assumed by the analytical model, but, rather, at an exponential rate that steepens over time until the mass loss becomes seemingly instantaneous. This final, catastrophic mass loss phase occurs close to the end of the cloud's lifetime, i.e. once $\sim 80\%$ of the initial cold mass has already been lost. We also find that the cloud becomes highly elongated in the transverse direction as it falls inwards to the galaxy. This is in disagreement with the analytical model, which assumes that the cloud will contract while retaining its spherical shape. Finally, we find a good agreement between the numerical and analytical velocity profiles suggesting that, despite all the approximations, the kinematics of the clouds is well described by the analytical model.

Contents

Chapter 1

Introduction

Galaxies can be categorized into two main types — early-type galaxies (ETGs) and late-type galaxies (LTGs; Hubble 1936). ETGs are spheroidal, almost featureless galaxies that predominately contain old stars and tend to reside in dense clusters of galaxies. They are characterized by a lack of ongoing star formation and are therefore often labeled as *passive* or *quiescent* galaxies. The formation history of these galaxies is believed to consist of two phases: an initial phase of rapid in-situ star formation followed by an assembly of stars that formed ex-situ. During the in-situ star formation phase, ETGs were actively accreting gas which presumably also powered the active galactic nucleus (AGN) that some ETGs host in their galactic center (Cimatti et al. 2019). LTGs, on the other hand, are quite different: they inhabit regions that are less densely packed with galaxies and have a more distinctive shape in the form of spiral arms and a central bulge. These galaxies are still actively forming stars (mainly in the spiral arms) and are therefore known as *star-forming galaxies* (Binney and Merrifield 1998; Sparke and Gallagher 2007). Their formation history is characterized by a slower rate of in-situ star formation than ETGs, which is produced by a dissipative infall of gas. Due to the conservation of angular momentum, a rotationally supported disk forms, which may eventually evolve into an LTG (Mo et al. 2010; Pillepich et al. 2015).

Even though LTGs and ETGs follow different evolutionary paths, they both initially formed in a dark matter (DM) halo which had started to attract baryonic matter (i.e. gas) after the epoch of Recombination (Ryden 2016). The amount of baryonic matter relative to the total (baryonic + dark) matter in the Universe is known as the *cosmic baryon fraction*, $f_{\rm b} \simeq 0.16$, and is one of the most well-constrained parameters in Cosmology (Planck Collaboration et al. 2020). Based on this parameter and on the assumption that galaxies accrete all the gas within their DM halos, one would expect the total baryonic mass in galaxies to be simply $M_{\rm b} = f_{\rm b} M_{\rm halo}$. However, observations have indicated that over a wide range of galaxy masses, the baryonic mass is well below $f_{\rm b} M_{\rm halo}$. A considerable portion of the expected baryons are therefore missing (e.g. McGaugh et al. 2010). Where exactly these missing baryons are is an open question, but it is generally believed that they must reside in two media: the *intergalactic medium* (IGM; Danforth and Shull 2005) and the *circumgalactic medium* (CGM; Cimatti et al. 2019). The IGM resides in between the galaxies, while the CGM is a multiphase medium that surrounds every galaxy out to roughly its halo virial radius. The CGM is intimately linked with the IGM from which it can accrete low-metallicity gas. If this gas is able to remain cool (or to cool down) and reach the inner regions of the galaxy, star formation will ensue (as is the case for LTGs). The CGM is therefore believed to play a key role in the evolution of galaxies as it regulates the galaxy's gas supply and fuels star formation with cold gas (Tumlinson et al. 2017).

This chapter is organized as follows. In section 1.1, we introduce the various gas phases

that constitute the CGM; in section 1.2, we explain the perceived dynamics of the CGM; in section 1.3, we describe the interactions that can arise between the hot and cold phase of the CGM in ETGs; in section 1.4, we introduce an analytical model which invokes these interactions to account for the lack of star formation in ETGs; and in section 1.5, we explain the aim of this research.

1.1 The circumgalactic medium

The existence of the CGM residing in the halo regions of both ETGs and LTGs has been shown by observations in emission and absorption ranging from X-ray (Anderson et al. 2013; Li et al. 2017; Li et al. 2018) to UV-optical bands (Bordoloi et al. 2011; Keeney et al. 2013; Kacprzak et al. 2014; Borthakur et al. 2015). The CGM comprises three phases based on its temperature: the cold/cool ($T < 10^5$ K), hot ($T \sim 10^{6-7}$K), and intermediate warm ($T \sim 10^{5-6}$K) phase.

1.1.1 Cold phase

The cold phase of the CGM comes in two forms: *neutral* and *ionized*. The neutral gas manifests itself as extra-planar cold gas which has been extensively observed, through 21-cm emission lines, around both the Milky Way and other nearby spiral galaxies (e.g. Marasco et al. 2019). This extra-planar cold gas has been observed as a gaseous halo that surrounds the galactic plane (see the left panel of Figure 1.1) and which exhibits a regular, differential rotation that lags with respect to that of the disk (Oosterloo et al. 2007). In the Milky Way, this neutral (H I) cold gas has also been detected in the form of clouds that reside within ~ 10 kpc of the Galactic plane (Sancisi et al. 2008; Wakker et al. 2008; Fraternali et al. 2015). These clouds move at velocities that deviate from the galactic rotation (Wakker and van Woerden 1997) of which we distinguish two types: Intermediate-Velocity-Clouds (IVCs), which move at velocities $30\,\mathrm{km/s} < |V_{\mathrm{LSR}}| < 90\,\mathrm{km/s}$ relative to the Local Standard of Rest (LSR), and High-Velocity-Clouds (HVCs; Muller et al. 1963), which move at higher velocities of $|V_{\mathrm{LSR}}| > 90\,\mathrm{km/s}$ (Wakker 1990). The accretion of this extra-planar H I gas is considered a contributor to the fuelling of star formation in our Milky Way and other star-forming galaxies.

Observations from Hα emissions have shown that also ionized cold gas can reside close to the galactic plane of disk galaxies. This gas, known as diffuse ionized gas (DIG), is seen in both the Milky Way and other nearby spiral galaxies and is believed to be the ionized part of the neutral extra-planar gas (e.g. Fraternali et al. 2004; Putman et al. 2012; Li et al. 2021). However, ionized cold gas with a significantly lower density has also been observed to reside at much larger distances (~ 100 kpc) from the galactic plane (Tumlinson et al. 2017). This low-density, ionized gas was first discovered by Boksenberg and Sargent 1978 and Bergeron 1986 via detections of absorption lines in the UV and in the optical from spectra of background quasars. More recent absorption-line studies have furthermore shown that this ionized cold gas is not one homogeneous medium, but an ensemble of various absorbing clouds that move at different velocities and are bound to their host galaxies (e.g. Werk et al. 2013; Tumlinson et al. 2013; Werk et al. 2014). What is even more surprising is that these cold ionized clouds not only inhabit the halo regions of LTGs but also of ETGs (see the right panel of Figure 1.1), as evidenced by observations of H I (Thom et al. 2012; Chen et al. 2018), Mg II and other low-ionization absorption lines (Gauthier et al. 2009; Huang et al. 2016; Huang et al. 2021). In fact, Thom et al. 2012 studied 16 (low-redshift) ETGs in the COS-Halos Survey (Tumlinson et al. 2013) and found that the Lyman-α absorption lines around ETGs are about as strong and frequent as around star-forming galaxies. These lines trace the neutral fraction of a largely photo-ionized medium. Using the CLOUDY

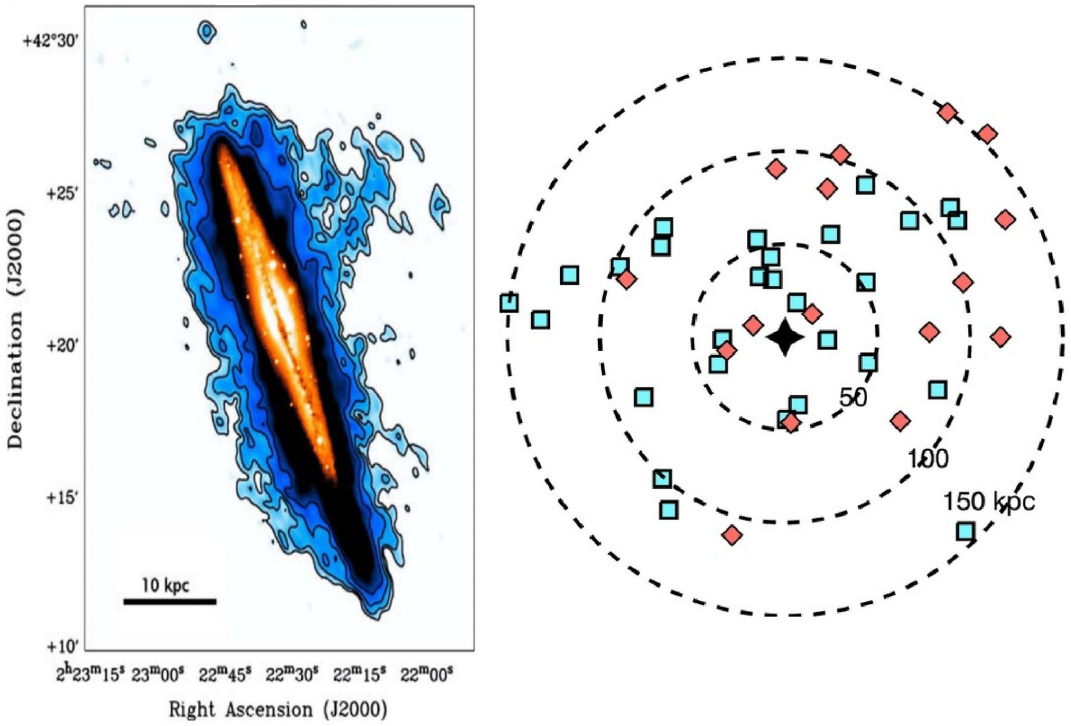

Figure 1.1: *Left:* Total H I map (blue) around the edge-on galaxy NGC 891 (orange) indicating the presence of (extra-planar) neutral cold CGM gas (Oosterloo et al. 2007; Sancisi et al. 2008). *Right:* QSO absorption line detections of ionized cold gas located at large distances from the galaxy (up to 150 kpc). The blue and red dots represent LTGs and ETGs, respectively (Tumlinson et al. 2013).

photo-ionization model (Ferland et al. 1998), they estimated the ionization fraction of the cold gas from which they inferred that the ETGs should have a total (neutral + ionized) cold gas mass of roughly $10^{9-11}\mathrm{M}_{\odot}$. These large uncertainties in the total mass of the cold gas is due to the fact that photo-ionization models are very sensitive to model assumptions.

In a more recent paper, Zahedy et al. 2019 investigated (using data from a COS-LRG sample; Chen et al. 2018) the cool CGM around 16 luminous red galaxies (LRGs) at $z = 0.21 - 0.55$ with stellar masses of $M_{\mathrm{star}} > 10^{11}\,\mathrm{M}_{\odot}$. They found an average temperature of $T \sim 10^{4}\,\mathrm{K}$ and a cool gas mass of $M_{\mathrm{cool}} = (1-2) \times 10^{10}\,\mathrm{M}_{\odot}$ within a projected distance of $d < 160\,\mathrm{kpc}$. They also reported large uncertainties for the (column) density and metallicity of the cold gas obtained with the CLOUDY model.

1.1.2 Hot phase

The existence of the hot CGM ($T \sim 10^{6-7}$ K), also known as the galaxy *corona*, was predicted by L. Spitzer based on the observations of cold ($T < 10^{5}\,\mathrm{K}$), dense pockets of H I gas residing within $\sim 1\,\mathrm{kpc}$ above the disk of our Milky Way (Spitzer 1956). Spitzer argued that these cold clouds could only survive if they were in pressure equilibrium with a surrounding hot, ionized and diffuse medium (see Figure 1.2). This hot surrounding medium is believed to form naturally around growing galaxies as inflowing IGM gas gets shock-heated to the virial temperature (White and Rees 1978; White and Frenk 1991; Birnboim and Dekel 2003). Unfortunately, the hot CGM is notoriously difficult to detect as its extremely low density ($n \sim 10^{-4}\,\mathrm{cm}^{-3}$ for spiral galaxies; Pezzulli et al. 2017) leads to a very low X-ray surface brightness (e.g. Bregman 2007). Nevertheless, its existence has been established via the detection of soft X-ray emission (e.g.

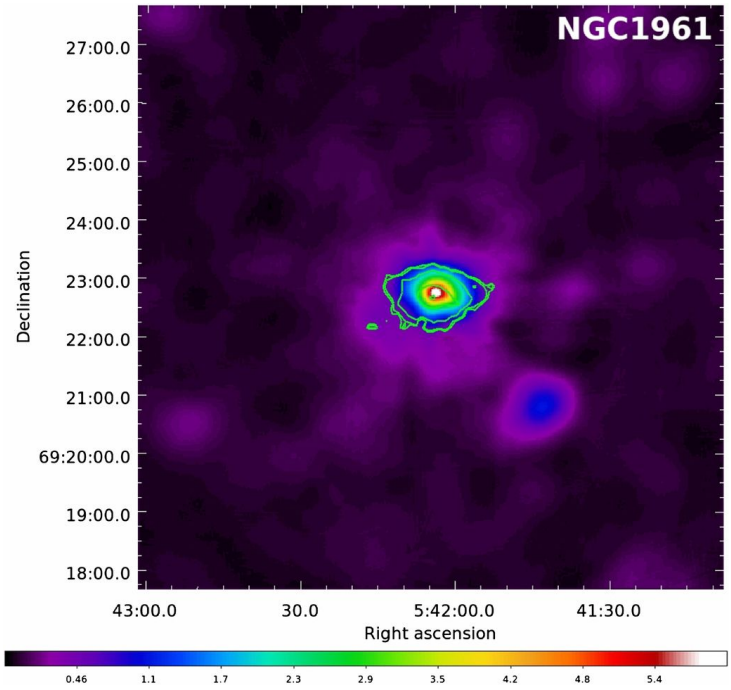

Figure 1.2: X-ray detection of a hot, diffuse medium (in purple) surrounding NGC 1961. The green contour lines represent the K-band intensity levels which have been overplotted to illustrate the extent and distribution of the stellar light (Bogdán et al. 2013).

Anderson and Bregman 2010; Anderson et al. 2013) and absorption-lines along QSO sightlines (e.g. Williams et al. 2005; Gupta et al. 2012). These detections are also supported by ΛCDM cosmological simulations, which have shown that hot coronal media are consistently formed within DM halos (e.g. Fumagalli et al. 2014; Fielding et al. 2017).

When a cold cloud, like an HVC, moves through and interacts with the surrounding hot medium, it may also lead to the creation of a mixed, intermediate warm phase ($T \sim 10^{5-6}$ K). The occurrence of this mixed gas has been testified by hydrodynamical simulations (e.g. Suresh et al. 2017) as well as by observations of UV absorption lines via ions such as O VI, C IV, and N V in both the Milky Way and external galaxies (e.g. Tumlinson et al. 2011; Werk et al. 2016).

An important difference between the cold and hot component is that only cold gas can flow to the inner regions of a galaxy and feed star formation. The hot corona, on the other hand, remains (approximately) in hydrostatic equilibrium with the galactic potential and will therefore, provided that it has a long cooling time, not accrete onto the galaxy (Spitzer 1956; Fang et al. 2013).

1.2 Dynamics of the CGM

Galaxies evolve by accreting gas from its surroundings which is slowly converted into stars. How exactly galaxies accrete their gas is still under debate, but, in general, we distinguish between two main ways: *hot mode* and *cold mode* accretion (Birnboim and Dekel 2003; Kereš et al. 2005; Dekel and Birnboim 2006; Stern et al. 2020). During hot mode accretion, inflowing IGM gas gets shock-heated to the virial temperature and forms an atmosphere in nearly hydrostatic equilibrium that can eventually slowly cool down in the central regions, if the cooling time is short enough. During cold mode accretion, cold gas is directly fed to the galaxy via filaments (from the IGM) without

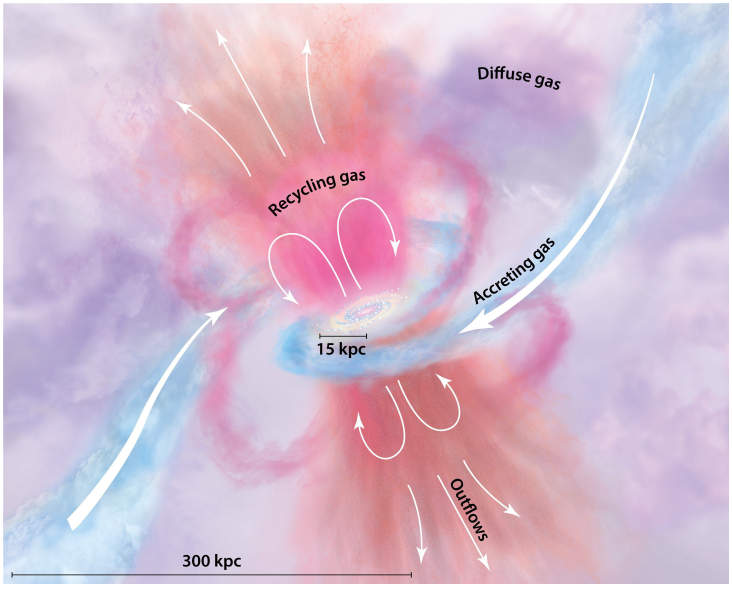

Figure 1.3: Schematic of in- and outflows of CGM gas around a star-forming galaxy. Cold gas (shown in blue) is attracted by the galaxy's gravitational pull and flows into its central regions while, at the same time, feedback effects eject gas outwards (orange). Part of this outflowing gas cannot escape the galaxy's potential well and falls back into the central regions (pink; Tumlinson et al. 2017).

being heated to the virial temperature. Which of these accretion modes dominates depends on the ratio between the cooling time $t_{\rm cool}$ and the free-fall time $t_{\rm ff}$. Hot mode accretion tends to dominate when $t_{\rm cool} > t_{\rm ff}$, leading to the formation of a gaseous pressure supported corona which makes gas accretion more gradual and regulated by radiative energy losses. Conversely, cold mode accretion tends to dominate when $t_{\rm cool} < t_{\rm ff}$, at which point the short cooling time prevents the hot corona from forming and allows the gas to accrete onto the galaxy in a free-fall timescale. The transition between these two regimes depends on the stability of a virial shock which, in turn, depends on the DM halo mass. It is estimated that when $M_{\rm halo} \lesssim 10^{11.5}{\rm M}_{\odot}$, the rapid cooling generates an unstable shock which ensures that the inflowing gas remains cool ($T \sim 10^4\,{\rm K}$). But when $M_{\rm halo} \gtrsim 10^{11.5}{\rm M}_{\odot}$, a stable shock forms that expands into the corona and heats the accreting gas to the virial temperature (Birnboim and Dekel 2003; Dekel and Birnboim 2006). The division between the two accretion modes is therefore roughly determined by the threshold mass $M_{\rm thres} \sim 10^{11.5}{\rm M}_{\odot}$, where hot mode dominates for higher mass halos ($\gtrsim M_{\rm thres}$) and cold mode dominates for lower mass halos ($\lesssim M_{\rm thres}$). This also implies that cold mode accretion dominated in the Early Universe, as the halo masses of nascent galaxies were still well below $M_{\rm thres}$. This was the case for ETGs when they were still forming stars, but currently they are surrounded by hot coronae that are somehow prevented from cooling, as testified by the absence of active star formation in these galaxies.

For star-forming galaxies, the dynamics of the CGM is complex as they experience both in- and outflows due to an interplay between gravity and feedback effects: gravity pulls cool, metal-poor gas in from the IGM, causing inflows, while stellar (and AGN) feedback propels cold gas outwards, causing outflows. However, not all of the ejected gas will leave the galaxy's halo; some of it cannot overcome the galaxy's gravitational attraction and will fall back in (see Figure 1.3). This *recycling scenario* allows the galaxy to "re-use" its enriched gas and form new stars (Tumlinson et al. 2017). A variation of the recycling scenario is the so-called galactic fountain accretion, where an ejected parcel of cold gas interacts and mixes with the hot corona

and cools a fraction of the hot gas. This gas eventually accretes onto the galactic disk, leading to further feeding of the star formation (Fraternali 2017).

1.2.1 Cold CGM around low-redshift ETGs

According to the current theory of galaxy formation, ETGs form the bulk of their stars at $z \gtrsim 2$, possibly via cold mode accretion, but at $z \approx 2$, star formation comes to a halt. This cessation of star formation in galaxies is a phenomenon known as *quenching*. It is expected that the cold mode accretion is succeeded by hot mode accretion once the galaxy has reached a halo mass of $M_{\rm halo} \gtrsim 10^{11.5} \mathrm{M}_{\odot}$ (Birnboim and Dekel 2003; Kereš et al. 2005; Dekel and Birnboim 2006). But in ETGs, the further cooling of the hot gas gets inhibited by AGN feedback effects that can ultimately lead to star formation quenching (Cimatti et al. 2019). One might therefore naively expect that ETGs should harbour no cold gas at all. But numerous observational studies have shown that a large fraction of massive quiescent galaxies at $z \lesssim 0.5$ still have a significant reservoir of cold ionized gas (e.g. Gauthier et al. 2009; Lundgren et al. 2009; Gauthier et al. 2010; Bowen and Chelouche 2011; Gauthier and Chen 2011; Thom et al. 2012; Zhu et al. 2014; Huang et al. 2016; Chen et al. 2018). This raises questions of where this cold gas actually comes from and why it does not feed star formation.

Possible origin and fate of the cold gas

The origin of the cool ionized gas around ETGs is still unclear. Due to the quiescence of these ETGs, the origin of the cold gas is probably related to gas accretion from the IGM or from tidal stripping of gas-rich satellite galaxies (e.g. Afruni et al. 2019). Both scenarios agree with the observation that cool CGM gas can even extend to distances comparable to the virial radius (e.g. Zhu et al. 2014; Huang et al. 2016). The accretion of gas from the IGM furthermore explains why this cold gas is seen in the form of clouds, as the cold filaments from the IGM will most likely fragment into clouds when they reach the virial radius (Afruni et al. 2019). Another possibility is that the cold gas is a leftover from feedback-driven outflows that occurred in the past, but this is generally deemed as unlikely given the quiescent state of these galaxies (Zahedy et al. 2019). Alternatively, the cold clouds could have also condensed out of the hot CGM due thermal instabilities (e.g. McCourt et al. 2012; Sharma et al. 2012; Voit 2018), but this scenario is not likely to occur at around the virial radius where the density of the corona is presumed to be very low. In addition, the conditions under which these instabilities can occur are still debated (Binney et al. 2009; Nipoti and Posti 2014).

What is clear, however, is that these cold clouds are somehow unable to fuel star formation. Perhaps the cold gas is shock-heated before reaching the galaxy's inner regions (e.g. Dekel and Birnboim 2006) or maybe the clouds will get disrupted as they propagate through the hot corona (e.g. Bland-Hawthorn et al. 2007; Putman et al. 2011). In a recent paper, Afruni et al. 2019 argued, based on a semi-analytical model, that passive ETGs still accrete cold gas from the IGM but are unable to feed star formation as the cold gas clouds will disrupt and evaporate in the hot corona (similar to the scenario in Putman et al. 2011) long before reaching the galactic center. This evaporation is the result of the interactions that can occur between the hot and cold phase of the CGM. However, Afruni et al. 2019 did not perform any hydrodynamical simulations to support their claim; these simulations are the subject of the present work.

1.3 Survival of cold gas clouds in the CGM

The propagation of a cold, high-density gas cloud through a hot, low-density medium leads to the onset of two hydrodynamical (HD) instabilities: the *Kelvin-Helmholtz* and *Rayleigh-Taylor* instabilities (Armillotta et al. 2017).

The Kelvin-Helmholtz (KH) instability occurs when there is a velocity difference across the interface between two continuous fluids or a velocity shear in one continuous fluid (Helmholtz 1868; F.R.S. 1871). In our case, the high-density infalling cold cloud moves with a higher velocity relative to the hydrostatic low-density corona. This shear flow induces turbulent activity at the interface between the two fluids, resulting in the formation of wave-like eddies at the cloud-corona interface that strip the cloud of its mass and mix it with the coronal medium. The mixed material has a lower velocity than the cloud and will therefore form a *tail* or *wake* downstream of the cloud's core (Cooper et al. 2009). KH instabilities grow quite quickly due to their relatively small wavelengths but are ultimately not that destructive (Chandrasekhar 1961). Nevertheless, it may still lead to a significant amount of gas stripping due to its short growth time (Cooper et al. 2009). The second instability, the Rayleigh-Taylor (RT) instability, emerges when a less dense fluid is accelerated into a more dense fluid (Rayleigh 1882; Taylor 1950; Drazin 2002). In other words, the cloud becomes subject to the RT instability as it moves through and experiences drag (i.e. deceleration) from the lower density hot medium. This instability has a significantly larger wavelength than the KH instability and therefore takes more time to develop (Chandrasekhar 1961). But once the wavelength is comparable to the size of the cloud, RT becomes extremely destructive and is capable of disrupting the entire cloud (Murray et al. 1993; Vieser and Hensler 2007; Armillotta et al. 2017).

These HD instabilities are thus responsible for the disruption of the cloud by stripping it of its cold gas and mixing it with the hot medium, leading to the formation of *mixed gas*. A rough way to quantify the time scale within which a spherical cloud will be destroyed by these instabilities is with the *cloud crushing* time scale (Jones et al. 1996): $t_{\rm cc} = 2r_{\rm c}\sqrt{\chi}/v_{\rm wind}$, where $r_{\rm c}$ is the cloud radius, $\chi = \frac{n_{\rm c}}{n_{\rm cor}}$ the ratio between the cloud ($n_{\rm c}$) and the coronal density ($n_{\rm cor}$), and $v_{\rm wind}$ the "wind" velocity that the cloud experiences as it propagates through the hot medium. This equation shows that a larger cloud (i.e. higher mass) and/or higher density cloud will lead to a longer survival time.

In addition to these instabilities, there are two other effects that also play an important role in the survival of the cloud: *radiative cooling* and *thermal conduction*.

1.3.1 Radiative cooling

Cold gas can cool via line transitions because the emitted photons will carry away a part of the (kinetic) energy of the gas particles (Cimatti et al. 2019). If the cooling is sufficiently strong and the coronal medium is not too hot, then the cold gas can gain mass by condensing mixed gas into cold gas (e.g. Marinacci et al. 2010; Fraternali 2017). However, in massive ETGs, the corona is so hot that the cooling cannot dominate and the mixed gas will most likely evaporate (though cooling will slow this process down). Another effect of cooling is that it will lead to *fragmentation* when the mixed gas cools below $\sim 10^6$ K (McCourt et al. 2018). This causes the cloud material to spread out over a significantly larger surface area.

1.3.2 Thermal conduction

Thermal conduction occurs in hot ionized media characterized by a steep temperature gradient where heat is transferred from the hot to the cold medium via collisions with free electrons

(Spitzer 1962). Thermal conduction tends to form an evaporative layer between the interface of the hot and cold medium which, in turn, smooths out the density gradient between the two media. This suppresses the KH and RT instabilities that may, consequently, extend the lifetime of the cloud (Marcolini et al. 2005; Orlando et al. 2005; Vieser and Hensler 2007). However, once the cloud starts to break apart, it will rapidly evaporate as the smaller bits of cloud material (cloudlets) will get smoothed out as well. This dual nature of thermal conduction is described by the *Field length* (Field 1965), which serves as a threshold scale; as long as the size of the cloud exceeds the Field length, radiative cooling will dominate and protect it against evaporation. But if the cloud size is smaller than the Field length, then thermal conduction will dominate and rapidly destroy it.

1.4 Analytical model for cold cloud evaporation in ETGs

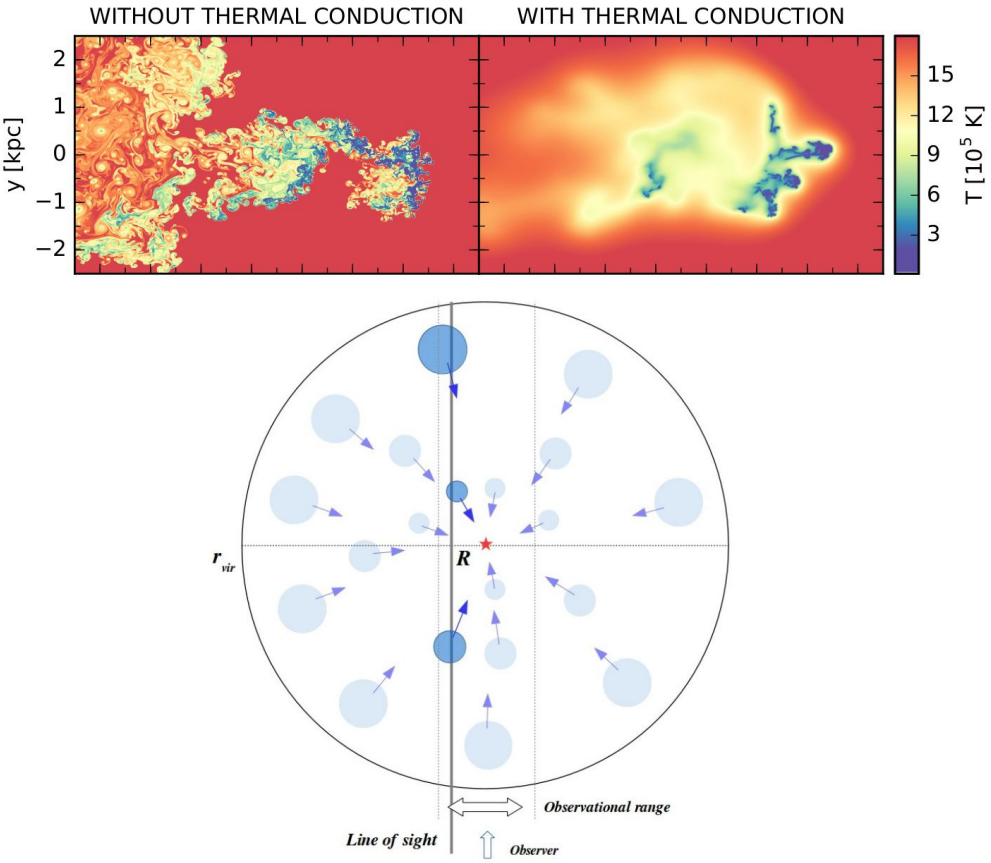

Figure 1.4: Comparison between a numerical (top) and analytical model (bottom). *Top:* Numerical simulation (temperature snapshot) of the disruption of a cold cloud propagating through a hot medium (Armillotta et al. 2017). In the left panel, there is only cooling which allows the KH and RT instabilities to take over and actively mix the cold with the hot gas. The cooling also leads to fragmentation as can be seen from the cloud material's large surface area. In the right panel, there is also thermal conduction which suppresses the KH and RT instabilities, keeps the cloud more compact, and creates a smooth wake at intermediate temperatures. *Bottom:* Sketch of the concept behind the analytical model (Afruni et al. 2019). The clouds start at the virial radius as perfect spheres and will contract — while still retaining their spherical shape — as they move closer to the galactic center.

Afruni et al. 2019 built a semi-analytical model that describes the cold CGM gas as clouds flowing in from the IGM. The model aims to reproduce the observations from the COS-LRG survey (Chen et al. 2018; Zahedy et al. 2019; see also section 1.1.1) from which the spread in cloud velocities and the total number of observed clouds is used as observational constraints. The infalling clouds are assumed to start with zero velocity at the virial radius, from which they will fall inwards towards the galactic center. Initially, the clouds will only experience the gravitational pull from the galaxy, but hydrodynamical effects will start to take over as they continue to move through the hot coronal medium, eventually leading to the destruction of the clouds.

By fitting the kinematic data of the observations using an Markov Chain Monte Carlo (MCMC) approach, Afruni et al. 2019 found that the clouds should have a mass of about $10^5\,M_\odot$ and that the total accretion rate of the cold gas is consistent with the accretion rate predicted by cosmological models (Fakhouri et al. 2010). They furthermore concluded that in order to reproduce the observations, the clouds need to evaporate in the hot corona. The effects that are responsible for cold cloud evaporation were computed with a specific mass loss equation which assumes that mass is exponentially lost. This is, however, a very rough approximation of how the stripping of cold gas proceeds in reality. For a more accurate description of cold cloud evaporation, one will have to resort to numerical models where the mass is directly stripped via HD instabilities (see section 1.3) that eventually tear the cloud apart. The accretion of cold gas by galaxies has already been extensively investigated by cosmological zoom-in simulations (e.g. Nelson et al. 2020), but these simulations do not have a high enough resolution to properly trace the infalling clouds and describe their interaction with the corona. To that end, we aim to build high resolution hydrodynamical simulations that can incorporate and resolve all the effects that arise during cloud-corona interactions.

A comparison between the analytical model of Afruni et al. 2019 and a high resolution numerical model (from Armillotta et al. 2017) is shown in Figure 1.4. Here we also clearly see the effects of radiative cooling (section 1.3.1) and thermal conduction (section 1.3.2), which can only be incorporated numerically.

1.5 Goal of this research

In this work, we aim to investigate the survival of cold, ionized gas clouds in the hot coronae of passive ETGs using 2D high resolution hydrodynamical simulations that incorporate the effects of radiative cooling and thermal conduction. In particular, we explore the scenario where ETGs gain their cold gas via the cosmic filaments from the IGM which reach the virial radius, fragment, and form infalling cold gas clouds. This has already been studied by Afruni et al. 2019, but their model is semi-analytical and, as such, is a rather simplified representation of what should happen in reality. Nevertheless, our simulations will use the same initial setup as described in Afruni et al. 2019 and will, therefore, allow us to also evaluate the validity of their analytical model.

The remaining part of this thesis adheres to the following structure: in Chapter 2, we explain the physics behind the simulations and present the setup of our hydrodynamical model; in Chapter 3, we show the main results of our simulations; in Chapter 4, we interpret our results and draw comparisons with the analytical model of Afruni et al. 2019; and in Chapter 5, we summarize our findings and explore the possibilities of future work.

Chapter 2

Methodology

Detections of cold absorbing clouds in the hot coronae of quiescent ETGs (e.g. Thom et al. 2012; Chen et al. 2018; Zahedy et al. 2019) has served as proof that quenched galaxies do, in fact, still harbour significant amounts of cold gas in their halo regions. Where these cold clouds come from is not completely known, but it is likely that they originate from the IGM. What is even more puzzling, however, is that these galaxies are quenched, meaning that none of these cold clouds are able to reach the central galaxy and feed star formation. Afruni et al. 2019 suggested with an analytical model that cold clouds around massive low-redshift ETGs are indeed incapable of reaching the central galaxies since they will evaporate in the coronal medium due to hydrodynamical interactions. However, due to the analytical nature of their model, the hydrodynamical effects responsible for the cloud evaporation can only be approximated by a specific mass loss equation. To that end, we aim to investigate the survival of cold clouds in the hot coronae of passive ETGs using high resolution hydrodynamical simulations, which will, in addition, also serve as a validity check for the analytical model. We carry out these simulations using PLUTO version 4.3 (Mignone et al. 2007; Mignone et al. 2012) which numerically solves the hydrodynamical (HD) equations that describe the dynamics of an astrophysical fluid.

This chapter presents our numerical methods and is organized as follows. In the first section, we explore the physics of numerical hydrodynamics; in the second section, we explain the setup of our hydrodynamical model; and, in the final section, we describe the various simulations and the associated diagnostics.

2.1 Numerical Hydrodynamics

In order to resolve the complex hydrodynamics of a cold, dense cloud propagating through a hot, tenuous medium, one needs to (simultaneously) solve the three conservation laws that govern the kinematics of a gas: the conservation of mass, momentum, and energy (Mignone et al. 2007; Grønnow 2018):

$$\begin{aligned} \frac{\partial \rho}{\partial t} &= -\boldsymbol{\nabla} \cdot (\rho \boldsymbol{v}), \\ \rho \frac{\partial \boldsymbol{v}}{\partial t} &= -\rho(\boldsymbol{v} \cdot \boldsymbol{\nabla})\boldsymbol{v} - \boldsymbol{\nabla} P - \rho \boldsymbol{\nabla} \Phi, \\ \frac{\partial E}{\partial t} &= -\boldsymbol{\nabla} \cdot (E + P + \rho\Phi)\boldsymbol{v} - \frac{\partial(\rho\Phi)}{\partial t} - n^2 \tilde{\Lambda} + \boldsymbol{\nabla} \cdot \kappa \boldsymbol{\nabla} T, \end{aligned} \tag{2.1}$$

where ρ is the mass density, $\boldsymbol{v}$ the velocity, P the thermal pressure, Φ the gravitational potential, $\tilde{\Lambda}$ the cooling function, n the number density of the gas, κ the thermal conductivity, T the

temperature, and the total energy density: the internal plus kinetic energy, with e the specific internal energy is:

$$E = \rho e + \frac{\rho |\boldsymbol{v}|^2}{2}. \tag{2.2}$$

The Euler equations shown in eq. (2.1) can be written in a flux conserving form, i.e. the *general conservation equation* (LeVeque 2002; Mignone et al. 2007):

$$\frac{\partial \boldsymbol{U}}{\partial t} + \boldsymbol{\nabla} \cdot \boldsymbol{T}(\boldsymbol{U}) = \boldsymbol{S}(\boldsymbol{U}), \tag{2.3}$$

where $\boldsymbol{U}$ is the state vector containing the conserved quantities (e.g. mass), $\boldsymbol{T}(\boldsymbol{U})$ the hyperbolic flux tensor, and $\boldsymbol{S}(\boldsymbol{U})$ the source tensor which contains terms (e.g. cooling) that break the conservation of the quantities contained in $\boldsymbol{U}$. The conservation equation is solved using an Eulerian finite-volume scheme which discretizes the HD equations on a mesh of grid cells. The description of the fluid is *Eulerian* since the fluid elements are evaluated within fixed grid cells. If, instead, the grid cells would be moving along with the fluid elements, then the description would be *Lagrangian* (Bennett 2006). Note that a finite-volume method uses grid *cells* instead of grid points. Each grid cell consists of a grid point located at the *cell center* x_i which is contained within the *cell walls*:

$$x_{i+1/2} = \frac{1}{2}(x_i + x_{i+1}), \tag{2.4}$$

where $x_{i+1/2}$ is the interface between the two cell centers x_i and x_{i+1}. Each cell has a volume V that contains a conserved quantity u_i^n, so the total content of each cell is $\mathcal{U}_i^n = u_i^n V$ (where n stands for the time step). To conserve the overall quantity, $\mathcal{U}_i^n$ should only change via in- and out-flows through the surrounding cell walls (i.e. there is no external source). We can therefore define a *flux* $f_{i+1/2}$ at each cell wall. Bearing this in mind, the time evolution of quantity u_i^n can be written in a *flux-conserving form*:

$$u_i^{n+1} = u_i^n + \frac{\Delta t}{\Delta x}\left(f_{i-1/2}^{n+1/2} - f_{i+1/2}^{n+1/2}\right), \tag{2.5}$$

where Δt is the time step, Δx the grid cell size, and $f_{i\pm1/2}^{n+1/2}$ is the half-time flux (i.e. $n+1/2$) at both interfaces (which, in general, allows for more accuracy). By writing the conservation equation in this form, we ensure that conserved quantities remain constant over time (LeVeque 2002; Toro 2009). In reality, however, we have source terms as well as pressure work which break the conservation of u_i^n.

In this thesis, we utilize the higher-order Godunov scheme (which is commonly used in astrophysics) to solve eq. (2.3). This requires: (i) a time integration scheme, (ii) a reconstruction and slope limiter scheme, and (iii) a Riemann solver.

2.1.1 The time integration scheme

Equation (2.5) is an example of an *explicit* time integration scheme, where the current time step (n) is used to find the next time step ($n+1$). To maximize the efficiency of the code, one wants to use the largest possible time step. The problem with large time steps, however, is that they are prone to cause instabilities in the code. In other words, the size of the time step is bound by a stability constraint. A widely-used numerical stability constraint is the Courant-Friedrichs-Lewy (CFL) condition (Courant et al. 1928), which for N dimensions is defined as:

$$\mathrm{CFL} = \Delta t \left(\sum_{i=1}^{N} \frac{\boldsymbol{v}_{x_i}}{\Delta x_i} \right) \leq C_{\max}, \tag{2.6}$$

where Δt is the time step, $\boldsymbol{v}_{x_i}$ the velocity of a propagating wave (i.e. the solution of the Riemann problem as described in section 2.1.3), and Δx_i the grid cell size. For an explicit time integrator, $C_{\max}$ is generally of the order of unity and must not be exceeded in order to reach a converging solution. In essence, the CFL condition tells us that information must propagate at the correct physical speeds in order to maintain numerical stability (LeVeque 2002). We see this back in eq. (2.6), where a higher wave velocity $\boldsymbol{v}_{x_i}$ needs to be balanced by a smaller time step (assuming constant Δx_i). Note, however, that the CFL condition is a necessary, but not always sufficient criterion; numerical instability can still arise even when the CFL condition is satisfied (Toro 2009; Grønnow 2018).

One can also use an *implicit* time integration scheme where u_{n+1} is found by using u_{n+1} itself. These schemes are often harder to implement than explicit schemes, but tolerate a larger value for $C_{\max}$ and are thus less restricted by the time step size (Ferziger and Peric 2002).

There are a variety of integration methods, of which the Euler method is the most simple and straightforward at the cost of being only accurate to first order. To overcome this, one has to resort to higher-order integrators such as Runge-Kutta. In this thesis, we adopt the *characteristic tracing* integrator which is second-order accurate in space and time (see PLUTO manual in Mignone et al. 2007).

2.1.2 Reconstruction and slope limiting

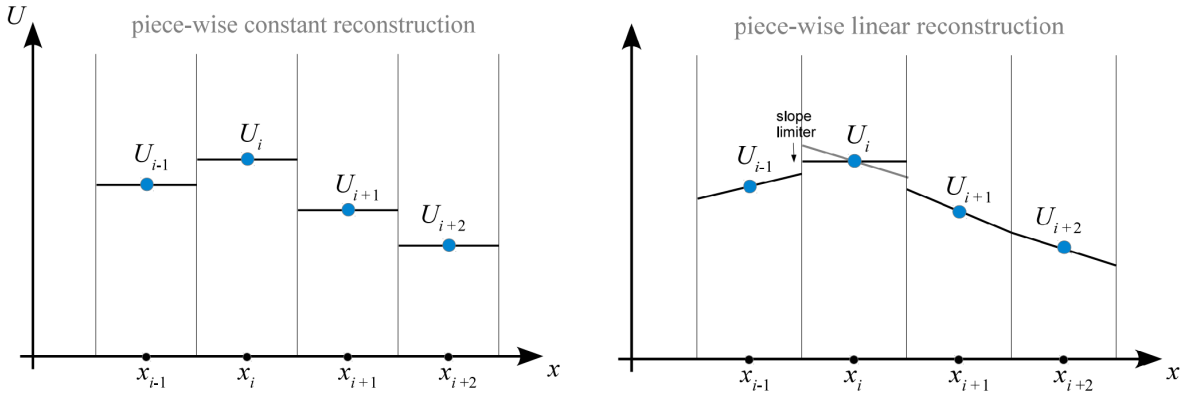

Figure 2.1: *Left:* Piecewise constant reconstruction (donor-cell) where the state in each cell is a constant based on the value at the cell center. *Right:* Piecewise linear reconstruction where the state in each cell is a linear function of position. This technique is more accurate, but is prone to "overshoot" at the discontinuities (Springel and Dullemond 2011).

In a finite-volume scheme, each cell has in its center a grid point with a certain value for $\boldsymbol{U}$, but one also needs to know what the value of $\boldsymbol{U}$ is in the remaining part of the cell. More specifically, we need the value of $\boldsymbol{U}$ at the cell interfaces since that is where we define the flux (see eq. (2.5)). The most simple assumption is that the state in the cell is identical to that of the grid center, the so-called *donor-cell* or *piecewise constant reconstruction* method (see left panel of Figure 2.1). This method was pioneered by Godunov 1959, but is only accurate to first order. To extend the accuracy to second order, one can assume that the state in each cell varies linearly as a function of position with a non-zero slope σ_i^n, where i and n stand for the cell location and time step, respectively. We call this *piecewise linear reconstruction* (see right panel of Figure 2.1). The drawback is that the slope can "overshoot" which leads to spurious oscillations near the cell discontinuities (LeVeque 2002). Schemes that do not produce these oscillations, such as the donor-cell method, are known as "monotone". The reason why these oscillations occur is

explained by *Godunov's theorem*, which states that any linear monotone algorithm that is used to solve a PDE can at most be accurate to first order (Godunov 1959). Extending the accuracy to second order by adding a non-zero slope will thus break the monotonicity and lead to this unphysical behaviour.

These spurious oscillations manifest themselves as local minima and maxima whose development can be measured with the *Total Variation* (TV):

$$\mathrm{TV}(\mathrm{u}) = \sum_{\mathrm{i}=1}^{\mathrm{N}} |\mathrm{u_i} - \mathrm{u_{i-1}}|. \tag{2.7}$$

An increase in TV indicates that $\mathrm{u_i}$ is developing oscillations. When $\mathrm{TV}(\mathrm{u}^{\mathrm{n+1}}) \leq \mathrm{TV}(\mathrm{u}^{\mathrm{n}})$ no oscillations will form and the scheme is said to be *total variation diminishing* (TVD; Ferziger and Peric 2002). For our simulations, we use a piecewise linear reconstruction that adheres to TVD.

A way to prevent these overshoots and attain TVD is by using *slope limiters*. A slope limiter retains the second order accuracy of the linear reconstruction, but reverts back to first order around strong discontinuities (see right panel of Figure 2.1). This will prevent the onset of oscillations and will thus keep the scheme monotone. This method, which circumvents Godunov's theorem, was developed by van Leer 1979 and is known as MUSCL (Monotone Upwind Scheme for Conservation Laws), which is still commonly used today (e.g. Krause 2019). In our thesis, we keep the scheme monotone by adopting the slope limiter that PLUTO uses by default (Mignone et al. 2007).

2.1.3 The Riemann solver

A Riemann solver is a numerical algorithm that solves the *Riemann problem*. The Riemann problem is an initial-value problem where the initial state of the system is dictated by a conservation equation which contains a single discontinuity. This discontinuity separates two constant but different quantities u_{L} and u_{R} (Toro 2009):

$$u(x, t = 0) = u_0(x) = \begin{cases} u_{\mathrm{L}} & \text{for } x < 0 \\ u_{\mathrm{R}} & \text{for } x > 0. \end{cases} \tag{2.8}$$

A schematic of this is shown in Figure 2.2. The discontinuity at $x = 0$ can be seen as an infinitesimally thin slab that separates two fluids of, for instance, different temperatures or densities. The Riemann problem naturally occurs in a finite-volume scheme due to the discrete nature of the grid; the quantities within the cells, u, are separated by cell-boundaries which act as discontinuities. The merit of a Riemann solver is that it retains the pressure terms on the left-hand side (advection part) of eq. (2.3), meaning that there are no pressure source terms. In this way, we preserve all three *characteristics*[1] of the Euler equations. If the pressure terms would not be advected, then the solution of the system will not include the propagation of sound waves (Ferziger and Peric 2002; Toro 2009).

From these three preserved characteristics, one finds that the 1- and 3- characteristics represent *sound waves* (i.e. entropy is conserved), while the 2- characteristic represents an *entropy wave* or *contact wave* (i.e. entropy varies). When there is an abrupt change in the value of a quantity (e.g. pressure, density), the sound waves of the 1- and 3- characteristics can become *shock waves* at which point the entropy is no longer conserved on the shock front. This discrete

[1] A characteristic is any line on a (x,t) diagram that follows the possible trajectory of a signal.

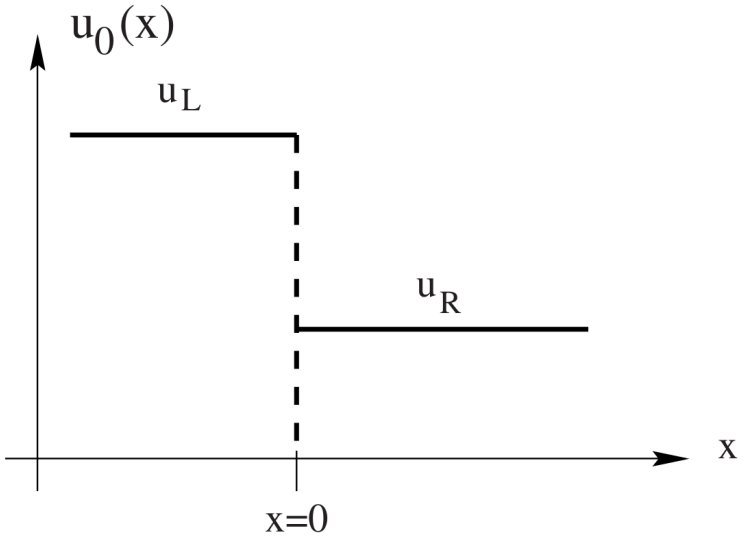

Figure 2.2: A sketch of the Riemann problem. The quantities u_{L} and u_{R} are both constant, but differ in value. They are separated by a discontinuity at $x = 0$ (Toro 2009).

"jump" also occurs in entropy waves, but the difference is that the pressure is constant across an entropy wave while the pressure varies across a shock wave. The 1- and 3- characteristics can also form a *rarefaction wave* which is characterized by continuous change rather than a discrete jump (Toro 2009; Grønnow 2018). Rarefaction waves are often seen in the wake of a shock wave where there is an area of lowered pressure relative to the unshocked medium (Zhang 2016).

The Riemann problem can be either solved exactly or approximately. The *Godunov scheme* or donor-cell method (Godunov 1959; see left panel of Figure 2.1) provides an exact solution leading to the emergence of the characteristic entropy, shock, and rarefaction waves. However, for longer simulations it is computationally too expensive to solve it exactly, so one has to resort to approximate solutions. Approximate Riemann solvers, such as the Harten, Lax, van Leer (HLL)-based solvers, linearize the general conservation equation (eq. (2.3)). An HLL-based solver assumes that only the discontinuities (i.e. the jumps) in the solution of the Riemann problem are waves, thereby completely ignoring the rarefaction waves (which is not a jump). The original HLL-solver (Harten et al. 1983) only uses the two backward and forward sound waves while dropping the middle contact wave. Forgoing the middle wave, however, leads to a gradual smoothing of the contact discontinuities. To resolve this issue, the HLLC-solver (where C stands for "Contact"; Toro et al. 1994) was developed which retains middle wave and keeps the contact discontinuities sharp. We therefore use this solver for our simulations.

2.2 Model setup

We carry out the hydrodynamical simulations in 2D using the PLUTO (version 4.3) code which numerically solves partial differential equations (PDE) via the finite volume or finite difference method based on the Godunov's scheme (Mignone et al. 2007). The relevant equations are discretized and solved on a grid. PLUTO can use a variety of numerical algorithms such as time integration schemes, slope limiters, and Riemann solvers (see section 2.1). For our simulations, we use (i) the characteristic tracing integrator for time stepping, (ii) the default PLUTO slope limiter to prevent spurious oscillations, and (iii) the HLLC solver to solve the Riemann problem. In order to make the simulations more feasible, we employ Adaptive Mesh Refinement (AMR), which splits the grid up in a hierarchy of continuously more refined sub-grids (Mignone et al. 2012). This allows us to save computation time by only fully refining the regions of interest while relegating the rougher grids to the less important regions of the simulation box. The level of refinement depends on the refinement criterion which we base on the *density gradient*, i.e. the steeper the density gradient the higher the resolution. An example of this is shown in Figure 2.3. The base grid (Level 0) has a resolution of 2 grid cells per kpc and is employed for the low density corona. For each level of refinement, we increase the resolution in every dimension by a factor of 2 until the highest resolution of 128 grid cells per kpc (Level 6) is reached.

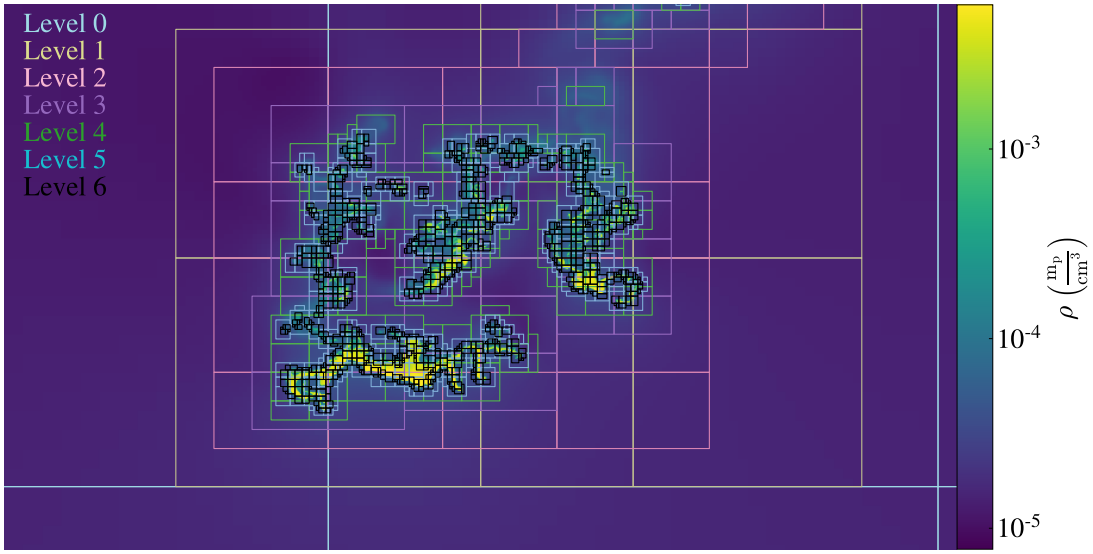

Figure 2.3: Snapshot of the infalling cloud in terms of density overlaid with the AMR refinement grid. The various colours of the grid signify the level of refinement, where Level 0 is the lowest resolution (base) grid and Level 6 is the highest resolution grid. AMR refines the cloud material based on the steepness of the density gradient. Only the regions with significant amounts of cold cloud material are fully refined, as shown by the black grids (Level 6). The other, lower density regions have a less steep density gradient and will therefore be resolved with a continuously lower resolution.

In this work, we study the infall of cold gas clouds through the hot corona of a typical low-redshift massive ETG. In setting up our simulations, we must first consider the gravitational and hydrodynamical effects that this infalling cloud is subject to. These effects, and how we define them, constitute the *initial conditions* of our simulations. Once that foundation has been laid, processes such as cooling and thermal conduction can be added.

2.2.1 Initial conditions

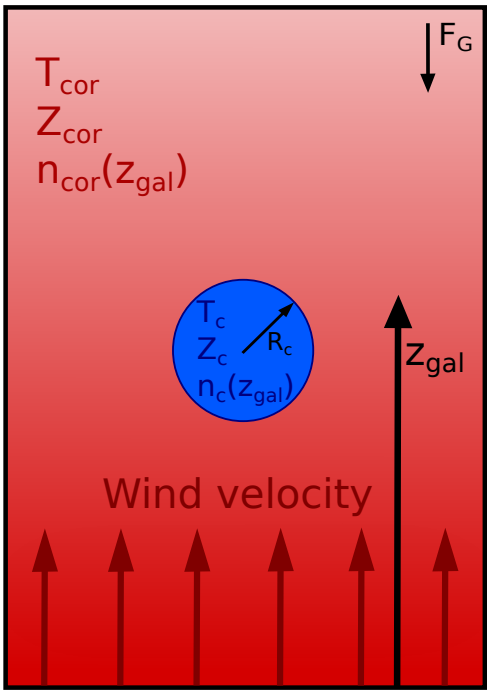

Figure 2.4: Sketch of the model setup: a cold, spherical cloud of uniform density (blue sphere) is radially falling inward to the galactic center due to gravity while being surrounded by a hot, low density medium (red). The simulation is carried out in the reference frame of the cloud, so it experiences a wind from the hot corona as it falls down (more of this is explained in section 2.2.4). The cloud has a radius R_c and a higher density but lower temperature than the corona. Depending on the assumed origin of the cold cloud, it can have a metallicity equal to or less than the coronal medium. The hot corona itself is assumed to be plane parallel such that the galactocentric radius corresponds to the height z_{gal}. As a result, the density gradient of the corona — indicating an increase in coronal density as the distance to the galactic center decreases — is also plane parallel.

For our model we consider a spherical cold cloud of uniform density surrounded by a low density, hot medium that is in hydrostatic equilibrium with the galactic potential (see Figure 2.4). The model is contained within a certain box where we keep a zero gradient at three of the four boundaries via ghost cells (i.e. we assume that the values of the cells outside the simulation box is the same as at the boundaries). At the bottom boundary, we have an injection zone where we inject a wind with a varying velocity. This wind-tunnel setup is chosen so as to mimic the effects of a gas cloud interacting with the hot corona as it falls into the potential well of a galaxy. In such a setup, the simulations are carried out in the reference frame of the cloud (see section 2.2.4).

The cold cloud starts moving at the virial radius with a velocity of $v_i = 0\,\mathrm{km/s}$ and falls radially inward as it is being attracted by gravity. The dynamics of such an infalling cloud is then determined by gravitational and hydrodynamical effects.

Gravitational effects

The main force that drives the infall of cold clouds is the gravitational force of the galactic halo. In our model we assume that the potential is dominated by dark matter (DM) and that the mass distribution of the DM halo is described by the NFW profile (Navarro et al. 1995):

$$M(r_{\rm gal}) = 4\pi\rho_0 r_{\rm s}^3 \left[\ln\left(1 + r_{\rm vir}/r_{\rm s}\right) - \frac{r_{\rm gal}/r_{\rm s}}{1 + r_{\rm gal}/r_{\rm s}}\right] , \tag{2.9}$$

where $r_{\rm gal}$ is the radius centered around the galactic center and ρ_0 is the central density defined as:

$$\rho_0 = \frac{M_{\rm vir}}{4\pi r_{\rm s}^3 \left[\ln\left(1 + r_{\rm vir}/r_{\rm s}\right) - \frac{r_{\rm vir}/r_{\rm s}}{1+r_{\rm vir}/r_{\rm s}}\right]} , \tag{2.10}$$

where $M_{\rm vir}$ and $r_{\rm vir}$ are the virial mass and radius, respectively, and $r_{\rm s}$ is the scale radius defined as $r_{\rm s} = r_{\rm vir}/c$ where c is the concentration. We adopt the averaged values of $M_{\rm vir} = 10^{13.3}{\rm M}_\odot$ and $r_{\rm vir} = 526\,{\rm kpc}$ of the 16 massive ETGs used in Afruni et al. 2019. The concentration was calculated following Dutton and Macciò 2014, resulting in a value of $c = 6.9$. The gravitational potential of the NFW halo is given by:

$$\Phi(r_{\rm gal}) = -\frac{4\pi G\rho_0 r_{\rm s}^3}{r_{\rm gal}} \ln\left(1 + r_{\rm gal}/r_{\rm s}\right), \tag{2.11}$$

where G is the gravitational constant.

Hydrodynamical effects

For simplicity, we assume the hot corona to be *isothermal* with a temperature equal to the virial temperature, $T_{\rm vir}$, and in *hydrostatic equilibrium* with the DM halo. We also make the simplifying assumption that the potential and coronal number density are *plane parallel*, i.e. they are a function of height only: $r_{\rm gal} \to z_{\rm gal}$. From these assumptions one can derive the following electron density profile:

$$n_{\rm e,cor}(z_{\rm gal}) = n_{\rm e,0} \exp\left[-\frac{\mu_{\rm cor} m_{\rm p}}{k_{\rm B} T_{\rm cor}} (\Phi(z_{\rm gal}) - \Phi_0)\right] , \tag{2.12}$$

where $\mu_{\rm cor} = 0.6$ is the mean molecular weight of the completely ionized coronal gas (Sutherland and Dopita 1993), $m_{\rm p}$ is the proton mass, $k_{\rm B}$ is the Boltzmann constant, $T_{\rm cor} = T_{\rm vir} = 6.5 \times 10^6\,{\rm K}$ is the coronal temperature equal to the average virial temperature of the 16 ETGs, and Φ_0 and $n_{\rm e,0} = 6 \times 10^{-3}\,{\rm cm}^{-3}$ are the NFW-potential and the normalized gas density at the lowest point with a height of $r_0 = 10\,{\rm kpc}$ above the midplane, respectively. The value for $n_{\rm e,0}$ was obtained by assuming that the total coronal mass is equal to 20% of the total baryonic mass ($M_{\rm bar} = f_{\rm b} M_{\rm vir}$, where $f_{\rm b} = 0.158$ is the cosmic baryon fraction (Planck Collaboration et al. 2020)) inside the galaxy halo (Afruni et al. 2019). This percentage is based on observational estimates (e.g. Anderson and Bregman 2011; Bogdán et al. 2013), but its exact value is still under debate.

By assuming that the cloud and the corona are in *pressure equilibrium*, one can easily compute the density of the cloud $n_{\rm c}$:

$$n_{\rm c} T_{\rm c} = n_{\rm cor} T_{\rm cor}, \tag{2.13}$$

where $T_{\rm c} = 2 \times 10^4\,{\rm K}$ is the cloud temperature, for which we assume the mean temperature of the cool absorbers in the COS-LRG sample (Zahedy et al. 2019), and $n_{\rm cor} = 2.1 n_{\rm e,cor}$ is the total particle number density of the corona (Afruni et al. 2019). Notice that the density of the hot corona as well as the density of the cold cloud (due to the pressure equilibrium) increase when they get closer to the galactic center (see Figure 2.5). This means that the clouds become smaller as they get closer to the galactic center (if they are not torn apart by HD instabilities first).

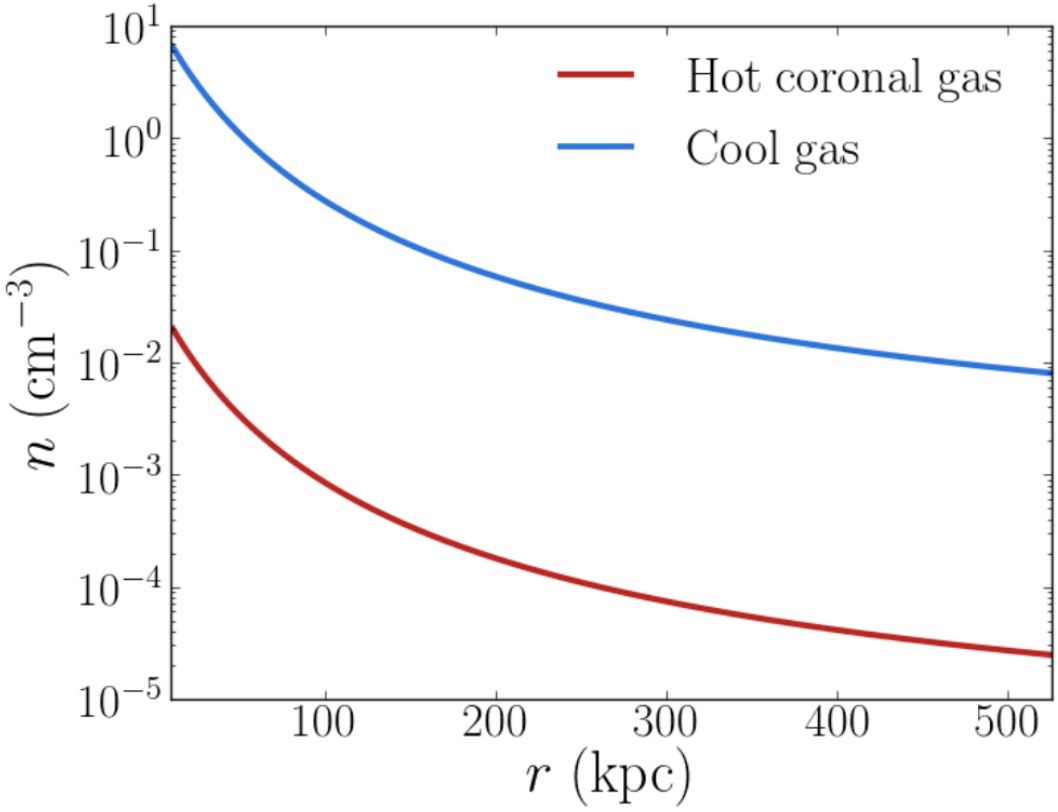

Figure 2.5: Density fall-off as a function of distance from the galactic center. Both the coronal and cold gas attain higher densities as they get closer to the galaxy center. Also notice that the cool gas has a significantly higher density than the coronal medium (Afruni et al. 2019).

In order to have numerical stability at the interface between the cold and hot gas, we define a smooth mass density profile that comprises both the coronal and cloud density (Grønnow et al. 2018):

$$\rho(r_{\rm c}) = \mu_{\rm cor}\left\{n_{\rm cor} + \frac{1}{2}(n_{\rm c} - n_{\rm cor})\left(1 - \tanh\left[s\left(\frac{r_{\rm c}}{R_{\rm c}} - 1\right)\right]\right)\right\}\,, \tag{2.14}$$

where $r_{\rm c}$ is the radius centered on the cloud, $R_{\rm c}$ the cloud radius, and s the steepness of the profile for which we adopt a value of $s = 10$ (note that this value of s is very steep, so the density profile is approximately a top-hat profile). The cloud radius, $R_{\rm c}$, is defined as the radius where the density is halfway between the density of the corona, $n_{\rm cor}$, and the density of the cloud $n_{\rm c}$. For $r_{\rm c} >> R_{\rm c}$, the 2nd term becomes zero and the mass density is equal to the mass density of the corona. For $r_{\rm c} < R_{\rm c}$, the 2nd term will be non-zero and will therefore lead to a top-hat profile that ensures a smooth transition between the cloud and the corona. It should furthermore be mentioned that we assume that the cloud has the same mean molecular weight as the corona[2], i.e. $\mu_{\rm c} = \mu_{\rm cor} = 0.6$.

The precise value of $R_{\rm c}$ depends on the mass of the cloud which for 2D simulations is defined

[2]Note that the cloud should actually have a mean molecular weight of $\mu_{\rm c} = 0.67$ instead of $\mu_{\rm c} = 0.6$ when it is in collisional ionization equilibrium, which we assume for our cooling functions (see Figure 2.6). This difference is, however, so small that it would have a negligible impact on the results.

as:

$$M_{\rm c}(r_{\rm c}) = \int_0^{R_{\rm c}} 2\pi\rho(r_{\rm c})\frac{4R_{\rm c}}{3}r_{\rm c}{\rm d}r_{\rm c}, \tag{2.15}$$

where the factor $\frac{4R_{\rm c}}{3}$ is used to rescale the 2D disk to a 3D sphere (Marinacci et al. 2010). By adopting a certain cloud mass, we can derive the value of $R_{\rm c}$ via numerical integration and root-finding. In most cases, we assume that the cloud starts at the virial radius with a cloud mass of $M_{\rm c} = 10^5\,{\rm M}_\odot$ based on the findings of Afruni et al. 2019. This leads to a cloud radius of $R_{\rm c} \approx 0.71\,{\rm kpc}$.

Finally, we assume that the corona obeys the ideal gas law such that the (coronal) pressure is given by:

$$P = n_{\rm cor}k_{\rm B}T_{\rm cor}. \tag{2.16}$$

The above mentioned equations contain some parameters that we keep fixed at all times. An overview of all our fixed parameters is shown in Table 2.1.

Table 2.1: Fixed simulation parameters where $n_{\rm e,0}$ is the normalized gas density at $r_0 = 10\,{\rm kpc}$, $T_{\rm c}$ the cloud temperature, $T_{\rm cor}$ the coronal temperature, $M_{\rm vir}$ the virial mass, $r_{\rm vir}$ the virial radius, r_0 the smallest considered radius above the midplane for which the coronal electron density profile is equal to $n_{\rm e,0}$, $\mu_{\rm cor}$ the mean molecular weight of the hot corona, c the concentration parameter, and s the steepness of the density profile (these parameters are used in eqs. (2.9) to (2.14) and eq. (2.16)). Note that $T_{\rm cor}$, $M_{\rm vir}$, and $r_{\rm vir}$ are the averaged quantities from the 16 low-redshift ETGs in Afruni et al. 2019. In addition, we also keep the metallicity of the corona ($\rm Z_{cor}$) fixed at all times.

$n_{\rm e,0}$ ($\rm cm^{-3}$)	$T_{\rm c}$ (K)	$T_{\rm cor}$ (K)	$M_{\rm vir}$ ($\rm M_\odot$)	$r_{\rm vir}$ (kpc)	r_0 (kpc)	$\mu_{\rm cor}$	c	s	$\rm Z_{cor}$ ($\rm Z_\odot$)
6×10^{-3}	2×10^4	6.5×10^6	$10^{13.3}$	526	10	0.6	6.9	10	0.3

2.2.2 Cooling and thermal conduction

The energy loss due to radiative cooling (Λ) depends on the cooling function ($\tilde{\Lambda}$) and number density of the gas (n; Mignone et al. 2007):

$$\Lambda = -n^2\tilde{\Lambda}(T, {\rm Z}) \tag{2.17}$$

where $\tilde{\Lambda}$ is in units of erg $\rm cm^3\ s^{-1}$ and is a function of both metallicity and temperature[3]. In Figure 2.6, we see that the cooling is most effective at an intermediate temperature of around $\sim 10^{5.4}\,{\rm K}$. This is a temperature that the gas can attain when the cold and hot gas mix together. Depending both on the metallicity as well as the coronal temperature, the mixed gas can either *condensate* into cold gas or *evaporate* into hot coronal gas. Since the temperature of the corona increases as a function of the virial mass, cold cloud evaporation becomes more and more likely in massive galaxies as the intermediate temperature of the mixed gas will also become higher (for which the cooling is less effective). In fact, Armillotta et al. 2016 found that gas condensation is completely ineffective for $M_{\rm vir} > 10^{13}\,{\rm M}_\odot$, implying that the mixed gas should always evaporate

[3]We compute $\tilde{\Lambda}$ using the data from the cooling tables of Sutherland and Dopita 1993 and the equation $\tilde{\Lambda} = \Lambda_{\rm net}/(\rho_{24}/\bar{\mu})^2$, where $\Lambda_{\rm net}$ is the net cooling function in erg $\rm cm^{-3}\ s^{-1}$, ρ_{24} is the density in g $\rm cm^{-3}$ times 10^{24}, and $\bar{\mu}$ is the mean molecular weight in g times 10^{24}.

in our model (for which we assume $M_{\rm vir} = 10^{13.3}\mathrm{M}_\odot$). The opposite is true in Milky Way-like galaxies whose virial mass — and therefore coronal temperature — is low enough to allow for gas condensation. Nonetheless, radiative cooling does play an important role in the survival time of the cloud as it slows down the destruction of the cold gas when it mixes with the coronal medium.

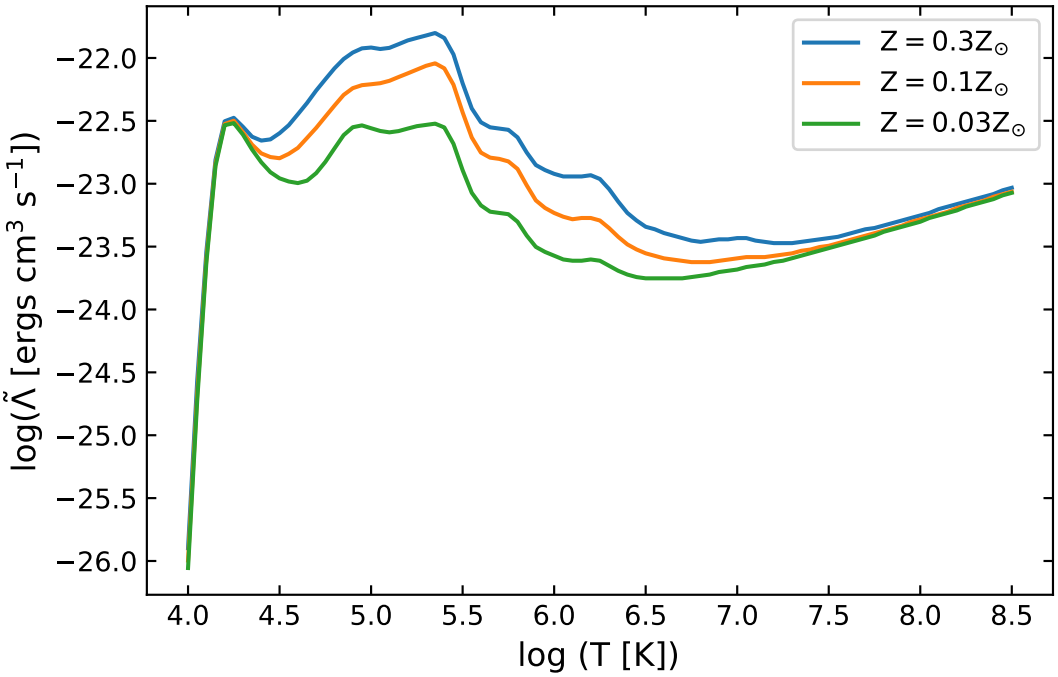

Figure 2.6: Normalized cooling function ($\tilde{\Lambda}$) as a function of temperature for $\mathrm{Z} = 0.03\,\mathrm{Z}_\odot$ (green), $\mathrm{Z} = 0.1\,\mathrm{Z}_\odot$ (orange), and $\mathrm{Z} = 0.3\,\mathrm{Z}_\odot$ (blue) adopted from the Collisional Ionization Equilibrium (CIE) cooling tables of Sutherland and Dopita 1993. A higher metallicity leads to more efficient cooling, but does not impact the overall shape of the cooling curve; for all three metallicities we see that the cooling rate is at its peak efficiency at a temperature of $\sim 10^{5.4}\,\mathrm{K}$.

Because of the high temperature difference between the corona and the cloud, *thermal conduction* cannot be neglected. In an ionized plasma, thermal conduction occurs via free electrons as described by the classical Spitzer conductivity (Spitzer 1962; Draine and Giuliani 1984):

$$\kappa_{\rm Sp} = f \cdot 5.6 \times 10^{-7} T^{5/2} \tag{2.18}$$

where f is a suppression factor which approximates the suppression of thermal conduction due to magnetic fields by assuming it is an *isotropic* process. In reality, however, thermal conduction is only suppressed in the direction perpendicular to the magnetic field and is therefore an *anisotropic* process (Kooij et al. 2021). But since barely anything is known about the magnetic field strength in hot coronae around ETGs, the simplifying assumption of an isotropic suppression is justified. Without this suppression, the thermal conduction would be unrealistically efficient, which would hinder the acceleration of the infalling cloud (Brüggen and Scannapieco 2016).

2.2.3 Tracer

When investigating the evolution of the infalling cloud, one needs to be able to keep track of the cloud material. We carry this out with the help of a *tracer*. A tracer acts as a passive scalar,

meaning that it moves along with the fluid without influencing the HD equations (like adding a colour to a liquid). We define the tracer C in the initial conditions where it has a value of 1 when it is located at a cloud-centric distance, r_c, that lies within the cloud radius and 0 when it exceeds the cloud radius:

$$C = \begin{cases} 1 & \text{if } r_c < R_c \\ 0 & \text{if } r_c \geq R_c. \end{cases} \tag{2.19}$$

In this way, we can not only keep track of the cloud material as it moves along with the evolving fluid, but it also allows us to restrict certain effects to only the cloud material. The latter case is important when we include radiative cooling since any cooling of the hot corona — albeit inefficient cooling due to its high temperature and low density (see eq. (2.17) and Figure 2.6) — would disrupt its (approximate) hydrostatic equilibrium[4]. In reality, the cooling of the coronal medium is counteracted (and therefore kept in hydrostatic equilibrium) by the heating effect of the metagalactic UV field (Haardt and Madau 1996; Haardt and Madau 2001; Haardt and Madau 2012). In our model, we roughly mimic this effect by setting a cooling floor at 2×10^4 K (which ensures that no gas can cool below the cloud temperature T_c) and by prohibiting the cooling of any unmixed coronal gas with a second tracer. The second tracer is defined in the initial conditions where we only allow cooling to occur within a cloud-centric distance of $r_c < 1.3R_c$[5]. The reason why we use $1.3R_c$ is because for $r_c = R_c$ the density is half the cloud density which still classifies as mixed gas while for $r_c = 1.3R_c$ the density is practically equal to the coronal density (see eq. (2.14)). In this way, the second tracer will keep track of all the cold and mixed gas (but not of the hot gas) as it evolves along with the simulation. This allows us to subject only the cold and mixed gas to radiative cooling, while the hot gas will experience no cooling at all.

2.2.4 Comoving grid

Following an infalling cloud as it travels through the hydrostatic hot corona is unfeasible with a static grid; the sheer distance the cloud would need to travel to survive its journey would require us to make an exceptionally large grid which would lead to memory issues. Instead, we utilize a *comoving grid* which allows us to keep the center of mass of the cloud material at rest with respect to the grid by travelling along with it. In the reference frame of the cloud, the hot corona ceases to be static and becomes a "wind" that we inject from the bottom of the grid (see Figure 2.4 for a schematic). In this way, we can confine the grid to only the size we need to fully capture a "seemingly static" evaporating cloud.

In order to set up a comoving grid, we need to compute the velocity of the center of mass of the cloud material, v_{CoM}, and subtract that for each time iteration such that v_{CoM} is zero at all times (note that v_{CoM} will be equal to the velocity of the injected "wind"). This ensures that the cloud material remains static. We carry this out with the tracer C (see eq. (2.19)) which keeps track of the cloud material. The center of mass velocity is defined as the total linear momentum of the cloud material, $p = \sum_{i=1}^{n} m_i C v_i$, divided by the total mass of the cloud material M_{tot}:

$$v_{\text{CoM}} = \frac{1}{M_{\text{tot}}} \sum_{i=1}^{n} m_i C v_i, \tag{2.20}$$

[4] Another reason why we disallow the cooling of the hot gas is because the cooling time of the corona is much higher than 1 Gyr, which is the timescale that we consider in our simulations.

[5] Note that the tracer, and therefore the cooling, will evolve along with the simulation after it has been defined in the initial conditions.

where m_i and v_i are the cell mass and velocity of the cloud material in the ith cell, respectively. Because this comoving grid only keeps v_{CoM} at zero for the material that was initially in the cloud, the cold gas will eventually tend to move downward (as the hotter cloud material slows down due to mixing). This will make it seem that the cloud is moving downwards even though it is just the cold gas whose center of mass velocity is not kept at zero.

2.2.5 Refinement threshold

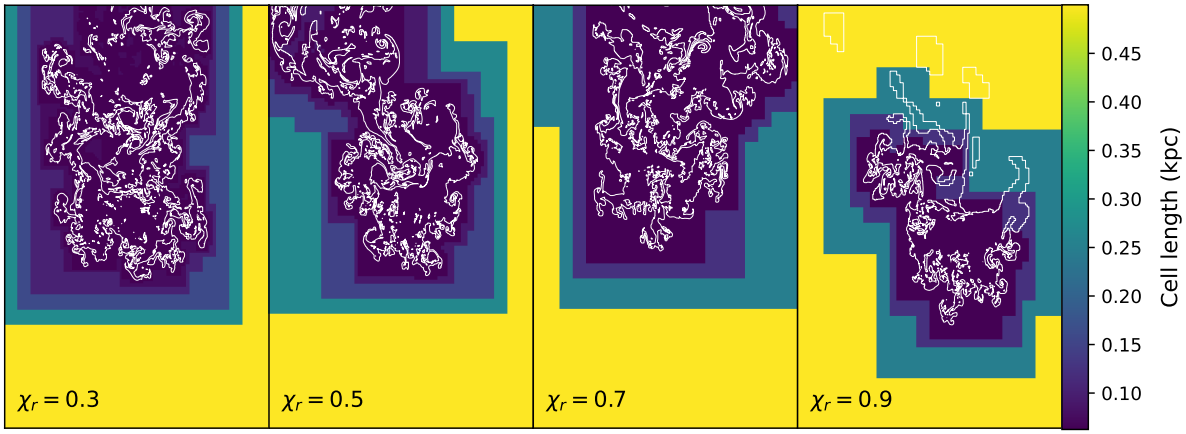

Figure 2.7: Cell length (in units of kpc) plot of a cloud being stripped by HD instabilities with a refinement threshold from left to right of $\chi_r = 0.3$, $\chi_r = 0.5$, $\chi_r = 0.7$, and $\chi_r = 0.9$. The darker patches represent the fully refined regions (smaller cell length), while the yellow patches represent the least refined regions (larger cell length). The overplotted white contours show where the gas has a density of $\rho = 1.2 \times 10^{-5}\,\mathrm{m_p/cm^3}$. For $\chi_r = 0.9$, part of the cloud wake is not being resolved as the density contours leave the fully refined regions.

The refinement criterion that we use for AMR is based on the density gradient, but we also need to define how sensitive AMR should be for grid cell refinement. This is defined by the *refinement threshold*, χ_r, where everything will be refined if $\chi_r = 0$ and nothing will be refined if $\chi_r = 1$. A comparison of various values for χ_r is displayed in Figure 2.7, in which a fragmenting cloud is shown in terms of cell length. The lowest value $\chi_r = 0.3$ refines most of the substructure including the wake of the cloud, but will be more computationally expensive. The highest value $\chi_r = 0.9$, on the other hand, refines only the highest density regions, causing large parts of the wake to be not refined at all (see density contour in the fourth panel of Figure 2.7). This results in artificially extending the cloud's lifetime as the HD instabilities are not being fully resolved. We therefore opted for a value of $\chi_r = 0.7$ which refines enough of the cold cloud material such that cloud's lifetime will not differ from the lower values $\chi_r = 0.5$ and $\chi_r = 0.3$ (see section 4.2.1 for a convergence test). Using $\chi_r = 0.7$ will, however, lead to a slightly less refined wake, but that has no impact on our results of the cold gas as the wake only contains low density, hot gas.

2.3 The simulations

Table 2.2: Varied simulation parameters. We vary the efficiency of thermal conduction with the suppression factor such that we consider only cooling when $f = 0$, while we consider both cooling and thermal conduction when $f > 0$.

Simulation name[a]	Max resolution (cells/kpc)	$r_{\rm start}$ (kpc)	$R_{\rm c}$ (kpc)	$M_{\rm c}$ ($\rm M_\odot$)	$\rm Z_c$ ($\rm Z_\odot$)	f
f0L, f0H	64,128	$r_{\rm vir}$	0.71	10^5	0.3	0
f0L-Z	64	$r_{\rm vir}$	0.71	10^5	0.05	0
f0L-r	64	$r_{\rm vir}/2$	0.45	10^5	0.3	0
f0L-Z-r	64	$r_{\rm vir}/2$	0.45	10^5	0.05	0
f1L, f1H, f1VH	64,128,256	$r_{\rm vir}$	0.71	10^5	0.3	0.01
f1H-Z	128	$r_{\rm vir}$	0.71	10^5	0.05	0.01
f1H-r	128	$r_{\rm vir}/2$	0.45	10^5	0.3	0.01
f1H-Z-r	128	$r_{\rm vir}/2$	0.45	10^5	0.05	0.01
f1H-M	128	$r_{\rm vir}$	1.53	10^6	0.3	0.01
f1H-Z-M	128	$r_{\rm vir}$	1.53	10^6	0.05	0.01
f2L, f2H, f2VH	64,128,256	$r_{\rm vir}$	0.71	10^5	0.3	0.02
f5L, f5H, f5VH	64,128,256	$r_{\rm vir}$	0.71	10^5	0.3	0.05
f10L	64	$r_{\rm vir}$	0.71	10^5	0.3	0.1

[a] The naming process works as follows: the number after f signifies the used percentage of the suppression factor f (e.g. f1 is f=0.01); the resolution is set to be either Low (L; 64 cells/kpc), High (H; 128 cells/kpc), or Very High (VH; 256 cells/kpc); the reduced cloud metallicity of $\rm Z_c = 0.05\,Z_\odot$ is indicated with the letter Z; a starting radius of $r_{\rm start} = r_{\rm vir}/2$ is labeled with the letter r; and a starting cloud mass of $M_{\rm c} = 10^6\,\rm M_\odot$ is indicated with the letter M.

In order to find out which parameters influence the survival of the cold cloud and in what way, it is necessary to run multiple simulations with varying initial conditions and setups. The parameters that we vary are the suppression factor f, the cloud metallicity $\rm Z_c$, the initial cloud mass $M_{\rm c}$, the starting radius of the infalling cloud $r_{\rm start}$, and the resolution of the grid (see Table 2.2). Note that a change in the cloud mass and/or in the starting radius will also lead to a change in the cloud radius $R_{\rm c}$ (see eq. (2.15)). All simulations shown in Table 2.2 have furthermore been solely carried out in 2D and always include radiative cooling.

When varying the cloud metallicity, we either keep the metallicity for both the cloud ($\rm Z_c$) and corona ($\rm Z_{cor}$) fixed at a value of $0.3\,\rm Z_\odot$, or we give the cloud a lower metallicity of $\rm Z_c = 0.05\,Z_\odot$ while keeping the corona at the same value of $\rm Z_{cor} = 0.3\,Z_\odot$[6]. For the latter case, we require a third tracer to define to the metallicity of the cloud and the corona in the initial conditions[7]. The border between these two metallicities ought to be placed at a radius where the density is significantly different from the corona. We therefore define it at the radius centered around the cloud where the density is twice the coronal density, i.e. $n(r_{\rm c}) = 2n_{\rm cor}$. All the cloud material within that radius is (in the initial conditions) set at $0.05\,\rm Z_\odot$, while the cloud material beyond that radius is set at $0.3\,\rm Z_\odot$. The computation of the intermediate metallicities (as well as the

[6] Note that the metallicity of the corona is a fixed parameter in our setup (see Table 2.1).

[7] In other words, the tracer is the metallicity itself. This is possible because both the metallicity and the tracer are fractional numbers.

calculation of the cooling curve for $Z_c = 0.05\,Z_\odot$) is then carried out with bilinear interpolation using the three cooling functions ($Z \in \{0.03, 0.1, 0.3\}\ Z_\odot$) as shown in Figure 2.6 (Sutherland and Dopita 1993).

2.3.1 Diagnostics

Computing the cold gas mass $M_{\rm cold}$ at a given time requires us to find all the cells that contain cold gas and sum up their masses. We carry this out by only considering the gas that has a temperature below $T_{\rm cold} = 4 \times 10^4\,\mathrm{K}$. This temperature threshold is twice as high as the cooling floor (as well as the initial cloud temperature T_c), which is set at $2 \times 10^4\,\mathrm{K}$. The reason for this is to ensure that we capture all the cold gas, considering that the temperature tends to fluctuate close to the cooling floor. This also means that the mass of the original cloud material (M_c) — which is set by the tracer (eq. (2.19)) — is not the same as the mass of the cold gas ($M_{\rm cold}$). The reason for this is because the mass of the cloud material does not change with time as long as the tracer does not leave the simulation box. The mass of the cold gas, on the other hand, will change once evaporation (or condensation) sets in. Note that since we are dealing with 2D simulations, we also need to multiply $M_{\rm cold}$ with the conversion factor $\frac{4R_c}{3}$ to rescale the 2D disk to a 3D sphere to obtain the true mass (Marinacci et al. 2010).

Using this cold gas, we can define a couple of diagnostics. The first one pertains to the cold gas mass loss of our hydrodynamical model relative to the analytical model. Afruni et al. 2019 assumed that the cold gas in their analytical model loses mass *exponentially* according to the following equation:

$$M_{\rm cold}(t) = M_{\rm cold}(0)e^{-\alpha t}, \tag{2.21}$$

where $M_{\rm cold}(0)$ is the initial cold cloud mass, α is the *evaporation rate* used to analytically describe the evaporation of the cold gas (see Fraternali and Binney 2008; Marinacci et al. 2010), and t is the time.

The second diagnostic is related to the cloud morphology: the shape of the infalling cloud changes as a function of time due to HD instabilities which strip the cloud of its cold gas and eventually tear it apart. A way to quantify the change in cloud shape is by investigating the spread of the cold gas along x and y at a given moment in time. We call this the *effective size*, which is defined as (Klein et al. 1994; Mac Low et al. 1994; Banda-Barragán et al. 2016):

$$R_{\rm eff} = \left[5\left(\langle X_j^2\rangle - \langle X_j\rangle^2\right)\right]^{1/2}, \tag{2.22}$$

where X_j is the coordinate along axis j which can either be $j = x$ or $j = y$, $\langle X_j\rangle$ is the averaged cloud extension, and $\langle X_j^2\rangle$ is its root mean square. The angle brackets $<>$ indicate that we are considering a cold gas mass weighted volume average defined as:

$$\langle Q_{\rm cold}\rangle = \frac{\int Q_{\rm cold}\rho_{\rm cold}\mathrm{d}V}{\int \rho_{\rm cold}\mathrm{d}V}, \tag{2.23}$$

where $Q_{\rm cold}$ is a certain quantity (in this case the coordinate X_j) of the cold gas and $\rho_{\rm cold}$ is the density of the cold gas. From the effective size, one can also derive the cross-sectional area of the cold gas known as the *effective area*:

$$A_{\rm eff} = \pi R_{\rm eff}^2. \tag{2.24}$$

Chapter 3

Results

In this chapter, we show the main results that we obtained from our 2D hydrodynamical simulations to investigate the survival of cold CGM clouds in the hot coronae of massive ETGs. We first focus our attention on one main simulation (the fiducial simulation) and then we discuss how varying the parameters influences those results.

This chapter is organized as follows. In section 3.1, we present the main results of our fiducial simulation; in section 3.2, we investigate how the results of the fiducial simulation change when we vary the suppression factor (section 3.2.1), the cloud metallicity (section 3.2.2), the initial cloud mass (section 3.2.3), and the starting radius (section 3.2.4); and in section 3.3, we summarize our results.

3.1 The fiducial simulation

Our fiducial setup is the f1H (hydro) simulation, where the cloud starts at the virial radius, has a mass of $10^5\,M_\odot$, undergoes radiative cooling via line transitions, contains gas at the same metallicity as the corona ($0.3\,Z_\odot$)[1], experiences thermal conduction with an efficiency of 1% ($f = 0.01$), and has a maximum resolution of 128 cells/kpc (see Table 2.2).

The evolution of the cloud for the f1H simulation is shown in terms of density (Figure 3.1) and in terms of temperature (Figure 3.2). When comparing these plots, it becomes clear that the density and temperature have the same shape and that a high (low) density corresponds to a low (high) temperature. The three panels display three instances in time: approximately 250, 500, and 750 Myr after the cloud has started falling in from the virial radius. After ≈ 250 Myr, the cloud has lost its initial spherical shape and has slightly deformed, but seemingly no cold gas has been lost. At $t \approx 500$ Myr, the cloud has further deformed as it has become elongated along the x-axis and flattened along the y-axis. Small bits of cloud material have started to detach, but the cloud has not yet been disrupted as the thermal conduction (f=0.01) tends to suppress the onset of HD instabilities and protects the cloud as long as the cloud size is larger than the Field length (Field 1965; see section 4.1.1 for more information). However, after ≈ 750 Myr, the HD instabilities have become strong enough to tear the cloud apart into small clumps of cold gas. Because these clumps are all smaller than the Field length, the remaining cold gas undergoes rapid evaporation as the thermal conduction becomes dominant and smooths out the remaining cold gas.

[1] Note that the metallicity of the hot corona is in general quite uncertain, especially in the outer regions and even more so in ETGs. $0.3\,Z_\odot$ is based on the estimated coronal metallicity of the Milky Way (Miller and Bregman 2015), which is also still ill-constrained.

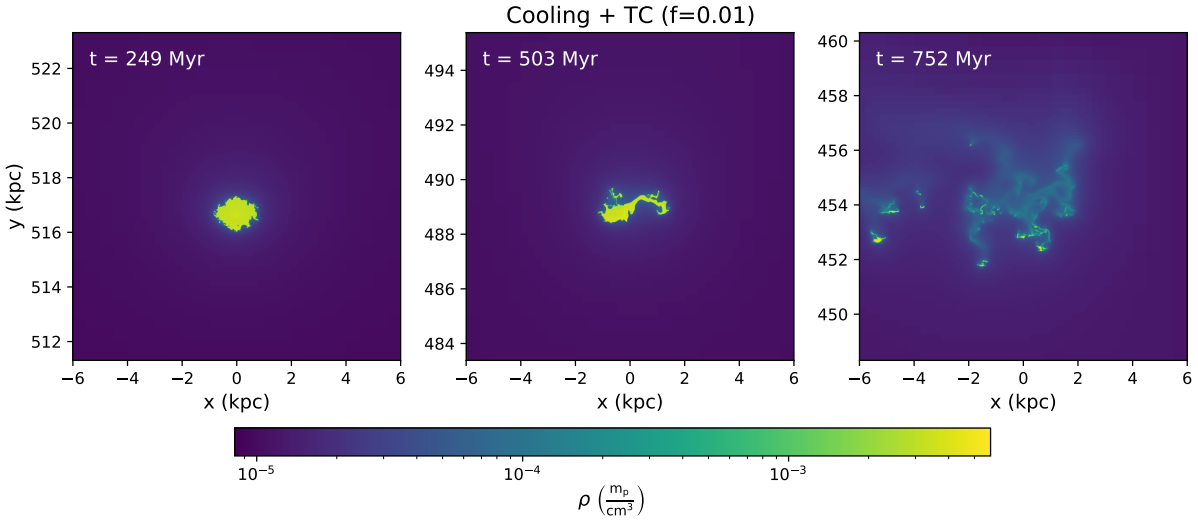

Figure 3.1: Density map of the f1H simulation with logarithmic colour scales at three time instances: a high density, cold cloud (yellow) of mass $10^5\,\mathrm{M}_\odot$ and metallicity $\mathrm{Z_c} = 0.3\,\mathrm{Z}_\odot$ moves through a tenuous, hot coronal medium (in dark blue) wherein it ultimately evaporates. The y-axis displays the current height of the cloud above the midplane and updates for the distance that the infalling cloud has already travelled. The timer in the left-hand corner indicates the amount of time that has elapsed since the cloud has started falling down from a height of $y = r_{\mathrm{vir}} = 526\,\mathrm{kpc}$. The density is in units of proton mass per cm^3.

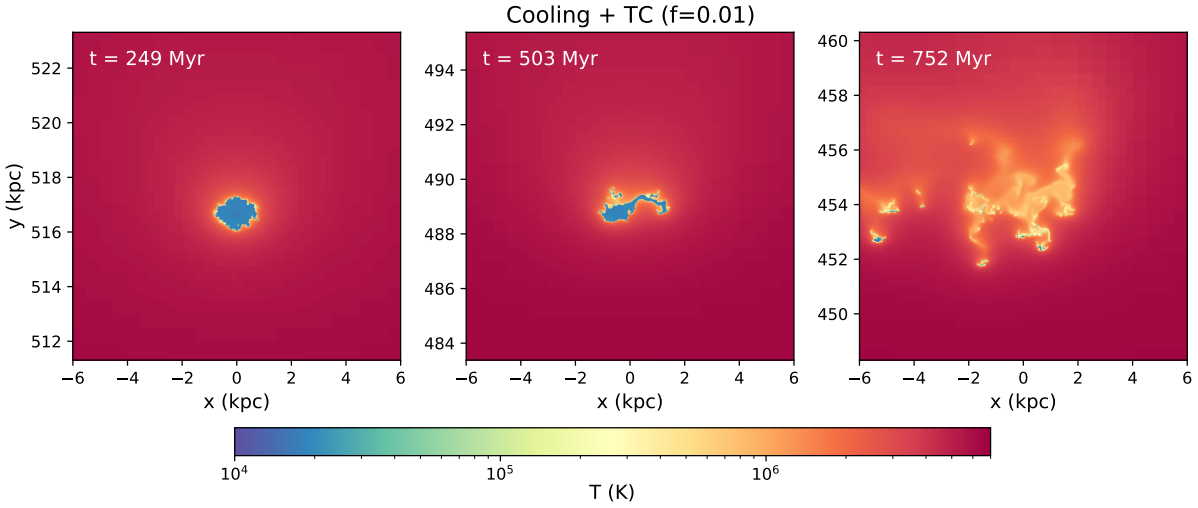

Figure 3.2: Temperature snapshots of the f1H simulation with logarithmic colour scales at the same three time instances of Figure 3.1.

3.1.1 Cold gas mass evolution

In the left panel of Figure 3.3, one can see the cold gas mass M_{cold} (i.e. the mass of all the gas that has a temperature below $T_{\mathrm{cold}} = 4 \times 10^4\,\mathrm{K}$) of our fiducial simulation (coloured circles) as a function of time on a semi-logarithmic plot. The first thing that we see is that M_{cold} is declining with time, meaning that cold gas is being evaporated into hot gas. The mass loss initially occurs at quite a slow rate for around $\approx 500\,\mathrm{Myr}$, but after that it comes to a turning point where the mass loss becomes very substantial as the HD instabilities break the cloud into

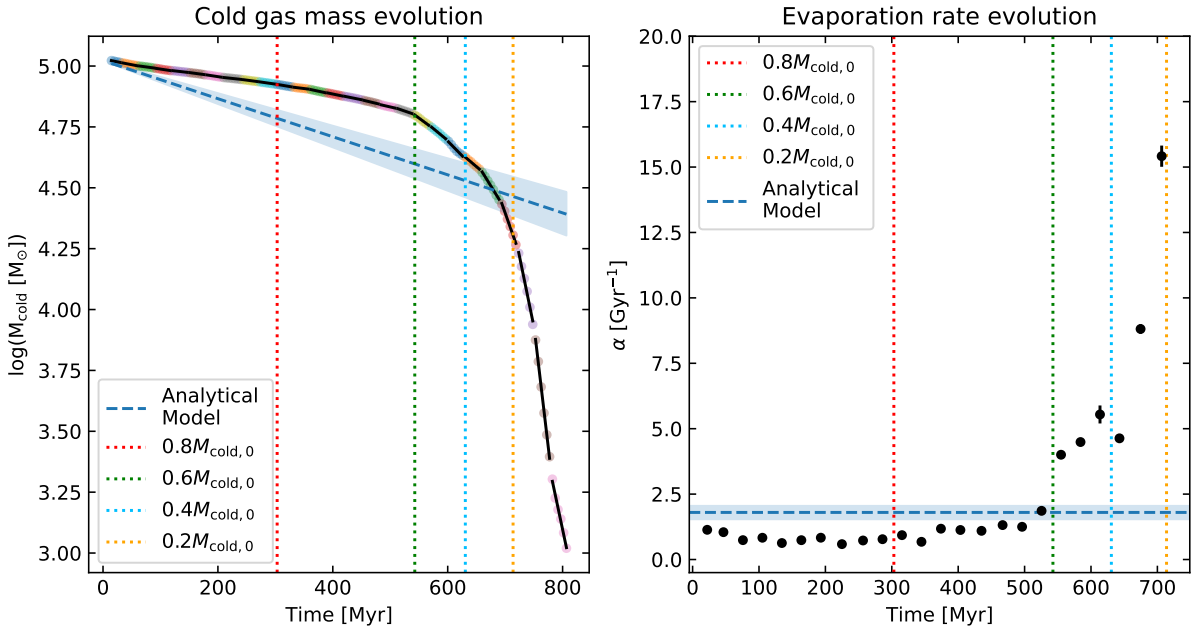

Figure 3.3: *Left:* Semi-logarithmic plot of the cold gas mass as a function of time for the f1H fiducial simulation. The coloured circles represent the simulation data split up into segments of 30 Myr. The four, dashed vertical lines show the time at which 20% (red), 40% (green), 60% (skyblue), and 80% (orange) of the original cold gas mass of the fiducial simulation has evaporated. The black lines represent the exponential decay fits of each data segment. And the blue, dashed line is the cold gas mass loss according to the analytical model of Afruni et al. 2019, where the blue band represents the $\pm 1\sigma$ error. *Right:* The evaporation rate α plotted as a function of time. Each black dot represents the value of α corresponding to the fits of the 30 Myr segments in the left panel with the associated error bar (obtained from the covariance matrix of each fit). The analytical value of $\alpha = 1.8^{+0.25}_{-0.26}\mathrm{Gyr}^{-1}$ is overplotted as a blue, dashed horizontal line, where the blue band represents the $\pm 1\sigma$ error.

smaller cloudlets which are easily evaporated. The various times at which a specific amount of cold gas has evaporated is displayed with four dashed, vertical lines that indicate the time at which the cloud has lost 20% (red), 40% (green), 60% (skyblue), and 80% (orange) of its original cold gas mass. We consider the cold gas to have been evaporated or *crushed* once 80% of its original mass has been stripped. Nevertheless, we show all the simulation data up to the point where it has lost 99% of its initial mass (i.e. when $M_{\mathrm{cold}} = 10^3\,\mathrm{M}_\odot$) so as to display the complete cold gas mass evolution, even though a small fraction of this gas survives till later times. In addition, we also overplotted the cold gas mass loss according to the analytical model of Afruni et al. 2019 including its uncertainties as a blue, dashed line. The analytical model approximates the stripping of cold gas by assuming that mass is lost at a constant exponential rate with evaporation rate α.

In order to draw a comparison between the simulation and the analytical model, we split the simulation data of the cold gas mass up into separate data sets, each spanning a time of 30 Myr as can be seen from the wide range of colours used for the data points. This allowed us to separately fit each one of the subsets of data with an exponential decay function (eq. (2.21)), as shown by the black line segments. From each of these fits we obtained an estimate of α at every 30 Myr time interval for our hydro simulation. The evolution with time of the evaporation rate α obtained from our fits, together with the constant value of the analytical model, is shown in the right panel of Figure 3.3. When we compare the hydro simulation with the analytical model in

both panels, we see a distinct difference: in the simulation, the slope — and therefore the value of α — changes as a function of time, while the analytical model has a constant slope with a value of $\alpha = 1.8\,\mathrm{Gyr}^{-1}$. The evaporation rate of our hydro simulation is, however, approximately constant for around $\approx 500\,\mathrm{Myr}$, with an average value of $\bar{\alpha}_{\mathrm{sim}} = 1\,\mathrm{Gyr}^{-1}$. But after that, the value of α strongly increases as the mass loss rate accelerates. The analytical model does not have this transition to the accelerated mass loss and therefore predicts that the cloud will survive for a longer time. This behaviour is illustrated in Figure 3.4, where the percentage of cold gas mass loss of the analytical model is compared with that of the hydro simulation. Initially, the analytical model predicts a faster mass loss than the hydro simulation, but is eventually overtaken by the hydro simulation. As a result, the cold cloud in the simulation takes $\approx 700\,\mathrm{Myr}$ to lose 80% of its original mass, while the analytical model takes about $\approx 900\,\mathrm{Myr}$, which is nonetheless still quite similar to the result of the simulation. This relatively short survival time in both models implies that the cloud most likely evaporates before reaching the central galaxy (as we see more clearly in section 3.1.3).

Note that we have included error bars for the analytical model here since the value of $\alpha = 1.8\,\mathrm{Gyr}^{-1}$ is only the median value (50th percentile) obtained from the MCMC analysis carried out by Afruni et al. 2019. If we also consider the 32nd and the 68th percentile, then we find that $\alpha = 1.8^{+0.25}_{-0.26}\mathrm{Gyr}^{-1}$.

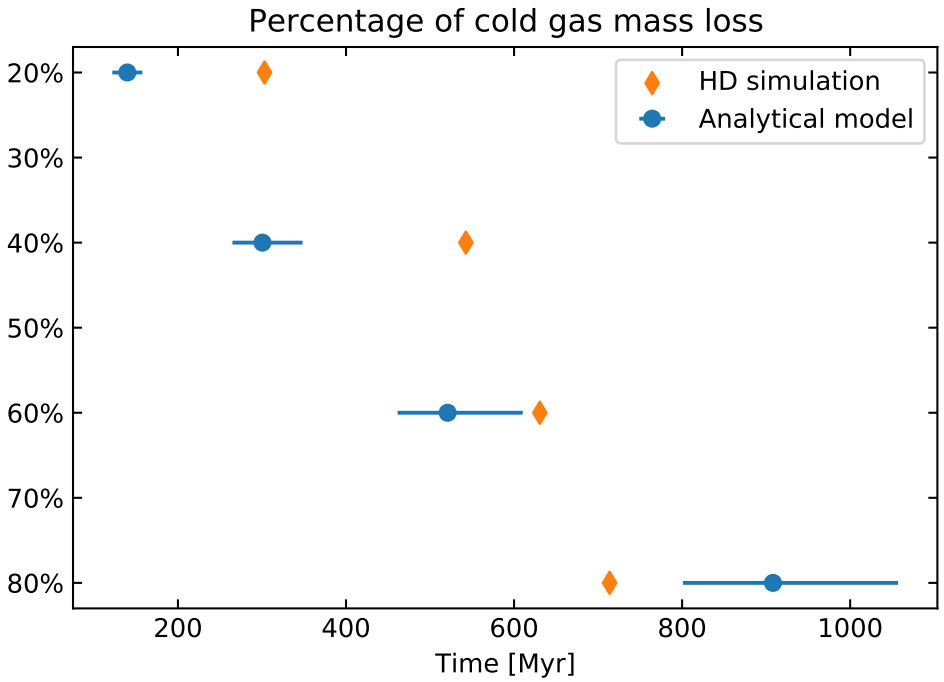

Figure 3.4: Percentage of cold gas mass loss as a function of time for the fiducial (f1H) simulation (orange diamonds) and analytical model (blue circles). The dots represent the timestamps at which the cloud has lost 20%, 40%, 60%, and 80% of its initial cold gas mass for increasing time. The error bars around the analytical model arise from considering the uncertainty in α.

3.1.2 Cloud morphology

In the analytical model, the cold cloud becomes an increasingly smaller sphere during its motion towards the galactic center. In other words, the radius of the cloud decreases as a function of time. This is a consequence of the assumed pressure equilibrium and the increase in coronal density as the height above the galactic plane decreases (see Figure 2.5). In our simulations, on the other hand, the cold gas tends to lose its spherical shape and flattens in the direction parallel to the cloud's motion (see center panel of Figure 3.1). This is an important difference because the evolution of the cloud's size affects the drag and therefore the infall velocity of the cloud. To quantify this behaviour, we computed the effective size, R_{eff}, of the cold gas in the simulation box with eq. (2.22) (see section 2.3.1 for the computational details).

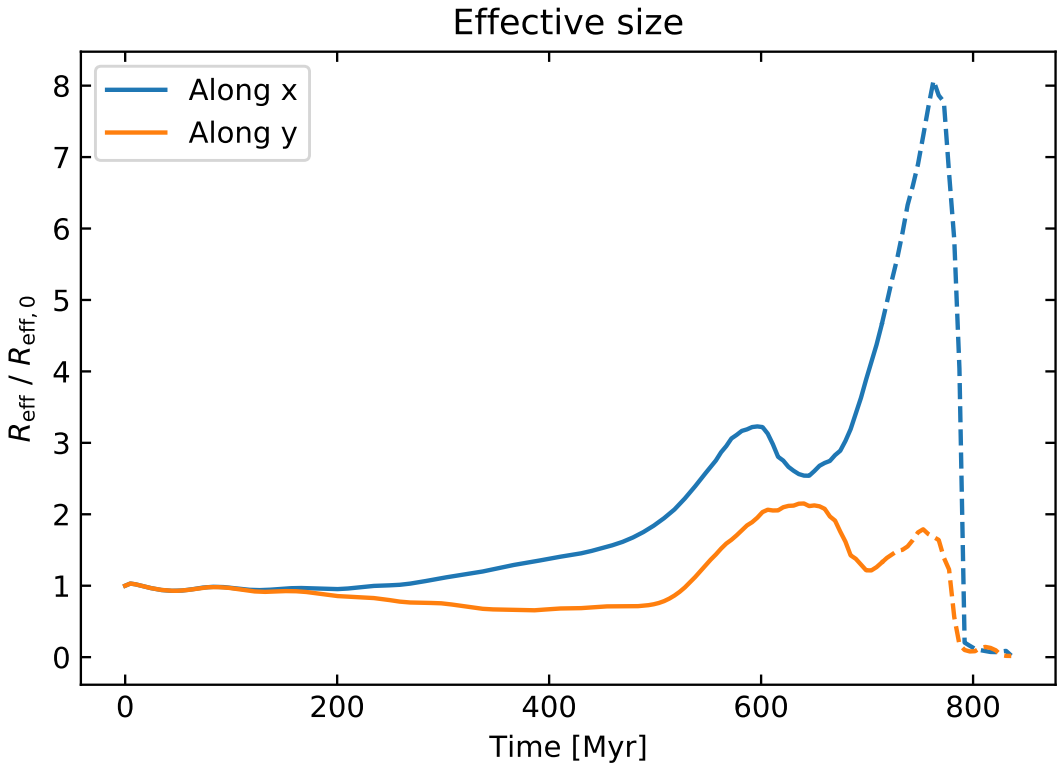

Figure 3.5: The effective size of the cold gas (normalized with respect to its initial value) as a function of time for the f1H fiducial simulation. The blue and orange curve represents the spread of cold gas along x and y, respectively. The dotted line indicates the point in time at which 80% of the initial cold gas mass has evaporated.

In Figure 3.5, the effective size of the cold gas along x and y (where y is the direction of motion) is plotted as a function of time. The spread along x and y is identical for the first $\approx 100\,\mathrm{Myr}$ as the cold gas cloud is still almost a perfect sphere. But at around $t \approx 200\,\mathrm{Myr}$, the effective size along both directions start to decouple as the cold gas begins to stretch out along x and flatten along y. At this point, the cold gas velocity has become high enough that the front of the cold gas cloud begins to experience a "headwind" from the coronal medium, which accounts for the elongation along x and the flattening along y. R_{eff} does not increase along y also because thermal conduction prevents the formation of a wake by smoothing out the stripped cloud material (e.g. Armillotta et al. 2016). However, at $t \approx 500\,\mathrm{Myr}$, the effective size along y does actually manage to increase (along with $R_{\mathrm{eff}}(x)$) as chunks of cold gas (i.e. cloudlets)

start to detach from the main cold gas cloud (the beginning of this can been seen in the center panel of Figure 3.1). These detached cloudlets experience a stronger deceleration because their smaller sizes (i.e. smaller than the Field length) leads to a faster evaporation in the static hot corona. As a result, the cloudlets start to lag behind the main cold gas cloud along the direction of motion (y), which results in an increase in $R_{\rm eff}$ along y. This increase is, however, quite subtle since the detached cloudlets quickly evaporate due to thermal conduction.

Once the cold gas has lost 80% of its initial mass at $t \approx 700\,\mathrm{Myr}$, $R_{\rm eff}(x)$ experiences a steep increase as the mass loss transitions to the accelerated phase (see Figure 3.3), at which point the (partially suppressed) HD instabilities set in and completely tear the cloud apart (mostly along x). Shortly after, the spread of cold cloud material along both axes plummets as more and more cold gas evaporates in the hot corona until they both reach a value of 0 at $t \approx 800\,\mathrm{Myr}$.

3.1.3 Velocity evolution

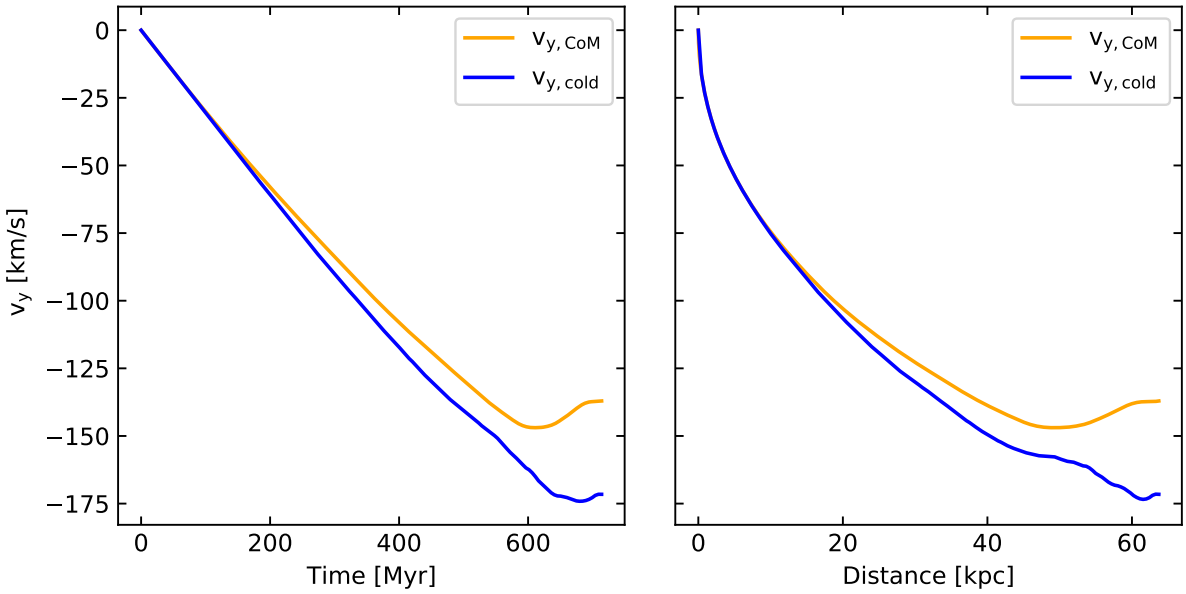

Figure 3.6: Velocity in the negative y-direction of the f1H fiducial simulation (pointing towards the galactic center) as a function of time (left panel) and distance (right panel). The velocity of all the initial cloud material and the velocity of only the cold gas are depicted as orange and blue curves, respectively.

The velocity of the cold gas is calculated by summing the center of mass (CoM) velocity of all the cloud material (i.e. the tracer) together with the average velocity of the cold ($< 4 \times 10^4\,\mathrm{K}$) gas. We follow the evolution of the velocity up to the point where we consider the cloud to have been crushed, i.e. the point where 80% of its initial cold gas mass has evaporated. Notice that since we are dealing with a cloud that falls radially downward, we only need to consider the velocity component along y.

In Figure 3.6, the CoM velocity ($v_{\rm y,CoM}$) and the cold gas velocity ($v_{\rm y,cold}$) are plotted as a function of time (left) and distance (right). In the left panel, we see that $v_{\rm y,CoM}$ and $v_{\rm y,cold}$ are identical for the first $\approx 100\,\mathrm{Myr}$, but soon after they slowly start to decouple as the first bit of cold cloud material evaporates into hot gas. The reason why $v_{\rm y,CoM}$ decreases with respect to $v_{\rm y,cold}$ is because the moving cold gas mixes with the static coronal gas resulting in a lower velocity, while the cold gas that has not evaporated yet continues falling down. During the first $\approx 600\,\mathrm{Myr}$, the velocities seem to increase linearly with time as the gravitational force accelerates the cold gas.

But for $t \gtrsim 600\,\mathrm{Myr}$, drag forces start to decelerate the cold gas as the cloud is eventually torn apart by HD instabilities which increases the effective area (see eq. (2.24)) and thus the strength of the drag forces. In the right panel, one can see that the cold gas has only travelled a distance of about 64 kpc before having lost 80% of its initial mass after $\approx 700\,\mathrm{Myr}$. Clearly, the cold gas in this simulation is not able to reach the inner regions and feed star formation as it would have needed to travel a distance of around $r_{\mathrm{vir}} = 526\,\mathrm{kpc}$.

3.2 Varying simulation parameters

To obtain the results shown in section 3.1 we have made use of different model assumptions that may have influenced our findings. In particular, there are very high uncertainties on the values of (i) the suppression factor of thermal conduction (e.g. Kooij et al. 2021), (ii) the metallicity of the cool circumgalactic clouds (e.g. Prochaska et al. 2017; Wotta et al. 2019; Zahedy et al. 2019), and (iii) the mass of these cold gas clouds (e.g. Werk et al. 2014; Keeney et al. 2017). In this section, we investigate how much our results change if we modify these parameters. In addition, we also examine how reducing the starting radius of the cloud to half the virial radius affects our results.

3.2.1 The suppression factor of thermal conduction

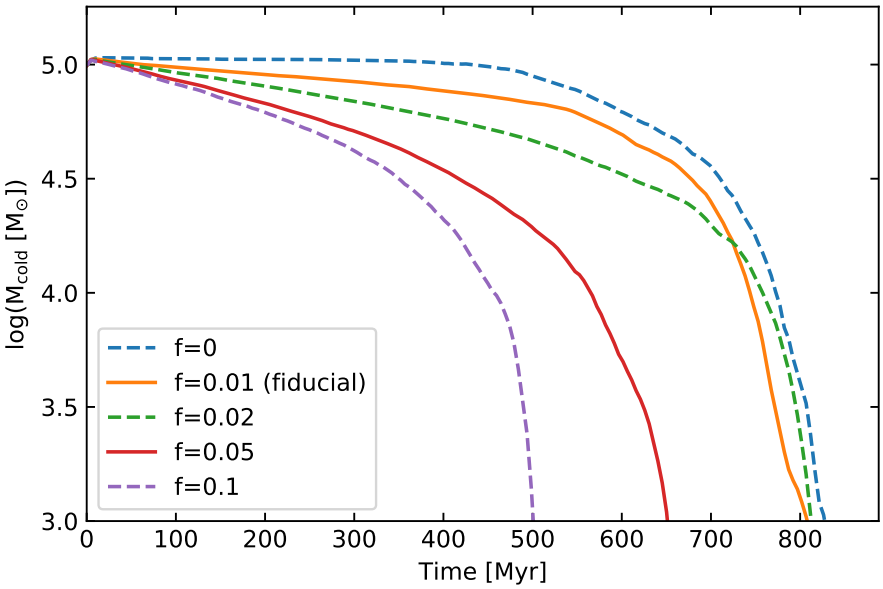

Figure 3.7: Cold gas mass evolution as a function of time for $f \in \{0, 0.01, 0.02, 0.05, 0.1\}$. A dashed line indicates that the simulation has not reached convergence, while a solid line indicates that is has reached convergence. If the solution has not converged, then we use the highest available resolution.

In the literature, a suppression factor of $f = 0.1$ is often assumed (e.g. Armillotta et al. 2017; Tang and Churazov 2018) which has been found to well approximate the actual anisotropic suppression by the magnetic fields in Milky Way-like galactic fountain clouds (Kooij et al. 2021). Yet, for our fiducial simulation we adopted a lower suppression factor of $f = 0.01$, since using $f = 0.1$ led to an extremely quick dispersion of the cold gas cloud — too quick to agree with the observations of cold gas around ETGs. This very high thermal conduction efficiency is due

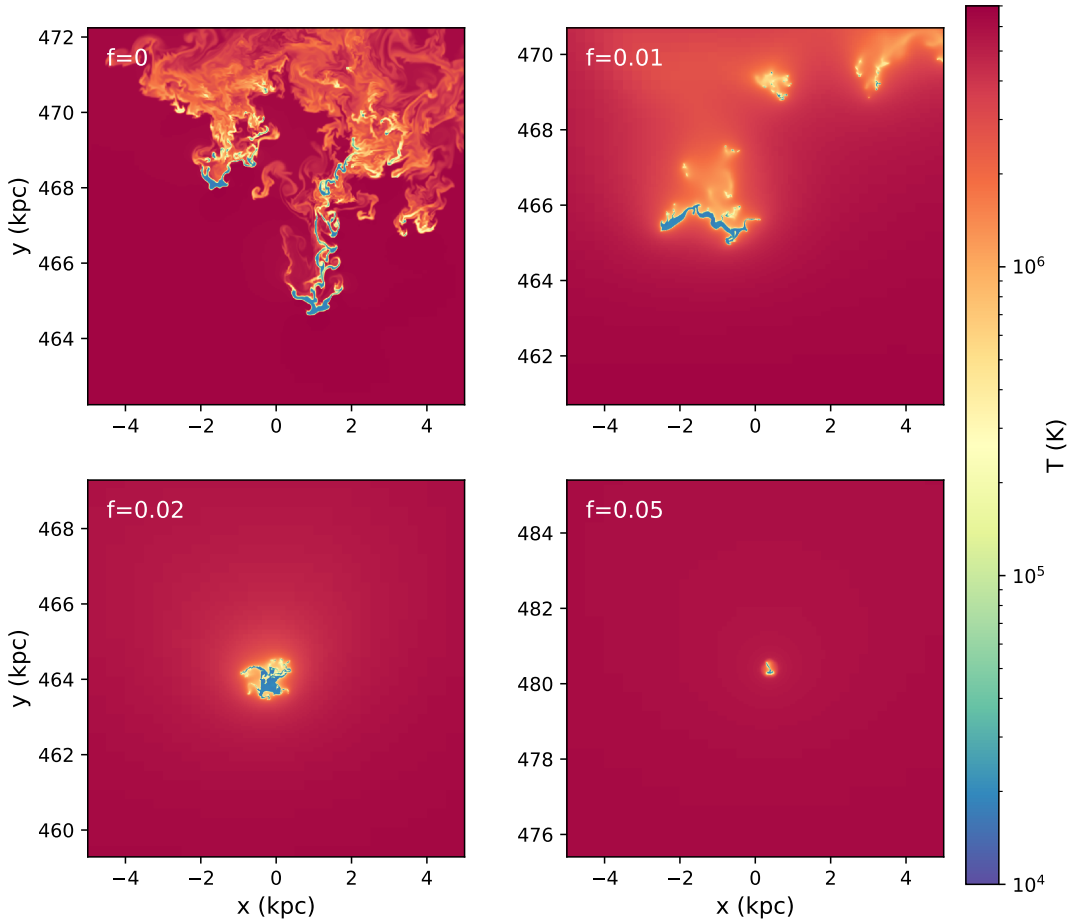

Figure 3.8: Temperature snapshot of the cold cloud at $t = 650\,\mathrm{Myr}$ for suppression factors of $f = 0$ (upper-left), $f = 0.01$ (upper-right), $f = 0.02$ (lower-left), and $f = 0.05$ (lower-right). The cloud has a starting radius of $r_{\mathrm{start}} = r_{\mathrm{vir}}$, a metallicity of $\mathrm{Z_c} = 0.3\,\mathrm{Z_\odot}$, and a starting mass of $M_{\mathrm{c}} = 10^5\,\mathrm{M_\odot}$ in all four cases.

to the higher temperature contrast between the cold gas and the hot corona in massive ETGs relative to Milky Way-like galaxies. It furthermore implies that whatever the value of f is in massive ETGs, it will likely be below $f = 0.1$ (at least in setups similar to ours).

The general trend of the suppression factor is that a higher value for f leads to a quicker cloud dissolution as the Field length increases as a function of f (see section 4.1.1 for a more detailed analysis on the Field length). Yet, at the same time, thermal conduction can also lead to a longer survival time by protecting the cloud from being torn apart by HD instabilities. The effect of various values for f on the cold mass evolution is shown in Figure 3.7, where one can see the cold gas mass as a function of time for suppression factors ranging from $f = 0$ to $f = 0.1$. At first glance, this plot implies that for $f = 0$, $f = 0.01$ and $f = 0.02$ the cold gas survives for a comparably long time, while for the higher values of f the cloud seems to quickly evaporate (especially for $f = 0.1$). Note, however, that the simulations with $f = 0$, $f = 0.02$, and $f = 0.1$ have not reached *convergence* (indicated by dashed lines). With having reached convergence we mean that the results of the simulations are not expected to change appreciably for higher grid resolutions. Achieving convergence is typically very challenging in any simulation. However, there are indications that these types of simulations can indeed reach convergence at parsec

scales when $f \gtrsim 0.01$ and when the Field length is well resolved (Armillotta et al. 2017; Kooij et al. 2021). This is not the case for $f = 0$ where thermal conduction is absent. In fact, McCourt et al. 2018 have shown that with cooling and no thermal conduction, the cold cloud will tend to shatter into tiny fragments with sizes much smaller than the resolution of our simulations. As a result, the HD instabilities that arise in $f = 0$ are not fully resolved and the cloud's lifetime is artificially prolonged (see section 4.2.1 for a convergence test). Nevertheless, it is important to understand how the various suppression factors (converged or not) will influence the evolution of the infalling cloud. To this end, we focus on how the results of our fiducial simulation ($f = 0.01$) differ if we change the suppression factor to $f = 0$, $f = 0.02$, and $f = 0.05$.

Temperature subplots of the cold cloud at $t = 650\,\mathrm{Myr}$ for suppression factors of 0, 0.01, 0.02, and 0.05 are shown in Figure 3.8. When $f = 0$ (no thermal conduction), HD instabilities can form freely and strip the cold cloud of its cold gas. The cloud consequently fragments and spreads out over a significantly larger surface area than when $f > 0$. Cooling is still present, but far too weak to prevent the cold gas from evaporating. We deem, however, this scenario unlikely since the coronal media of ETGs are ionized and have high temperatures of $T \sim 10^{6-7}\mathrm{K}$, meaning that thermal conduction must undoubtedly play a role. For $f = 0.01$, we notice that the cold cloud spreads out over a smaller surface area as the HD instabilities get suppressed, but it is nevertheless still capable of stripping the cloud of its cold gas, producing, however, a much smoother wake than when $f = 0$. For $f = 0.02$ and $f = 0.05$, on the other hand, the cold cloud remains compact because the higher thermal conduction efficiency suppresses the HD instabilities enough to prevent any significant mass stripping. However, for $f = 0.05$ the thermal conduction has become so efficient that it has practically evaporated the entire cloud after around 650 Myr.

Cold gas mass

The fitted cold gas mass loss for $f = 0$, $f = 0.02$, and $f = 0.05$ are shown in Figure 3.9, Figure 3.10, and Figure 3.11, respectively. Interestingly, for $f = 0$ there seems to be almost no mass loss for the first $\approx 400\,\mathrm{Myr}$, while for $f = 0.02$ and $f = 0.05$ mass starts to evaporate from the start (albeit at a low rate). For both $f = 0$ and $f = 0.02$, the cloud has lost 80% of its initial mass after roughly 700 Myr (analogous to the $f = 0.01$ case), while it only takes about 500 Myr for $f = 0.05$. The corresponding velocity profiles of $f = 0$ and $f = 0.02$ indicate that they both travel about the same distance as the fiducial simulation ($\approx 64\,\mathrm{kpc}$) before losing 80% of its initial mass. For $f = 0.05$, the travelled distance is half of that ($\approx 28\,\mathrm{kpc}$) as the overly efficient thermal conduction leads to more momentum transfer between the cloud and the corona, which impedes the acceleration of the infalling cloud (Brüggen and Scannapieco 2016). Nevertheless, these results all yield the same qualitative result of the cold gas evaporating before reaching the central galaxy, which is in agreement with our findings of the fiducial simulation.

When looking at the mass loss and evaporation rate predicted by the analytical model, it becomes clear that especially $f = 0.02$ agrees very well for the first $\approx 400\,\mathrm{Myr}$, with an average evaporation rate of $\bar{\alpha}_{\mathrm{sim}} = 1.5\,\mathrm{Gyr}^{-1}$. Yet, we note that this is purely coincidental since the analytical model does not explicitly incorporate the effects of thermal conduction and cooling.

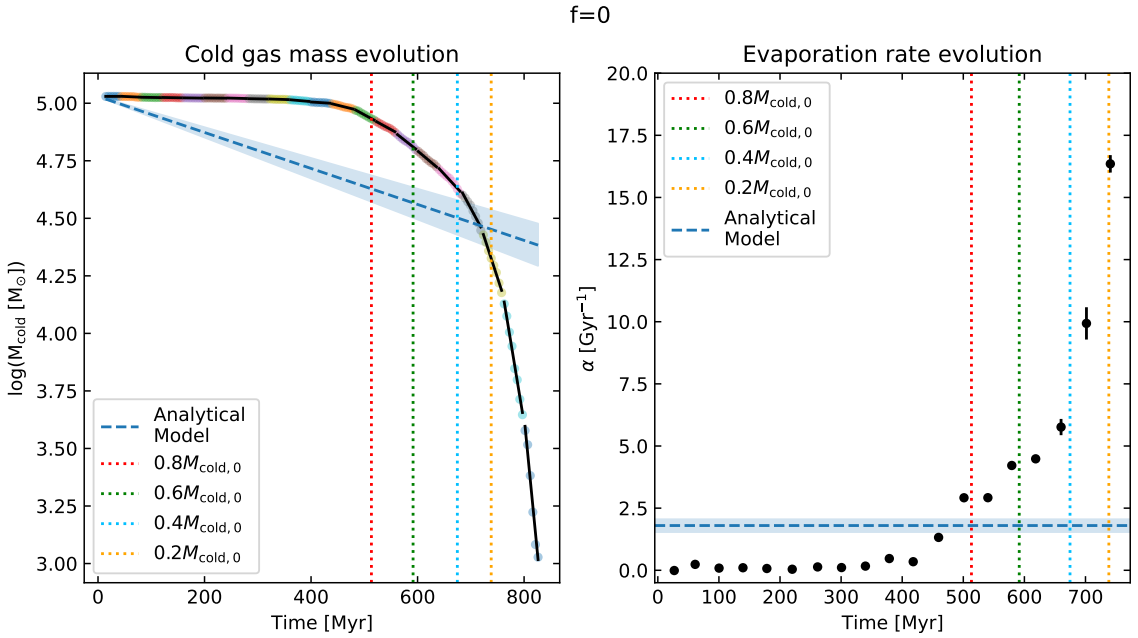

Figure 3.9: Cold gas mass loss as a function of time for the f0L simulation ($f = 0$). We plot the data in segments of 40 Myr which are separately fitted by an exponential decay function (see caption of Figure 3.3 for more details). Note that here the accelerated mass loss is only due to HD instabilities (since there is no thermal conduction) which speed up the evaporation process by fragmenting the cold cloud into smaller cloudlets.

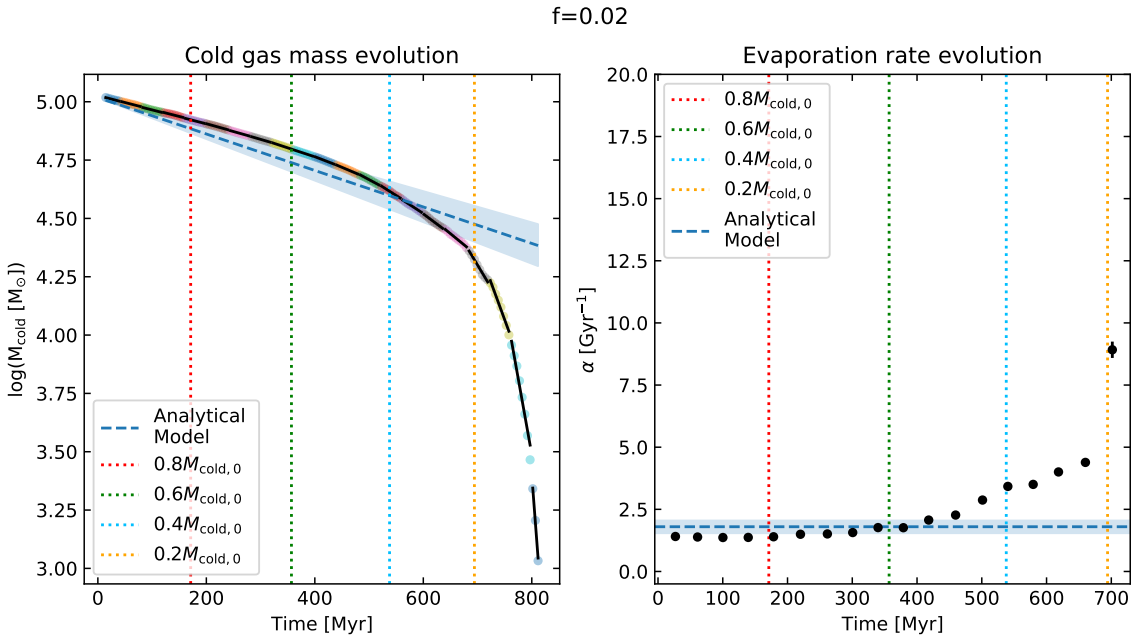

Figure 3.10: Cold gas mass loss as a function of time for the f2VH simulation ($f = 0.02$). We plot the data in segments of 40 Myr which are separately fitted by an exponential decay function (see caption of Figure 3.3 for more details).

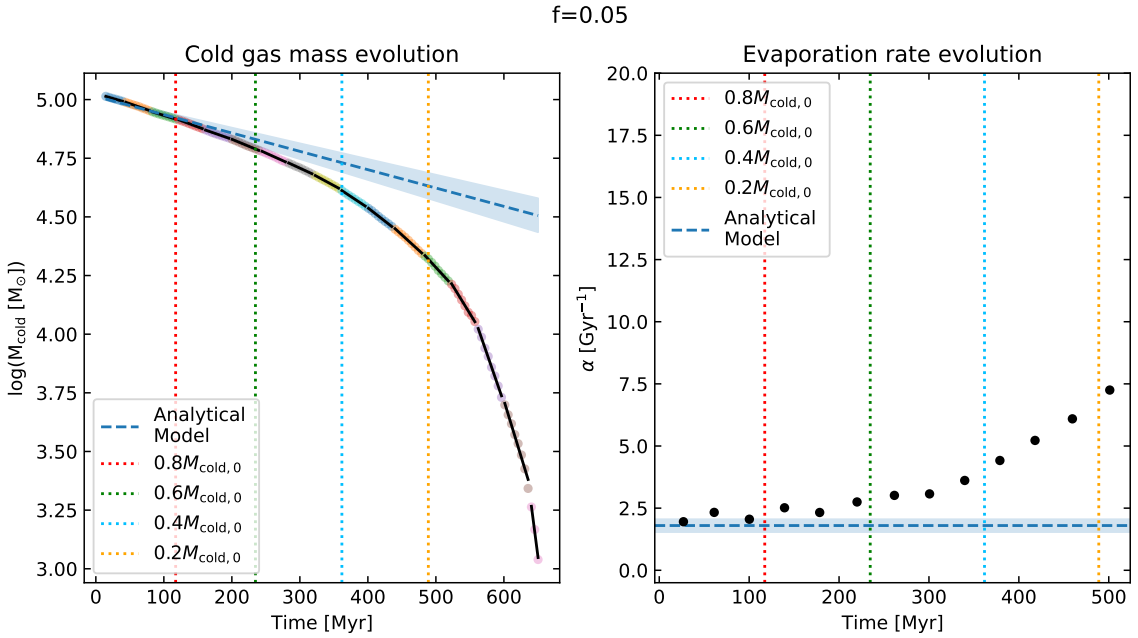

Figure 3.11: Cold gas mass loss as a function of time for the f5H simulation ($f = 0.05$). We plot the data in segments of 40 Myr which are separately fitted by an exponential decay function (see caption of Figure 3.3 for more details).

3.2.2 The cloud metallicity

So far we have assumed that the cloud has the same metallicity as the coronal medium ($Z_c = Z_{cor} = 0.3\,Z_\odot$). Yet, this assumption implies that the cloud must have condensed out of the hot corona, even though we assume that the cold gas originates from the metal-poor IGM. It would therefore be more consistent to let the cloud have a metallicity comparable with that of the IGM. To this end, we reduce the cloud's metallicity to $0.05\,Z_\odot$ (e.g. Cooper et al. 2015; Glidden et al. 2016)[2] while keeping the metallicity of the corona at a value of $0.3\,Z_\odot$ and the suppression factor at $f = 0.01$.

In Figure 3.12, one can see the density evolution at roughly $t = 250\,\mathrm{Myr}$, $t = 500\,\mathrm{Myr}$, and $t = 750\,\mathrm{Myr}$. Comparing this with Figure 3.1, we notice a stronger elongation along x at $t = 500\,\mathrm{Myr}$ for the metal-poor cloud ($0.05\,Z_\odot$) relative to the more metal-rich cloud ($0.3\,Z_\odot$). It furthermore seems that the lifetime of the metal-poor cloud is shorter as it has almost completely evaporated at $t = 750\,\mathrm{Myr}$. This becomes more evident when looking at the cold gas mass loss as a function of time in Figure 3.13; it takes the low metallicity cloud $\approx 650\,\mathrm{Myr}$ to lose 80% of its initial mass, while the high metallicity cloud takes around $\approx 700\,\mathrm{Myr}$. Clearly, a lower metallicity cloud will survive for a shorter amount of time as its weaker cooling is less capable of slowing down the evaporation of the cold gas. This also causes the cold gas to travel a slightly shorter distance ($\approx 54\,\mathrm{kpc}$) than the fiducial simulation ($\approx 64\,\mathrm{kpc}$). Because these differences are marginal, we justify the simplifying assumption of using a constant metallicity (i.e. $Z_c = Z_{cor} = 0.3\,Z_\odot$) in the other simulations.

[2]Note that the metallicity of the IGM is very uncertain since the estimates are based on photo-ionization models.

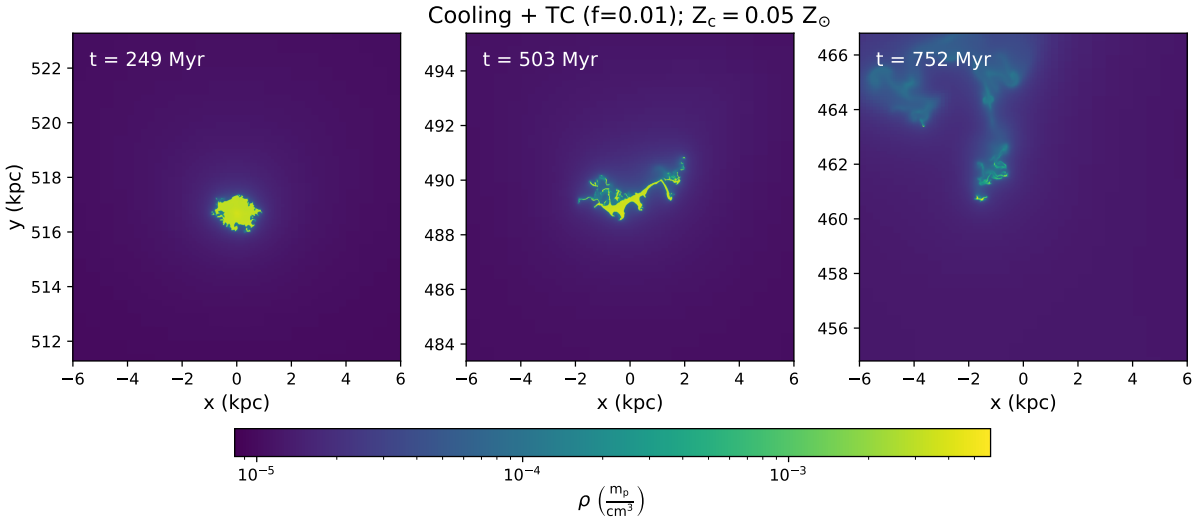

Figure 3.12: Density map at three time instances for the f1H-Z simulation ($f = 0.01$ with a cloud metallicity of $Z_c = 0.05\,Z_\odot$).

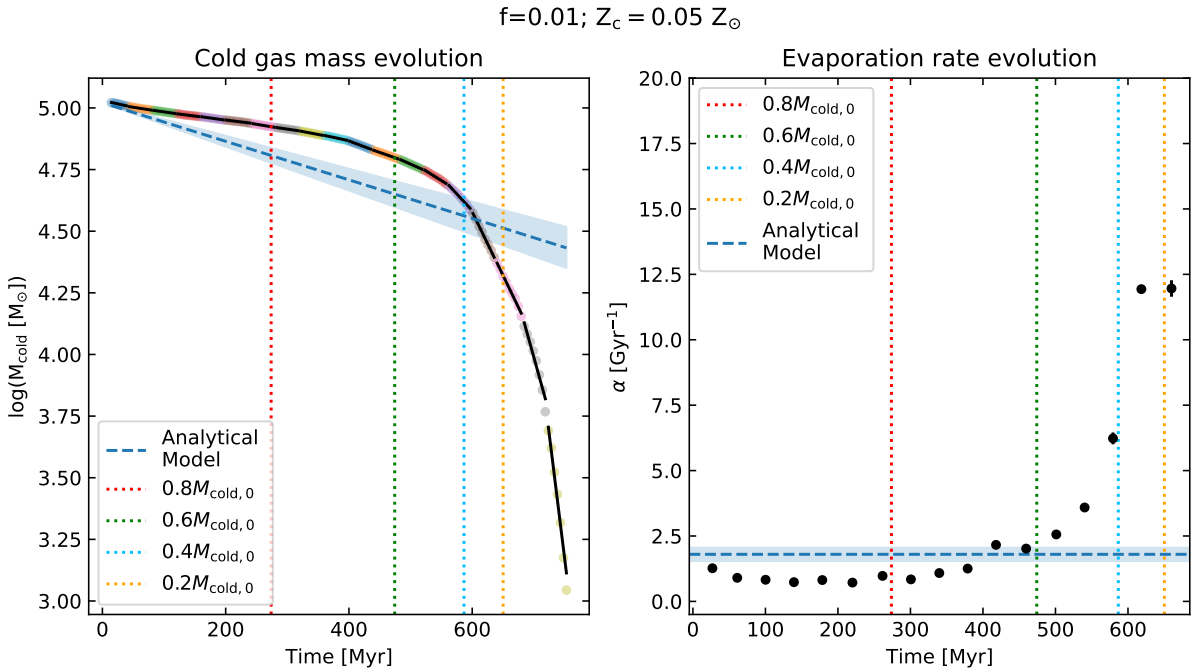

Figure 3.13: Cold gas mass loss as a function of time for the f1H-Z simulation ($f = 0.01$ with a cloud metallicity of $Z_c = 0.05\,Z_\odot$). We plot the data in segments of 40 Myr which are separately fitted by an exponential decay function (see caption of Figure 3.3 for more details).

3.2.3 The initial cloud mass

From the results described in the previous sections it has become clear that cold gas clouds with a mass of $10^5\,M_\odot$ are not able to reach the inner regions of the galaxy, irrespective of whether the cloud metallicity is equal to $0.05\,Z_\odot$ or $0.3\,Z_\odot$. Afruni et al. 2019 found that a cloud mass of $10^5\,M_\odot$ most closely matches the kinematics of the cool CGM clouds as observed by the COS-LRG survey. But there are, however, uncertainties on this value, given the assumptions made for the analytical analysis as well as the large uncertainty on the total cool CGM mass in ETGs (e.g. Werk et al. 2014; Keeney et al. 2017). Therefore, these cold clouds around ETGs might have a higher or lower mass than the assumed $10^5\,M_\odot$. In particular, it is interesting to see how much longer the cloud survives if we increase its mass to $10^6\,M_\odot$, as a higher mass leads to a longer cloud crushing time scale (see section 1.3). Note that increasing the cloud's mass does not lead to a higher density since that is determined by the height above the galactic center, but it does increase the cloud radius from $R_c = 0.71\,\mathrm{kpc}$ to $R_c = 1.53\,\mathrm{kpc}$. The other simulation parameters remain the same as in the fiducial simulation.

In Figure 3.14, the density of the higher mass cloud is shown at approximately 300, 600, and 900 Myr after its initial infall from the virial radius. The first thing we notice is that the cloud takes more time to deform from a nearly spherical shape than when its mass was $10^5\,M_\odot$ (see Figure 3.1). This is to be expected since higher mass clouds are less susceptible to drag forces (Afruni et al. 2019), which are responsible for deforming the cloud. The combination of a longer cloud crushing time and a higher resistance against drag forces, leads to a slower growth of instabilities as well as a longer cloud deformation time. Moreover, it takes more time for the HD instabilities to disrupt the cloud and fragment it into cloudlets smaller than the Field length, resulting in a longer lifetime. This can be seen in Figure 3.15, where we see that it takes around $\approx 1000\,\mathrm{Myr}$ for the cold cloud to lose 80% of its initial cold gas mass. Note that the evaporation rate of this simulation remains approximately constant (as the analytical model would assume) up to $t \approx 750\,\mathrm{Myr}$. We find that the mean of those constant values for α is equal to $\bar{\alpha}_{\mathrm{sim}} = 0.3\,\mathrm{Gyr}^{-1}$, which is significantly lower than $\bar{\alpha}_{\mathrm{sim}} = 1\,\mathrm{Gyr}^{-1}$ as was found in our fiducial simulation. At $t \gtrsim 750\,\mathrm{Myr}$, the cloud transitions to its accelerated mass loss rate and rapidly loses its remaining mass in about $\approx 350\,\mathrm{Myr}$.

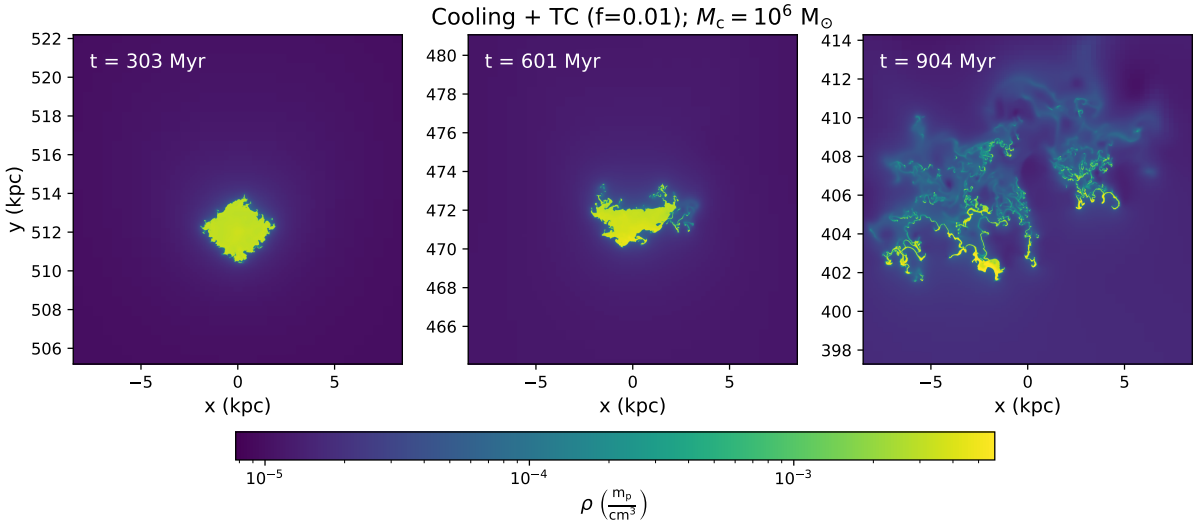

Figure 3.14: Density map at three time instances for the f1H-M simulation ($f = 0.01$ with an initial cloud mass of $M_c = 10^6\,M_\odot$).

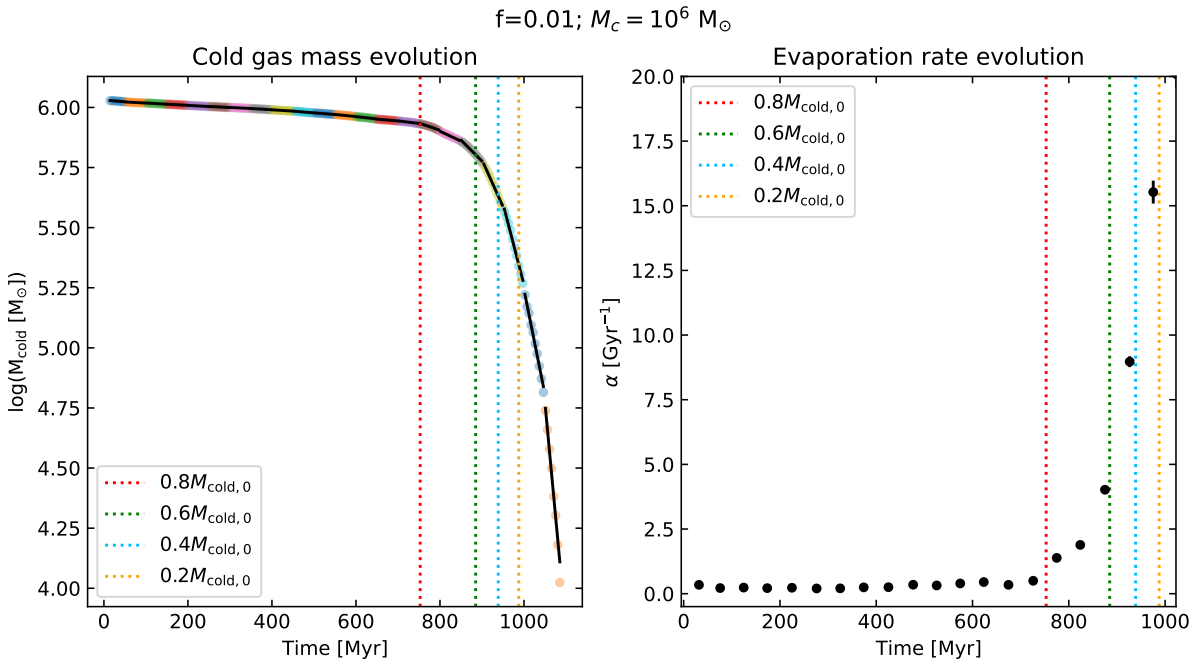

Figure 3.15: Cold gas mass loss as a function of time for the f1H-M simulation ($f = 0.01$ with an initial cloud mass of $M_c = 10^6\,M_\odot$). We plot the data in segments of 50 Myr which are separately fitted by an exponential decay function (see caption of Figure 3.3 for more details). Here we also show the simulation data up to the point where it has lost 99% of its initial mass, which is in this case $M_c = 10^4\,M_\odot$.

Also notice how the vertical lines indicating the percental mass loss are quite clustered at a relatively late time, whereas they are more spread out in the fiducial simulation with $M_c = 10^5\,M_\odot$ (see Figure 3.3). This implies that the dual effect of the thermal conduction is amplified for a cloud with a mass of $10^6\,M_\odot$; the cloud is protected against HD instabilities for a longer time, but it evaporates even more rapidly once the size of the cloudlets has become smaller than the Field length. Most notably, increasing the mass to $10^6\,M_\odot$ allows the cold gas to travel a distance of about 135 kpc — roughly twice the distance of the fiducial simulation — before evaporating. Nevertheless, it would still have needed to travel an additional ≈ 400 kpc in order to reach the central galaxy.

Unfortunately, we cannot draw a comparison between the analytical model here since $\alpha = 1.8\,\mathrm{Gyr}^{-1}$ is only appropriate for a cloud mass of $10^5\,M_\odot$ (Afruni et al. 2019).

3.2.4 The starting radius

Our assumption of letting the cloud fall in from the virial radius is predicated on the expectation that they originate from the IGM. However, these cold clouds might also originate from the hot coronal gas due to thermal instabilities (e.g. McCourt et al. 2012; Sharma et al. 2012; Voit 2018) and may therefore be located at distance that is different from the virial radius. In particular, thermal instabilities are more likely to occur closer to the galactic center where the density of the corona is higher (see Figure 2.5). To that end, we place the cloud at a distance equal to half the virial radius from the galactic center. We choose this particular value so that we can compare our results with the analytical prediction of Afruni et al. 2019 who also investigated the survival of the cold cloud at $r_{start} = r_{vir}/2$. Like with the preceding sections, we only change one parameter of the fiducial simulation. Nevertheless, it is worth noting that the assumed cloud metallicity of $Z_c = Z_{cor} = 0.3\,Z_\odot$ of the fiducial simulation is actually more appropriate here (even though the

exact value is still uncertain), since a cloud that forms due to thermal instabilities should have the same metallicity as the corona.

As explained in the method section, the density of the corona increases as the distance to the galactic center decreases. Because the cloud and the corona are assumed to be in pressure equilibrium, the cold cloud will therefore also increase its density when it gets closer to the galactic center. The cloud will thus attain a higher initial density when we place it at $r_{\rm vir}/2$ in the initial conditions. For an initial mass of $10^5\,{\rm M}_\odot$, we find that reducing the infall radius to $r_{\rm vir}/2 = 263\,{\rm kpc}$ leads to a smaller cloud radius of $R_{\rm c} = 0.44\,{\rm kpc}$ (see eq. (2.15)).

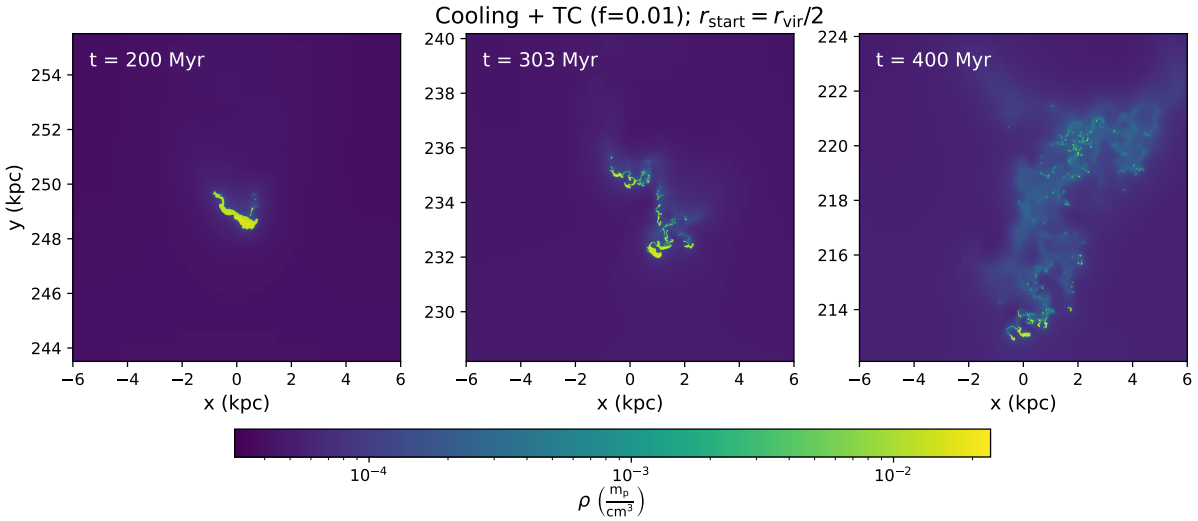

Figure 3.16: Density map at three time instances for the f1H-r simulation ($f = 0.01$ and a starting radius of $r_{\rm start} = r_{\rm vir}/2$). Note that the density values on the colourbar are now higher than if the cloud would start at the virial radius.

The density evolution of the cloud starting at half the virial radius at approximately $t = 200\,{\rm Myr}$, $t = 300\,{\rm Myr}$, and $t = 400\,{\rm Myr}$ is shown in Figure 3.16. Notice that, due to the higher density of the cloud, we use a different colour scale than the one we used in the fiducial simulation (see Figure 3.1). It is, furthermore, evident that the cloud evaporates way faster when it starts at $r_{\rm vir}/2$ than when it starts at $r_{\rm vir}$ since it has almost completely disintegrated at $t = 400\,{\rm Myr}$. We see this also in Figure 3.17 where 80% of the initial cloud mass is lost after $\approx 400\,{\rm Myr}$ (while it took the fiducial simulation $\approx 700\,{\rm Myr}$ to lose the same amount of cold gas). This higher destruction rate was also predicted by Afruni et al. 2019, who found that the analytical evaporation rate would increase from $\alpha = 1.8^{+0.25}_{-0.26}\ {\rm Gyr}^{-1}$ for $r_{\rm start} = r_{\rm vir}$ to $\alpha = 2.4^{+0.52}_{-0.55}\ {\rm Gyr}^{-1}$ for $r_{\rm start} = r_{\rm vir}/2$. Even though this new value for α overpredicts the initial mass loss and evaporation rate of our simulation (see Figure 3.17), the results of a faster cloud destruction are qualitatively the same.

As for the velocity evolution, we find that the cloud experiences a stronger gravitational acceleration since it is closer to the galactic center, but also a stronger deceleration due to drag forces as the density of the coronal medium is higher. The cloud manages to traverse a distance of $\approx 47\,{\rm kpc}$, which is still largely insufficient to reach the inner regions of the galaxy.

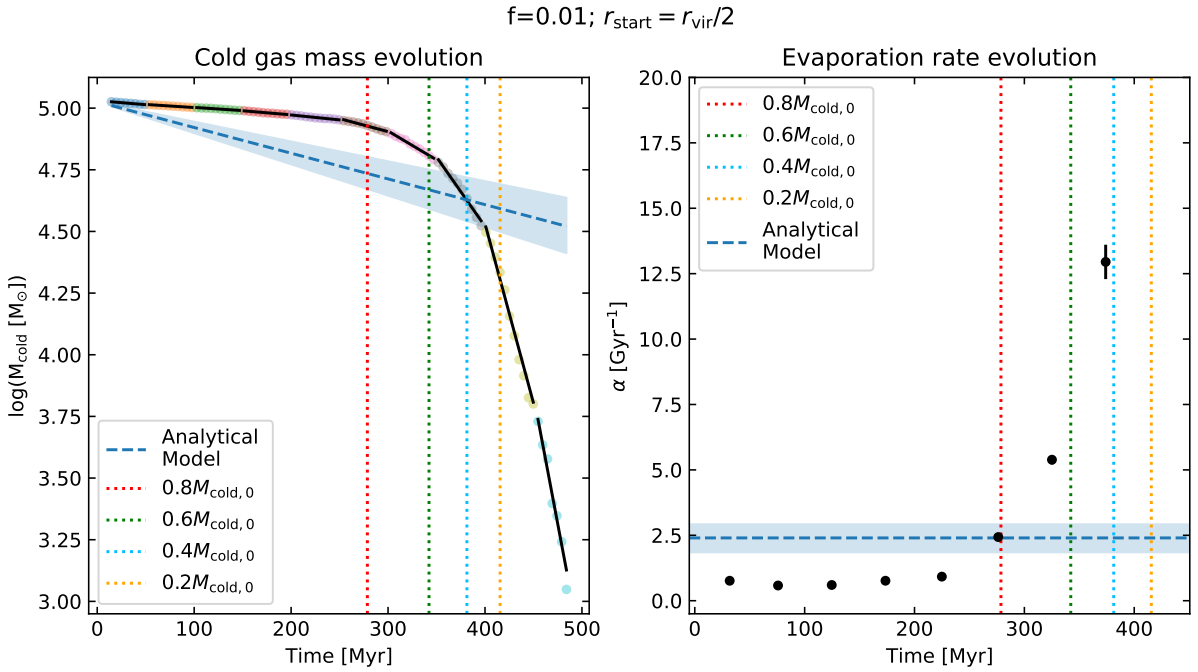

Figure 3.17: Cold gas mass loss as a function of time for the f1H-r simulation ($f = 0.01$ and a starting radius of $r_{start} = r_{vir}/2$). We plot the data in segments of 50 Myr which are separately fitted by an exponential decay function (see caption of Figure 3.3 for more details). The evaporation rate according to the analytical model is for $r_{start} = r_{vir}/2$ estimated to be $\alpha = 2.4^{+0.52}_{-0.55}$ Gyr^{-1} (Afruni et al. 2019).

3.3 Summary of the results

Qualitatively, all the results of the simulations that we compiled in Table 2.2 are the same: the cold gas cloud evaporates in the hot corona before reaching the inner regions of the galaxy. But how long the cloud survives and how far it travels depends strongly on our simulation parameters. This is summarized in Figure 3.18, where one can see how the results of the fiducial simulation changes when we vary the suppression factor for thermal conduction (f), the cloud metallicity, the initial cloud mass, and the starting radius of the cloud. Comparing the results with respect to the fiducial simulation (blue cross), we can make the following general observations:

- Increasing the suppression factor beyond $f = 0.02$ leads to an almost linear decrease in the survival time for the cloud.
- Lowering the cloud metallicity from $0.3\,Z_\odot$ to $0.05\,Z_\odot$ slightly decreases the survival time of the cloud.
- Increasing the cloud mass from $10^5\,M_\odot$ to $10^6\,M_\odot$ leads to a weaker drag force and results in a roughly 50% longer survival time as well as a doubling in the travelled distance.
- Decreasing the starting radius to half the virial radius leads to a stronger drag force and roughly reduces the survival time by 40% and the travelled distance by 30%.

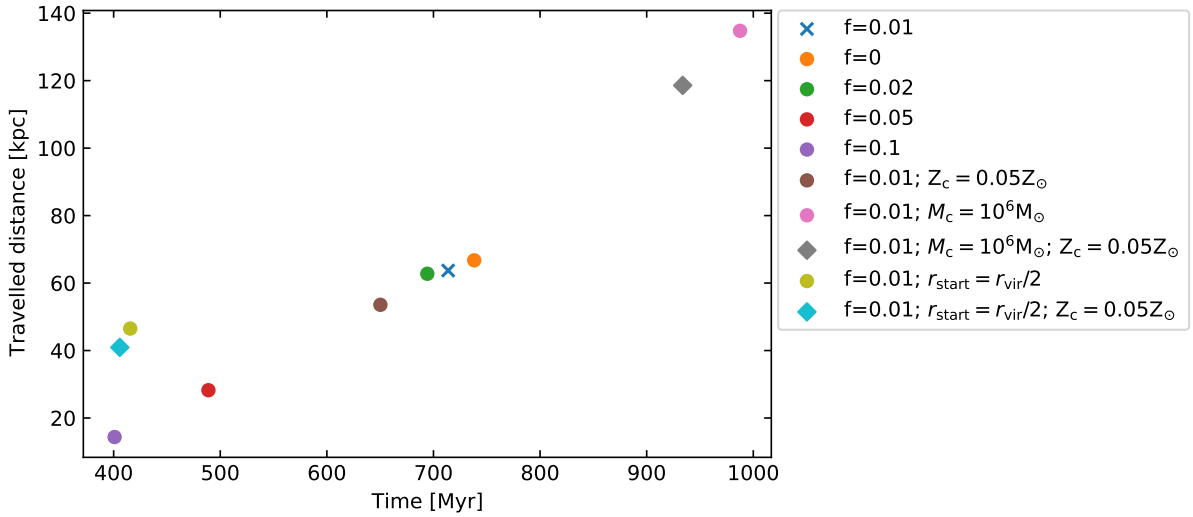

Figure 3.18: Summary plot showing the elapsed time (x-axis) and distance travelled (y-axis) for the cold gas to lose 80% of its initial mass. The cross indicates the fiducial simulation, the dots represent the simulations where one parameter has been changed with respect to the fiducial simulation, and the diamonds are the simulations where two parameters have been changed (with respect to the fiducial simulation).

Chapter 4

Discussion

We have found, via 2D hydrodynamical simulations, that an infalling cold cloud will evaporate in the hot coronal medium of an ETG long before it can reach the galactic center. This result is also in line with the analytical predictions of Afruni et al. 2019. In this chapter, we analyze our results further and draw some further comparisons with the analytical model. After that, we also discuss the limitations as well as the validity of our simulations.

4.1 Analysis of the results

4.1.1 The Field length

In section 3.2.1, we have shown that a cloud with a mass of $10^5\,M_\odot$ and a starting radius of $r_{\rm start} = r_{\rm vir} = 526\,{\rm kpc}$ evaporates increasingly faster for $f > 0.05$ (where f is the suppression factor of thermal conduction), while for $f = 0.01$ and $f = 0.02$ the cloud survives approximately as long as for $f = 0$ (no thermal conduction, see Figure 3.7). Note, however, that the $f = 0$ curve in Figure 3.7 is our least converged simulation (see Figure 4.4), which may imply that the used grid resolution is not enough to fully resolve the HD instabilities. This would, consequently, lead to an artificial extension of the cloud's lifetime (see section 4.2.1 for more detailed information). It therefore seems likely that for $f = 0.01$ and $f = 0.02$ the cloud would survive longer than for $f = 0$ (if it would have converged), indicating that for these low suppression factors, thermal conduction is able to protect the cloud against disruption by HD instabilities.

Whether or not the thermal conduction will protect a cloud against destruction depends (roughly) on how the size of the cloud ($\lambda_{\rm c} = 2R_{\rm c}$, where $R_{\rm c}$ is the cloud radius) and the Field length ($\lambda_{\rm F}$) relate to one another. The Field length[1] is defined as (Field 1965; Begelman and McKee 1990; McKee and Begelman 1990):

$$\lambda_{\rm F} \equiv \left(\frac{f \kappa_{\rm Sp} T_{\rm cor}}{n_{\rm c}^2 \tilde{\Lambda}(T_{\rm c})} \right)^{1/2}, \tag{4.1}$$

where $\kappa_{\rm Sp} = 5.6 \times 10^{-7} T_{\rm cor}^{5/2}$ is the Spitzer conductivity at the coronal temperature ($T_{\rm cor}$), $f \leq 1$ the suppression factor, $n_{\rm c}$ the number density of the cold gas, and $\tilde{\Lambda}(T_{\rm c})$ the cooling function of the cold gas at a temperature of $T_{\rm c} = 2 \times 10^4\,{\rm K}$. When $\lambda_{\rm c} < \lambda_{\rm F}$, conduction will be effective and can smooth out the density/temperature gradient of the entire cloud, leading to rapid evaporation. Conversely, when $\lambda_{\rm c} > \lambda_{\rm F}$, conduction will be less effective and can therefore

[1] In this case, we are looking at the efficacy of thermal conduction in terms of size. But one could also look at it in terms of time by comparing the conduction timescale with the cooling timescale.

only smooth out the cloud-corona interface, thereby potentially suppressing the onset of HD instabilities. In addition, if the grid resolution is significantly smaller than the Field length, then convergence may be reached at a lower resolution (see section 4.2.1 for an analysis on the convergence for various values of f).

While we know that $T_{\rm cor}$ is a constant (since we assume an isothermal corona), we will also assume $\tilde{\Lambda}(T_{\rm c})$ to be a constant. In reality, this value will differ depending on the metallicity, but at a temperature of $2 \times 10^4\,\mathrm{K}$ the cooling functions will only differ by about $\sim 15\%$ between metallicities of $\mathrm{Z} = 0.3\,\mathrm{Z}_\odot$ and $\mathrm{Z} = 0.03\,\mathrm{Z}_\odot$ (see Figure 2.6). We therefore adopt the value of $\tilde{\Lambda}(T_{\rm c})$ corresponding to a cloud metallicity of $0.3\,\mathrm{Z}_\odot$ since that is also the metallicity we assumed when we varied f. Equation (4.1) will thus only depend on f and — because $n_{\rm c}$ decreases as a function of distance from the galactic center (see Figure 2.5) — on the starting radius $r_{\rm start}$. The values of $\lambda_{\rm F}$ for $f \in \{0.01, 0.02, 0.05, 0.1\}$ at starting radii of $r_{\rm vir}$ and $r_{\rm vir}/2$ are shown in Table 4.1. For a cloud mass of $10^5\,\mathrm{M}_\odot$, the cloud has an initial size of $\lambda_{\rm c}(r_{\rm vir}) = 1.42\,\mathrm{kpc}$ at the virial radius and an initial size of $\lambda_{\rm c}(r_{\rm vir}/2) = 0.89\,\mathrm{kpc}$ at half the virial radius. We find that $\lambda_{\rm c}(r_{\rm vir}) \lesssim \lambda_{\rm F}$ for $f > 0.05$ which is in line with our findings that the cloud is rapidly destroyed for suppression factors larger than 0.05, while being protected for $f = 0.01$ and $f = 0.02$ due to the suppression of instabilities. Do note that the cloud will eventually also undergo rapid evaporation for $f \leq 0.02$ once structures smaller than the Field length are produced due to mass stripping and/or cloud contraction.

For a starting radius at half the virial radius, we find that $\lambda_{\rm F}$ decreases by a factor of about 4, while $\lambda_{\rm c}(r_{\rm vir}/2)$ is only about ~ 1.6 times smaller than $\lambda_{\rm c}(r_{\rm vir})$. This implies that clouds that form deeper in the galactic corona can withstand higher values of f due to their higher density.

Table 4.1: Field length for various suppression factors at a distance of $r_{\rm vir}$ and $r_{\rm vir}/2$ from the galactic center.

Field length	$f = 0.01$	$f = 0.02$	$f = 0.05$	$f = 0.1$
$\lambda_{\rm F}(r_{\rm vir})$	0.80 kpc	1.13 kpc	1.78 kpc	2.52 kpc
$\lambda_{\rm F}(r_{\rm vir}/2)$	0.20 kpc	0.28 kpc	0.44 kpc	0.62 kpc

4.1.2 The effect of cooling

In all simulations we have included the effects of cooling, but in none of them did we see an increase in cold gas mass due to condensation. This is because the coronal temperature is so high that any mixed gas will inevitably evaporate. Cooling can therefore only delay the evaporation of the cold gas. When we reduced the cloud metallicity of our fiducial simulation from $0.3\,\mathrm{Z}_\odot$ to $0.05\,\mathrm{Z}_\odot$, we saw that the lower metallicity cloud only had a slightly shorter lifetime due to its less efficient cooling. The difference in cooling efficiency was thus not that prominent. We therefore ran some additional simulations under conditions for which we expected the differing metallicities of $0.3\,\mathrm{Z}_\odot$ and $0.05\,\mathrm{Z}_\odot$ to have a strong effect on the efficiency of the cooling. These simulations were f0L-Z-r and f0L-r (see Table 2.2), where we expect a more prominent effect of cooling because (i) thermal conduction is ignored which allows for unhindered mixing and (ii) the density of both the cloud and the corona is higher at half the virial radius which yields a higher cooling rate.

The result is shown in Figure 4.1, where one can see how the low metallicity cloud (orange) has lost 99% of its initial cold gas mass after around $\sim 500\,\mathrm{Myr}$, while it takes around $\sim 1000\,\mathrm{Myr}$

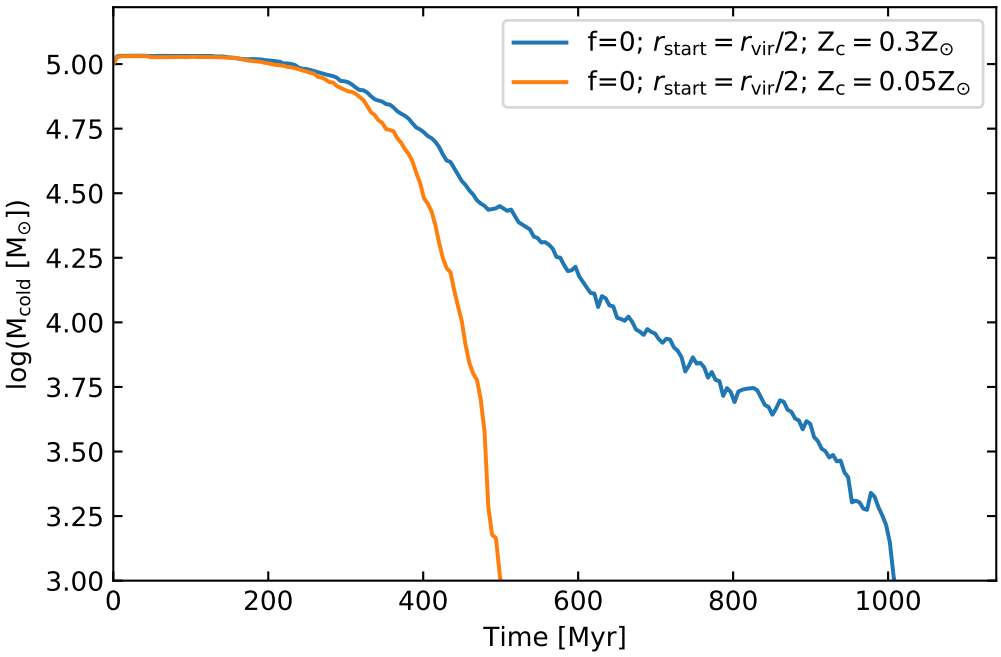

Figure 4.1: Cold gas mass as a function of time for the f0L-Z-r (orange) and f0L-r (blue) simulation (see Table 2.2).

for the high metallicity cloud (blue) to lose the same amount of cold gas. As expected, the higher density allows for a significantly higher cooling rate, which in turn increases the difference in cooling efficiency between the simulations at the two different metallicities (see eq. (2.17)). As a result, the high metallicity cloud is capable of delaying its evaporation for a considerably longer time than the low metallicity cloud. Do note, however, that this can only occur when the thermal conduction is very strongly suppressed to the point that it is close to zero, otherwise the mixed gas would evaporate before the cooling could become effective. Therefore, we conclude that the cooling of the CGM clouds in the hot coronae of ETGs is most likely never strong enough to lead to condensation. Instead, the clouds will tend to evaporate into the hot ambient medium. In fact, the cooling in the coronae of ETGs is in reality probably even weaker than in our simulations since we neglect any source of heating.

4.1.3 Comparison with the analytical model

So far we have seen that the analytical model overpredicts the survival time of the cloud because it assumes a constant exponential mass loss rate. We furthermore saw that the analytical model assumes a monotonic decrease in cloud radius during its infall, while the effective size (R_{eff}) of the cloud in the simulations tends to increase as it gets torn apart by instabilities (see Figure 3.5). This is an important difference since R_{eff} determines the cross section of the cloud which affects the drag force and, in turn, the velocity profile of the infalling cloud. It is therefore interesting to investigate how the analytical velocity profile compares with the velocity profile of the simulations. In order to draw this comparison, we first need to explain the main equations that describe the analytical velocity profile of Afruni et al. 2019:

The motion of a cloud that falls inwards to the galactic center due to gravity can be described

as follows:

$$\frac{\mathrm{d}v_{\mathrm{fall}}}{\mathrm{d}r_{\mathrm{gal}}} = \frac{1}{v_{\mathrm{fall}}(r_{\mathrm{gal}})} \frac{GM(r_{\mathrm{gal}})}{r_{\mathrm{gal}}^2} \ , \tag{4.2}$$

where r_{gal} is the radius centered around the galactic center, $v_{\mathrm{fall}}(r_{\mathrm{gal}})$ the infall velocity of the cloud, and $M(r_{\mathrm{gal}})$ the mass of the DM halo as described by the NFW profile (see eq. (2.9)). As the cloud moves through the hot corona it also experiences a *drag force* which decelerates the cloud (e.g. Marinacci et al. 2011):

$$\dot{v}_{\mathrm{drag}} = -\frac{\pi R_{\mathrm{c}}^2 \rho_{\mathrm{cor}} v^2}{M_{\mathrm{c}}} \ , \tag{4.3}$$

where R_{c} is the cloud radius, ρ_{cor} the coronal mass density, and M_{c} the mass of the cloud. Since the clouds are assumed to be spherical in this model, their radius is defined by:

$$R_{\mathrm{c}} = \left(\frac{3M_{\mathrm{c}}}{4\pi\rho_{\mathrm{c}}} \right)^{1/3} \ , \tag{4.4}$$

where ρ_{c} is the density of the cloud, which increases as the cloud gets closer to the galactic center (Figure 2.5). As a result, the spherical cloud will shrink as a function of r_{gal}. From eqs. (4.3) and (4.4) we also see that lower mass clouds experience a stronger drag force than higher mass clouds. Note that here the drag should decrease as the cloud radius continues to shrink, while the cloud in the simulations should experience a stronger drag force due to its growing effective size.

Unfortunately, the analytical model cannot describe the second-order hydrodynamical effects which eventually tends to destroy the clouds, as we have seen in our simulations (see Chapter 3). Instead, these effects are parameterized with a mass loss equation where gas is stripped at an exponential rate:

$$\frac{\mathrm{d}M_{\mathrm{c}}}{\mathrm{d}r_{\mathrm{gal}}} = -\frac{\alpha M_{\mathrm{c}}}{v}, \tag{4.5}$$

where the parameter α takes the evaporation of the cloud in the hot corona into account.

With both the gravitational and hydrodynamical descriptions at hand, one can combine eqs. (4.2), (4.3) and (4.5) into one main equation:

$$\frac{\mathrm{d}v}{\mathrm{d}r_{\mathrm{gal}}} = \frac{1}{v(r_{\mathrm{gal}})} \frac{GM(r_{\mathrm{gal}})}{r_{\mathrm{gal}}^2} + \frac{\pi R_{\mathrm{c}}^2(r_{\mathrm{gal}}) \rho_{\mathrm{cor}}(r_{\mathrm{gal}}) v(r_{\mathrm{gal}})}{M_{\mathrm{c}}(r_{\mathrm{gal}})}. \tag{4.6}$$

This equation tells us that the cloud is initially accelerated by gravity, but will eventually slow down as it interacts with the hot corona. In order to find $v(r_{\mathrm{gal}})$, we need to solve eqs. (4.5) and (4.6) at the same time since they are coupled. We carry this out with numerical ODE integration (using the SciPy odeint package) where we set $v(r_{\mathrm{start}}) = 0\,\mathrm{km/s}$ and $M_{\mathrm{c}}(r_{\mathrm{start}}) = 10^5\,\mathrm{M}_\odot$ as the initial conditions. The value of the evaporation rate α depends on the starting radius, where $\alpha = 1.8\,\mathrm{Gyr}^{-1}$ for $r_{\mathrm{start}} = r_{\mathrm{vir}}$ and $\alpha = 2.4\,\mathrm{Gyr}^{-1}$ for $r_{\mathrm{start}} = r_{\mathrm{vir}}/2$. Afruni et al. 2019 obtained the values of these parameters from their MCMC fit of the observational data from the COS-LRG sample (Chen et al. 2018; Zahedy et al. 2019).

Figure 4.2 depicts two subplots in which the velocities of the cold gas from various simulations (dashed lines) are overplotted with the analytical velocity profile (black). We only consider the velocity data of the simulations up to the point where 80% of the initial cold gas mass has been lost (i.e. when we consider the cloud to have been crushed). In the left panel, one can see that the velocity profiles for the suppression factors ranging from $f = 0.01$ to $f = 0.1$ agree

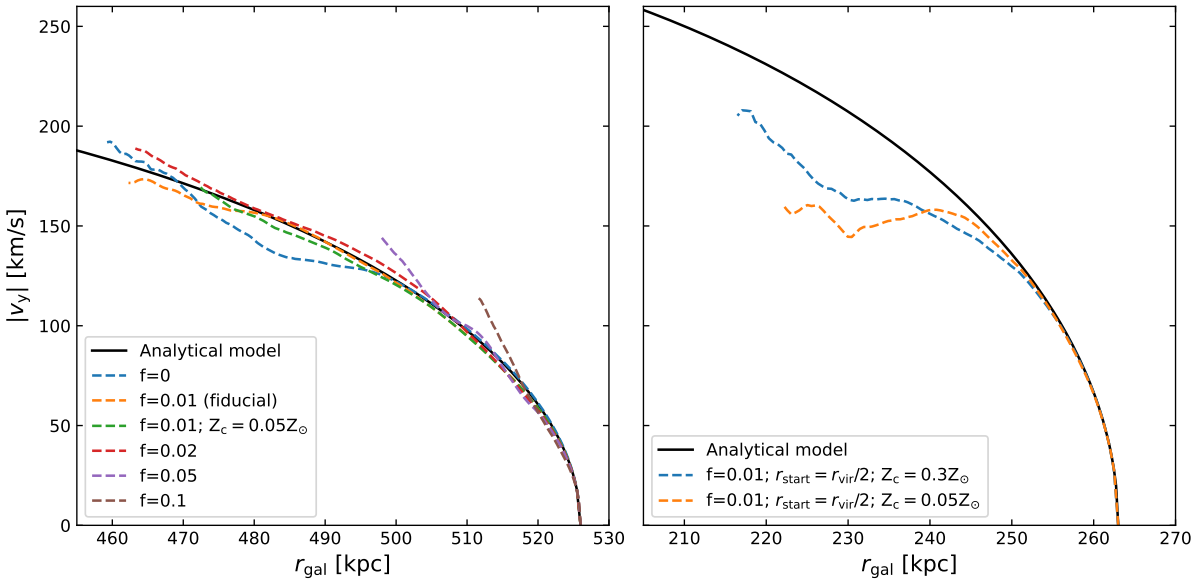

Figure 4.2: Comparison of the cloud velocity according to the analytical model of Afruni et al. 2019 (black line) with the velocity of the cold gas in our simulations (dashed lines). Note that we have taken the absolute value of v_y since we define it to be negative when pointing towards the galactic center.

very well with the analytical model, though they all tend to diverge a bit at the end. $f = 0.1$ and $f = 0.05$ diverge earlier as their survival time is curtailed by the highly efficient thermal conduction, while the lower suppression factors diverge a bit later due to their longer survival time. This divergence at the end is due to the transition to the accelerated mass loss which the analytical model ignores. Note that $f = 0$ has the weakest agreement with the analytical model, but it is also the least converged simulation owing to its lack of thermal conduction. In addition, we also added the velocity profile for $f = 0.01$ with a lower cloud metallicity similar to that of the IGM ($Z_c = 0.05 Z_\odot$; green). Comparing this with the fiducial simulation (orange), for which the metallicity is equal to that of the corona ($Z_c = Z_{cor} = 0.3\,Z_\odot$), we see that the higher metallicity cloud travels a bit farther since its more efficient cooling slightly prolongs the cloud's survival time. In the right panel, the velocity profile for a starting radius at half the virial radius is shown. Here we see a weaker agreement as both the high and low metallicity clouds diverge quite early on. This can be explained by the higher cloud and coronal density at $r_{vir}/2$, which strongly increases the efficiency of the cooling (which the analytical model does not take into account). As a result, the stripped cold gas can survive as multiple small cloudlets (see right panel of Figure 3.16), which makes the drag force significantly different from that of the analytical model (which assumes the drag force of a single spherical cloud).

From this comparison and the results from the previous chapter, we find that all our simulations are in agreement with the theoretical expectation that quiescent galaxies do not accrete gas anymore. We also note that considering a metal-poor cloud — which is more faithful to our assumption that the cloud originates from the IGM — results in a slightly shorter lifetime. What is surprising, however, is that the velocity profiles of our simulations match so well with the analytical model, which does not properly take the hydrodynamical effects into account. We can therefore conclude that the analytic prediction, at least up to the point where the cloud is not highly disrupted by HD instabilities, is a very good approximation of the motion of cool CGM clouds in the hot coronae of ETGs.

4.2 Limitations

Despite that hydrodynamical simulations can incorporate more complexity than an analytical model, they still have limitations. The two main factors that are responsible for these limitations are (i) the finite grid resolution and (ii) the assumptions made by our model.

4.2.1 Convergence tests

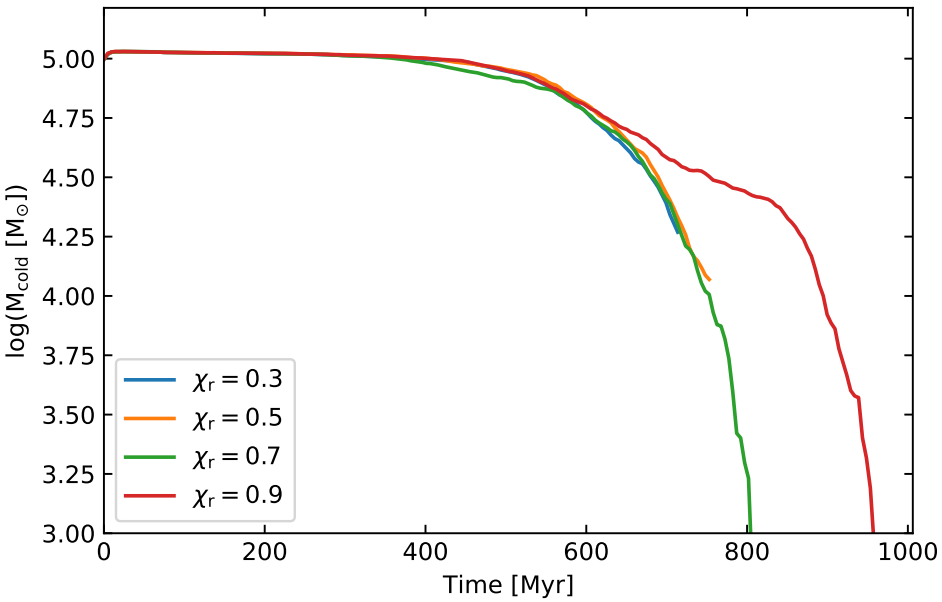

Figure 4.3: Convergence test for refinement threshold values of $\chi_r = 0.3$ (blue), $\chi_r = 0.5$ (orange), $\chi_r = 0.7$ (green), and $\chi_r = 0.9$ (red). The constant simulation parameters that we used here were $f = 0$, $M_c = 10^5\,M_\odot$, $r_{start} = r_{vir}$, $Z_c = 0.3\,Z_\odot$, and a grid resolution of 64 grid cells per kpc ($\mathcal{R}_{64}$). Radiative cooling is included in all cases.

In order to capture the complete behaviour of a gas, one would preferably have a grid with a resolution high enough to fully resolve the HD instabilities and the fragmentation effect of the radiative cooling. Unfortunately, this requires such a high grid resolution that the simulations would become computationally unfeasible. We therefore have to accept that all our results will necessarily contain some inaccuracies. Nevertheless, one can try to reach a grid resolution that is high enough such that the overall results do not appreciably change for increasing resolution. Once that happens, our simulation is said to have reached *convergence*[2]. The first convergence test that we carried out was for the simulations in which we varied the value of the refinement threshold χ_r (see section 2.2.5), which is shown in Figure 4.3. Even though we used the lowest resolution of 64 grid cells per kpc for these simulations, one can still clearly see that $\chi_r = 0.7$ has converged since the result does not change anymore for lower values of χ_r.

As for the simulations in Chapter 3, we noticed that some simulations reach convergence at a lower resolution than others. In particular, a higher suppression factor f generally leads to a faster convergence as the stronger smoothing effect of the thermal conduction produces less small-scale structures. On the other hand, convergence is much harder to reach when we only

[2]Note that here we are dealing with the convergence of the cold gas mass specifically. Other quantities might reach convergence at a different resolution.

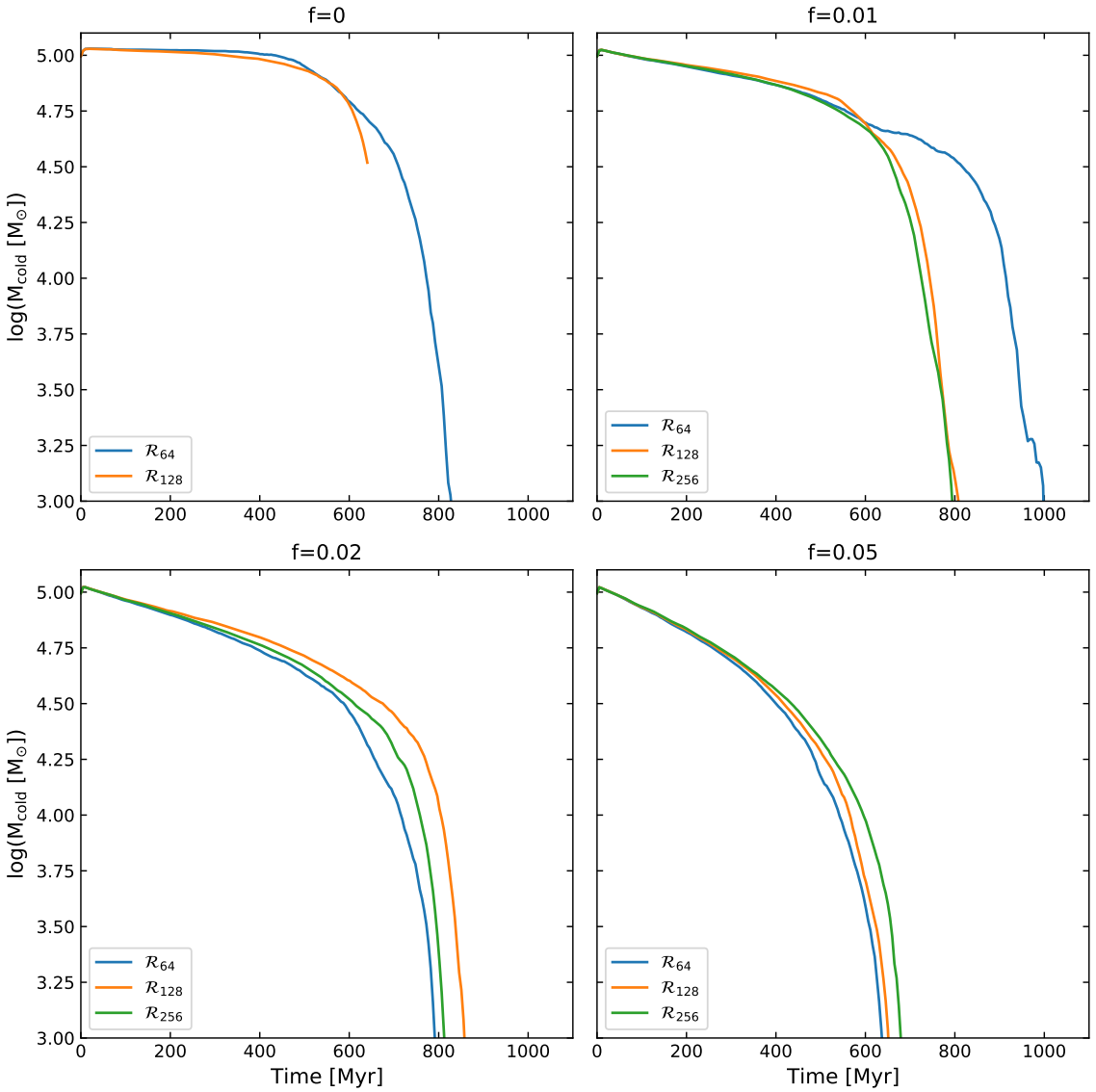

Figure 4.4: Convergence test for suppression factors of $f = 0$ (upper-left) $f = 0.01$ (upper-right), $f = 0.02$ (lower-left), and $f = 0.05$ (lower-right) at various resolutions. The constant simulation parameters that we used here were $M_c = 10^5\,M_\odot$, $r_{start} = r_{vir}$, and $Z_c = 0.3\,Z_\odot$. Radiative cooling is included in all cases.

consider cooling ($f = 0$) due to the increasingly smaller structures that emerge as the cloud undergoes fragmentation (e.g. Armillotta et al. 2016; McCourt et al. 2018; Sparre et al. 2020). This can be seen in Figure 4.4, where the cold gas mass (for clouds with an initial mass of $M_c = 10^5\,M_\odot$) is plotted as a function of time for $f = 0$, $f = 0.01$, $f = 0.02$, and $f = 0.05$ at resolutions of 64 ($\mathcal{R}_{64}$; blue), 128 ($\mathcal{R}_{128}$; orange), and 256 ($\mathcal{R}_{256}$; green) grid cells per kpc. For $f = 0$, one can see that convergence has not been attained as the incomplete $\mathcal{R}_{128}$ curve[3] begins its catastrophic mass loss phase at an earlier time than $\mathcal{R}_{64}$. This indicates that the

[3]The reason why this $\mathcal{R}_{128}$ curve, as well as the $\chi_r = 0.5$ and $\chi_r = 0.3$ curves in Figure 4.3, are incomplete is because the PLUTO code got "stuck" in such a way that the simulation would continue running but not progress to the next time step. This problem does not arise when $f > 0$. We do not yet know the cause of these numerical problems, but it may be related to memory usage issues.

lowest resolution ($\mathcal{R}_{64}$) artificially extends the lifetime of the cold gas mass as it does not fully resolve the HD instabilities, which strip the cloud of its cold gas, nor the fragmentation process due to the cooling. For $f = 0.01$, on the other hand, we were able to reach convergence at a resolution of $\mathcal{R}_{128}$ since the result barely changes for the higher resolution of $\mathcal{R}_{256}$. Notice that the lowest resolution ($\mathcal{R}_{64}$) still artificially extends the lifetime of cold gas mass as the low suppression factor does not suppress both the HD instabilities and the fragmentation process to such an extent that they need not be resolved. For $f = 0.02$, we see that the mass curves for all three resolutions are closer together, but, unfortunately, $\mathcal{R}_{128}$ and $\mathcal{R}_{256}$ are not close enough together to declare $f = 0.02$ as a converged simulation. For $f = 0.05$, we can see that the curves are even more tightly packed as the higher suppression factor (almost) fully suppresses the HD instabilities as well as any small-scale structure. Here, convergence has possibly been reached at a resolution of $\mathcal{R}_{64}$. Even though some of our simulations do not seem to be fully converged, the main result of clouds evaporating in the hot corona seems robust, since it holds at all the resolutions that we have investigated.

It should additionally be noted that not only the grid resolution but also the box size will influence the accuracy of the results; when the box size is too small, the cold gas will leave the simulation box before evaporating, leading to completely erroneous results. We have therefore ensured that our simulation box was always large enough such that it retained the cold gas until it evaporated.

4.2.2 Model assumptions

For our simulations, we have assumed that the infalling cloud begins its infall as a perfect sphere. In reality, the cloud probably has a more amorphous shape, but we justify our assumption since the cloud will quickly lose its spherical shape when it falls through and interacts with the hot corona. We have furthermore assumed the hot corona to be isothermal since, in general, the temperature does not strongly vary as a function of $r_{\rm gal}$ (e.g. Kim et al. 2020). In addition, we have assumed that the temperature of the hot gas is equal to the virial temperature, which is justified by models and roughly in agreement with observations (Goulding et al. 2016). We also assume the corona to be in hydrostatic equilibrium (as well as non-rotating) which is not entirely correct since material tends to flow into the CGM from IGM. The corona furthermore loses a small amount of energy due to radiative cooling, while it also gains a bit of energy from the metagalactic UV field (Haardt and Madau 1996; Haardt and Madau 2001; Haardt and Madau 2012). We take this balance between the cooling and heating of the corona roughly into account by utilizing a cooling floor that prevents any gas to cool below a temperature of 2×10^4 K. We also do not allow the corona to cool by using a tracer to restrict the cooling to only the cold and mixed cloud material. We implement the radiative cooling by using the Collisional Ionization Equilibrium (CIE) tables from Sutherland and Dopita 1993, which assumes that all ions are in the ground state and that the medium is optically thin to its own radiation (Dopita and Sutherland 2003). These assumptions are, however, quite crude. Including a more sophisticated chemical network which, for instance, computes the net radiative cooling by solving the equilibrium state of the medium for a given radiation field (Salz et al. 2015) would therefore be more accurate. Incorporating a more complex cooling function and an actual source of heating are thus possible improvements for future work.

We have furthermore adopted a suppression factor f to approximate the suppression of thermal conduction by magnetic fields. This means that we assume the suppression to be an isotropic process even though, in reality, it is anisotropic as the thermal conduction is only suppressed in the direction perpendicular to the magnetic field (Kooij et al. 2021). We again justify this simplification because the magnetic fields in the hot coronae of ETGs are virtually

unknown to date.

We have also neglected the effects of self-gravity even when we increased the cloud mass from $10^5\,\mathrm{M}_\odot$ to $10^6\,\mathrm{M}_\odot$ in section 3.2.3. If self-gravity played an important role, then our results could be inaccurate as the gravitational field may slow down the mass stripping and the breakup of the cloud. A way to quantify the importance of self-gravity, is via the *Jeans mass* which is defined as (Jeans 1902):

$$M_J = \frac{4\pi}{3}\rho_\mathrm{c} R_J^3 = \frac{1}{6}\rho_\mathrm{c}^{-1/2}\left(\frac{15 k_\mathrm{B} T_\mathrm{c}}{4\pi^{1/3} G m_\mathrm{p} \mu_\mathrm{c}}\right)^{3/2}, \tag{4.7}$$

where ρ_c is the density of the cold cloud, k_B the Boltzmann constant, $T_\mathrm{c} = 2\times10^4\,\mathrm{K}$ the temperature of the cold cloud, G the gravitational constant, m_p the proton mass, and $\mu_\mathrm{c} = 0.6$ the mean molecular weight of the cloud. Once $M_\mathrm{c} \sim M_\mathrm{J}$, self-gravity can no longer be ignored. Note that since $M_\mathrm{J} \propto \rho_\mathrm{c}^{-1/2}$, M_J will decrease for clouds that start closer to the galactic center (see Figure 2.5). Because the cloud density for starting radii of r_vir ($\rho_\mathrm{c} \sim 10^{-27}\,\mathrm{g/cm^3}$) and $r_\mathrm{vir}/2$ ($\rho_\mathrm{c} \sim 10^{-26}\,\mathrm{g/cm^3}$) are both so low, we find very high Jeans masses of $M_\mathrm{J} = 1.36\times10^9\,\mathrm{M}_\odot$ and $M_\mathrm{J} = 6.72\times10^8\,\mathrm{M}_\odot$, respectively. This shows that our clouds are all orders of magnitude below M_J. We can therefore safely ignore the effects of self-gravity.

The most important limitation of our model is that we have run our simulations solely in 2D. Our main justification for this is that 3D simulations are computationally too expensive (even when using AMR), which would force us to adopt a lower resolution. Running in 3D would therefore prevent most of our simulations from reaching convergence (see section 4.2.1). The downside with using 2D, however, is that even though we can obtain an estimate of the mass by rescaling the 2D disk to a 3D sphere, we cannot obtain the correct surface area. The reason for this is because the cross section of the rescaled "sphere" corresponds to the cross section of an infinitely long cylinder, whose surface area is equal to that of a one-dimensional "ring" (Grønnow et al. 2018). As a result, less instabilities will form which leads to less mass stripping. 2D simulations therefore underestimate the amount of mixing and, in case of evaporation, overpredict the lifetime of the cloud. This actually works in our favour, since our 2D simulations — which essentially constitutes the upper limit of the cloud's lifetime — have already clearly shown that the cold clouds cannot survive their journey to the galactic center.

Chapter 5

Conclusions

We have built 2D hydrodynamical simulations to numerically investigate the survival of infalling cold ($T_c = 2 \times 10^4$ K) clouds in the hot ($T_{cor} = 6.5 \times 10^6$ K) coronal medium of massive quiescent ETGs. For our model, we have used the average values of the virial mass, virial radius, and coronal temperature of 16 low-redshift ETGs, as well as the mean temperature of the cool absorbers in the COS-LRG sample (Chen et al. 2018; Zahedy et al. 2019). Our setup and simulation parameters are based on the findings of Afruni et al. 2019, who fitted with an analytical model the observational data of the COS-LRG sample. They found that the cool CGM of ETGs can be described by clouds with masses of 10^5 $M_\odot$ that fall in from the virial radius and eventually evaporate in the hot corona. Here we analyze the behaviour of these clouds with our simulations, for which we have varied the cloud metallicity, the starting/infall radius, the initial cloud mass, and the suppression factor (f) for isotropic thermal conduction.

From our results we can draw the following conclusions:

1. In all our simulations, the clouds evaporate in the coronal medium long before reaching the galactic center, thus accounting for the lack of star formation in these quenched galaxies. On average, we find that the clouds have an evaporation time of $\bar{t} = 643$ Myr and travel a distance of $\bar{d} = 63$ kpc (see Figure 3.18), which is significantly smaller than the average virial radius, $r_{vir} = 526$ kpc, of our reference sample of ETGs. These results are also in qualitative agreement with the analytical model of Afruni et al. 2019.

2. The cloud initially loses its cold gas mass at an approximately constant exponential rate, but eventually transitions to a catastrophic mass loss phase as it gets torn apart by HD instabilities and smoothed out by thermal conduction. We find that for a suppression factor larger than $f = 0.05$, the cloud survival time is shorter than ≈ 500 Myr. Therefore, this value of f possibly represents a rough upper limit on the thermal conduction efficiency, otherwise, these clouds would evaporate too quickly to be observable.

3. The analytical model finds an evaporation rate of $\alpha = 1.8^{+0.25}_{-0.26}$ Gyr^{-1} for a cloud of mass 10^5 $M_\odot$ that starts at the virial radius. This value is quite close to the average evaporation rate in our simulations (e.g. $\bar{\alpha}_{sim} = 1.5$ Gyr^{-1} for $f = 0.02$) during the (approximately) constant exponential mass loss phase. This agreement starts to break down, however, when the cold gas in the simulations transitions to its accelerated (catastrophic) mass loss phase, which the analytical model does not take into account.

4. In the analytical model it is assumed that the cold clouds will shrink but still remain perfectly spherical as they fall in towards the galactic center. This means that the radius of the cold cloud will decrease as a function of time. In our simulations, we have computed

the effective size $R_{\rm eff}$ (i.e. the spread of cold gas material along a certain direction) along the x- and y-axis for all our simulations and found that $R_{\rm eff}$ does not just decrease as a function of time. Instead, it exhibits a significantly more complicated behaviour that tends to increase rather than decrease with time. However, despite the significant differences in the shape of the cold cloud, the analytical approximation of the drag force works very well; we find that the velocity profiles of our simulations are in excellent agreement with the analytical velocity profile, especially for a cloud that starts at the virial radius. When we decrease the starting radius to half the virial radius, we find a weaker agreement between the velocities of our simulations and the analytical velocity.

Based on our results, we can suggest a couple of improvements for the analytical model. The first improvement pertains to the mass loss: in the analytical model the cloud loses its cold gas mass at a constant exponential rate, but it never undergoes any catastrophic mass loss which is ultimately responsible for the evaporation of the entire cloud. Instead, the cloud becomes progressively smaller but never actually disappears. This could be improved by implementing a new mass loss function in the analytical model which includes the catastrophic mass loss phase at the end, i.e. at a certain *evaporation time*. In fact, the catastrophic mass loss is so quick that simply setting the cloud mass to zero once the evaporation time has been reached is already a good approximation. The second improvement entails the size of the cloud: the radius of the cloud in the analytical model is determined by the pressure equilibrium which causes the cloud to shrink when it gets closer to the galaxy. Yet, our simulations show that the size of the cloud (measured as the spread in cold gas material) tends to increase as it gets torn apart by HD instabilities. This increase in cloud size leads to an increase in cross section, which in turn may imply that the cloud would be easier to observe via absorption lines (though its density would also be lower). The analytical model is based on the observational data of these clouds around massive ETGs, so incorporating this increase in the cloud size in the analytical model may improve the overall agreement with the observations.

As pointed out in the discussion, we have made some simplifying assumptions while setting up our simulations. It would, therefore, be interesting for future projects to introduce more complexity to our current simulations. First, we have ignored the effects of magnetic fields since they are currently unconstrained in ETGs. Yet, galactic magnetic fields are known to slow down the mixing process by dampening the KH instabilities (e.g. Grønnow et al. 2017; Grønnow et al. 2018) and can have a strong effect on the evaporation, cloud morphology, and momentum transfer between the cloud and the corona (Kooij et al. 2021). In addition, magnetic fields are also responsible for suppressing the thermal conduction. We have approximated this effect by isotropically suppressing the thermal conduction with a global suppression factor f. But, in reality, thermal conduction is anisotropically suppressed in the direction perpendicular to the magnetic field lines (Kooij et al. 2021). It would, therefore, be interesting to include magnetic fields (once more is known about them in ETGs) in future simulations. We have also adopted the Collisional Ionization Equilibrium (CIE) cooling tables from Sutherland and Dopita 1993 to implement radiative cooling for the mixed gas. Cooling plays an important role in slowing down the evaporation of cold gas, yet our assumption of CIE is quite crude. This can be improved by directly calculating the cooling during the simulation (which is required once CIE is not assumed anymore) rather than using the CIE cooling tables. In addition, we have also neglected the effect of heating, which could be implemented in future work. Finally, the simulations should be run in 3D — since our 2D simulations consistently underestimate the amount of mixing — to get more reliable estimates on the mass evolution of these cold gas clouds.

Acknowledgements

This year was a hectic year. But, nevertheless, we persevered! Because of that, I'd like to express my gratitude.

Filippo, despite already supervising another Master's student, you were still willing to take me under your wing. I cannot fathom how busy the life of a professor must be, but in spite of that, you have always been extremely helpful and understanding. Especially toward the end, your feedback has been indispensable in making this thesis more coherent.

Asger, you were the one who made the numerical code do its magic. Whenever I was at sea with trying to get the code up and running, you were always there to help me out. Even towards the end you discovered a mistake in my code that otherwise would have ruined some of my results. Truly, building these simulations would have been impossible without you.

Andrea, my simulations were based on your analytical model. Because of that, your model and thus your help was the theoretical backbone of this thesis. I must admit, my introduction was a mess at first. But in your feedback, you gave me such a clear outline of how I could improve upon it that I suddenly knew how to tackle that behemoth of a chapter.

Roy (a.k.a. Der Hackermann), whenever I was stuck at coding, I could always count on you. I thank you not only for your help but also for being a great asset to my Sesame Credit score (I mean friend, of course). In 2018 we went to Japan together, but South America awaits!

Being in lockdown is not my favourite activity. But it was made bearable thanks to my supportive parents and sister. I actually feel like we got closer together thanks to this pandemic (but don't worry, I'll soon bugger off to Sweden!). Visiting my grandparents every Saturday was also key in keeping me sane. Thank you Pake, for your endless supply of old songs and good sense humour, we're definitely going to listen to The Platters some time soon. And thank you Beppe, for your impeccable cooking skills and your kind-heartedness.

I'd also like to thank the Peregrine high performance computing cluster for ensuring that the simulations would finish before I'd die of old age.

Last but not least, I'd like to thank Sportclub FenF for having taught me discipline through Kyokushin Karate. Without that, I would not have been writing the acknowledgements of a Master's thesis.

Bibliography

Afruni, Andrea et al. (May 2019). "Cool circumgalactic gas of passive galaxies from cosmological inflow". In: *Astronomy & Astrophysics* 625, A11, A11. DOI: 10.1051/0004-6361/201835002. arXiv: 1903.06182 [astro-ph.GA].

Anderson, Michael E. and Joel N. Bregman (May 2010). "Do Hot Halos Around Galaxies Contain the Missing Baryons?" In: *The Astrophysical Journal* 714.1, pp. 320–331. DOI: 10.1088/0004-637X/714/1/320. arXiv: 1003.3273 [astro-ph.CO].

— (Aug. 2011). "Detection of a Hot Gaseous Halo around the Giant Spiral Galaxy NGC 1961". In: *The Astrophysical Journal* 737.1, 22, p. 22. DOI: 10.1088/0004-637X/737/1/22. arXiv: 1105.4614 [astro-ph.CO].

Anderson, Michael E. et al. (Jan. 2013). "Extended Hot Halos around Isolated Galaxies Observed in the ROSAT All-Sky Survey". In: *The Astrophysical Journal* 762.2, 106, p. 106. DOI: 10.1088/0004-637X/762/2/106. arXiv: 1211.5140 [astro-ph.CO].

Armillotta, L. et al. (Nov. 2016). "Efficiency of gas cooling and accretion at the disc-corona interface". In: *Monthly Notices of the Royal Astronomical Society* 462.4, pp. 4157–4170. DOI: 10.1093/mnras/stw1930. arXiv: 1608.06290 [astro-ph.GA].

Armillotta, L. et al. (Sept. 2017). "The survival of gas clouds in the circumgalactic medium of Milky Way-like galaxies". In: *Monthly Notices of the Royal Astronomical Society* 470.1, pp. 114–125. DOI: 10.1093/mnras/stx1239. arXiv: 1608.05416 [astro-ph.GA].

Banda-Barragán, W. E. et al. (Jan. 2016). "Filament formation in wind-cloud interactions - I. Spherical clouds in uniform magnetic fields". In: *Monthly Notices of the Royal Astronomical Society* 455.2, pp. 1309–1333. DOI: 10.1093/mnras/stv2405. arXiv: 1510.05356 [astro-ph.GA].

Begelman, Mitchell C. and Christopher F. McKee (Aug. 1990). "Global Effects of Thermal Conduction on Two-Phase Media". In: *The Astrophysical Journal* 358, p. 375. DOI: 10.1086/168994.

Bennett, Andrew (2006). *Lagrangian Fluid Dynamics*.

Bergeron, J. (Jan. 1986). "The MG II absorption system in the QSO PKS 2128-12 : a galaxy disc/halo with a radius of 65 kpc." In: *Astronomy & Astrophysics* 155, pp. L8–L11.

Binney, James and Michael Merrifield (1998). *Galactic Astronomy*.

Binney, James et al. (Aug. 2009). "Do high-velocity clouds form by thermal instability?" In: *Monthly Notices of the Royal Astronomical Society* 397.4, pp. 1804–1815. DOI: 10.1111/j.1365-2966.2009.15113.x. arXiv: 0902.4525 [astro-ph.GA].

Birnboim, Yuval and Avishai Dekel (Oct. 2003). "Virial shocks in galactic haloes?" In: *Monthly Notices of the Royal Astronomical Society* 345.1, pp. 349–364. DOI: 10.1046/j.1365-8711.2003.06955.x. arXiv: astro-ph/0302161 [astro-ph].

Bland-Hawthorn, Joss et al. (Dec. 2007). "The Source of Ionization along the Magellanic Stream". In: *The Astrophysical Journal Letters* 670.2, pp. L109–L112. DOI: 10.1086/524657. arXiv: 0711.0247 [astro-ph].

Bogdán, Ákos et al. (Aug. 2013). "Hot X-Ray Coronae around Massive Spiral Galaxies: A Unique Probe of Structure Formation Models". In: *The Astrophysical Journal* 772.2, 97, p. 97. DOI: 10.1088/0004-637X/772/2/97. arXiv: 1212.0541 [astro-ph.CO].

Boksenberg, A. and W. L. W. Sargent (Feb. 1978). "The existence of Ca II absorption lines in the spectrum of the quasar 3C 232 due to the galaxy NGC 3067." In: *The Astrophysical Journal* 220, pp. 42–46. DOI: 10.1086/155880.

Bordoloi, R. et al. (Dec. 2011). "The Radial and Azimuthal Profiles of Mg II Absorption around $0.5 < z < 0.9$ zCOSMOS Galaxies of Different Colors, Masses, and Environments". In: *The Astrophysical Journal* 743.1, 10, p. 10. DOI: 10.1088/0004-637X/743/1/10. arXiv: 1106.0616 [astro-ph.CO].

Borthakur, Sanchayeeta et al. (Nov. 2015). "Connection between the Circumgalactic Medium and the Interstellar Medium of Galaxies: Results from the COS-GASS Survey". In: *The Astrophysical Journal* 813.1, 46, p. 46. DOI: 10.1088/0004-637X/813/1/46. arXiv: 1504.01392 [astro-ph.GA].

Bowen, David V. and Doron Chelouche (Jan. 2011). "The Mg II Cross-section of Luminous Red Galaxies". In: *The Astrophysical Journal* 727.1, 47, p. 47. DOI: 10.1088/0004-637X/727/1/47. arXiv: 1011.4947 [astro-ph.CO].

Bregman, Joel N. (Sept. 2007). "The Search for the Missing Baryons at Low Redshift". In: *Annual Review of Astronomy and Astrophysics* 45.1, pp. 221–259. DOI: 10.1146/annurev.astro.45.051806.110619. arXiv: 0706.1787 [astro-ph].

Brüggen, Marcus and Evan Scannapieco (May 2016). "The Launching of Cold Clouds by Galaxy Outflows. II. The Role of Thermal Conduction". In: *The Astrophysical Journal* 822.1, 31, p. 31. DOI: 10.3847/0004-637X/822/1/31. arXiv: 1602.01843 [astro-ph.GA].

Chandrasekhar, Subrahmanyan (1961). *Hydrodynamic and hydromagnetic stability.*

Chen, Hsiao-Wen et al. (Sept. 2018). "Characterizing circumgalactic gas around massive ellipticals at z ~ 0.4 - I. Initial results". In: *Monthly Notices of the Royal Astronomical Society* 479.2, pp. 2547–2563. DOI: 10.1093/mnras/sty1541. arXiv: 1805.07364 [astro-ph.GA].

Cimatti, Andrea et al. (Dec. 2019). "Introduction to Galaxy Formation and Evolution. From Primordial Gas to Present-Day Galaxies". In: *arXiv e-prints*, arXiv:1912.06216, arXiv:1912.06216. arXiv: 1912.06216 [astro-ph.GA].

Cooper, Jackie L. et al. (Sept. 2009). "Starburst-Driven Galactic Winds: Filament Formation and Emission Processes". In: *The Astrophysical Journal* 703.1, pp. 330–347. DOI: 10.1088/0004-637X/703/1/330. arXiv: 0907.4004 [astro-ph.GA].

Cooper, Thomas J. et al. (Oct. 2015). "The Incidence of Low-metallicity Lyman-limit Systems at z ~3.5: Implications for the Cold-flow Hypothesis of Baryonic Accretion". In: *The Astrophysical Journal* 812.1, 58, p. 58. DOI: 10.1088/0004-637X/812/1/58. arXiv: 1505.06210 [astro-ph.GA].

Courant, R. et al. (Jan. 1928). "Über die partiellen Differenzengleichungen der mathematischen Physik". In: *Mathematische Annalen* 100, pp. 32–74. DOI: 10.1007/BF01448839.

Danforth, Charles W. and J. Michael Shull (May 2005). "The Low-z Intergalactic Medium. I. O VI Baryon Census". In: *The Astrophysical Journal* 624.2, pp. 555–560. DOI: 10.1086/429285. arXiv: astro-ph/0501054 [astro-ph].

Dekel, Avishai and Yuval Birnboim (May 2006). "Galaxy bimodality due to cold flows and shock heating". In: *Monthly Notices of the Royal Astronomical Society* 368.1, pp. 2–20. DOI: 10.1111/j.1365-2966.2006.10145.x. arXiv: astro-ph/0412300 [astro-ph].

Dopita, Michael A. and Ralph S. Sutherland (2003). "Collisional Ionization Equilibrium". In: *Astrophysics of the Diffuse Universe*. Berlin, Heidelberg: Springer Berlin Heidelberg, pp. 101–

123. ISBN: 978-3-662-05866-4. DOI: 10.1007/978-3-662-05866-4_5. URL: https://doi.org/10.1007/978-3-662-05866-4_5.

Draine, B. T. and Jr. Giuliani J. L. (June 1984). "Thermal evaporation of spherical clouds - Effects of viscous stresses". In: *The Astrophysical Journal* 281, pp. 690–701. DOI: 10.1086/162146.

Drazin, P. G. (2002). *Introduction to Hydrodynamic Stability*.

Dutton, Aaron A. and Andrea V. Macciò (July 2014). "Cold dark matter haloes in the Planck era: evolution of structural parameters for Einasto and NFW profiles". In: *Monthly Notices of the Royal Astronomical Society* 441.4, pp. 3359–3374. DOI: 10.1093/mnras/stu742. arXiv: 1402.7073 [astro-ph.CO].

F.R.S., Sir William Thomson (1871). "XLVI. Hydrokinetic solutions and observations". In: *The London, Edinburgh, and Dublin Philosophical Magazine and Journal of Science* 42.281, pp. 362–377. DOI: 10.1080/14786447108640585. eprint: https://doi.org/10.1080/14786447108640585. URL: https://doi.org/10.1080/14786447108640585.

Fakhouri, Onsi et al. (Aug. 2010). "The merger rates and mass assembly histories of dark matter haloes in the two Millennium simulations". In: *Monthly Notices of the Royal Astronomical Society* 406.4, pp. 2267–2278. DOI: 10.1111/j.1365-2966.2010.16859.x. arXiv: 1001.2304 [astro-ph.CO].

Fang, Taotao et al. (Jan. 2013). "On the Hot Gas Content of the Milky Way Halo". In: *The Astrophysical Journal* 762.1, 20, p. 20. DOI: 10.1088/0004-637X/762/1/20. arXiv: 1211.0758 [astro-ph.CO].

Ferland, G. J. et al. (July 1998). "CLOUDY 90: Numerical Simulation of Plasmas and Their Spectra". In: *The Publications of the Astronomical Society of the Pacific* 110.749, pp. 761–778. DOI: 10.1086/316190.

Ferziger, Joel and Milovan Peric (Jan. 2002). *Computational Methods for Fluid Dynamics*. Vol. 3. ISBN: 978-3-540-42074-3. DOI: 10.1007/978-3-642-56026-2.

Field, George B. (Aug. 1965). "Thermal Instability." In: *The Astrophysical Journal* 142, p. 531. DOI: 10.1086/148317.

Fielding, Drummond et al. (Apr. 2017). "The impact of star formation feedback on the circumgalactic medium". In: *Monthly Notices of the Royal Astronomical Society* 466.4, pp. 3810–3826. DOI: 10.1093/mnras/stw3326. arXiv: 1606.06734 [astro-ph.GA].

Fraternali, F. and J. J. Binney (May 2008). "Accretion of gas on to nearby spiral galaxies". In: *Monthly Notices of the Royal Astronomical Society* 386.2, pp. 935–944. DOI: 10.1111/j.1365-2966.2008.13071.x. arXiv: 0802.0496 [astro-ph].

Fraternali, F. et al. (Sept. 2004). "Kinematics of the ionised gas in the spiral galaxy NGC 2403". In: *Astronomy & Astrophysics* 424, pp. 485–495. DOI: 10.1051/0004-6361:20040529. arXiv: astro-ph/0405619 [astro-ph].

Fraternali, F. et al. (Feb. 2015). "Galactic hail: the origin of the high-velocity cloud complex C." In: *Monthly Notices of the Royal Astronomical Society* 447, pp. L70–L74. DOI: 10.1093/mnrasl/slu182. arXiv: 1411.4050 [astro-ph.GA].

Fraternali, Filippo (2017). "Gas Accretion via Condensation and Fountains". In: *Gas Accretion onto Galaxies*. Ed. by Andrew Fox and Romeel Davé. Vol. 430, p. 323. DOI: 10.1007/978-3-319-52512-9_14.

Fumagalli, Michele et al. (Jan. 2014). "Confronting Simulations of Optically Thick Gas in Massive Halos with Observations at z = 2-3". In: *The Astrophysical Journal* 780.1, 74, p. 74. DOI: 10.1088/0004-637X/780/1/74. arXiv: 1308.1669 [astro-ph.CO].

Gauthier, Jean-René and Hsiao-Wen Chen (Dec. 2011). "The star formation history of luminous red galaxies hosting Mg II absorbers". In: *Monthly Notices of the Royal Astronomical Society*

418.4, pp. 2730–2735. DOI: 10.1111/j.1365-2966.2011.19668.x. arXiv: 1108.4057 [astro-ph.CO].

Gauthier, Jean-René et al. (Sept. 2009). "The Clustering of Mg II Absorption Systems at z ~0.5 and Detection of Cold Gas in Massive Halos". In: *The Astrophysical Journal* 702.1, pp. 50–62. DOI: 10.1088/0004-637X/702/1/50. arXiv: 0902.3237 [astro-ph.CO].

— (June 2010). "The Incidence of Cool Gas in ~10^{13} M $_{sun}$ Halos". In: *The Astrophysical Journal* 716.2, pp. 1263–1268. DOI: 10.1088/0004-637X/716/2/1263. arXiv: 1004.5378 [astro-ph.CO].

Glidden, Ana et al. (Dec. 2016). "Predominantly Low Metallicities Measured in a Stratified Sample of Lyman Limit Systems at Z=3.7". In: *The Astrophysical Journal* 833.2, 270, p. 270. DOI: 10.3847/1538-4357/833/2/270. arXiv: 1604.02144 [astro-ph.GA].

Godunov, S. K. (1959). "A difference method for numerical calculation of discontinuous solutions of the equations of hydrodynamics." In: *Mat. Sb. (N.S.)* 47(89) (3), pp. 271–306.

Goulding, Andy D. et al. (Aug. 2016). "The MASSIVE Survey. IV. The X-ray Halos of the Most Massive Early-type Galaxies in the Nearby Universe". In: *The Astrophysical Journal* 826.2, 167, p. 167. DOI: 10.3847/0004-637X/826/2/167. arXiv: 1604.01764 [astro-ph.GA].

Grønnow, Asger (2018). *The effect of the Galactic magnetic field on gas accretion.*

Grønnow, Asger et al. (Aug. 2017). "Magnetized High Velocity Clouds in the Galactic Halo: A New Distance Constraint". In: *The Astrophysical Journal* 845.1, 69, p. 69. DOI: 10.3847/1538-4357/aa7ed2. arXiv: 1707.02697 [astro-ph.GA].

Grønnow, Asger et al. (Sept. 2018). "Magnetic Fields in the Galactic Halo Restrict Fountain-driven Recycling and Accretion". In: *The Astrophysical Journal* 865.1, 64, p. 64. DOI: 10.3847/1538-4357/aada0e. arXiv: 1805.03903 [astro-ph.GA].

Gupta, A. et al. (Sept. 2012). "A Huge Reservoir of Ionized Gas around the Milky Way: Accounting for the Missing Mass?" In: *The Astrophysical Journal Letters* 756.1, L8, p. L8. DOI: 10.1088/2041-8205/756/1/L8. arXiv: 1205.5037 [astro-ph.HE].

Haardt, F. and P. Madau (Jan. 2001). "Modelling the UV/X-ray cosmic background with CUBA". In: *Clusters of Galaxies and the High Redshift Universe Observed in X-rays*. Ed. by D. M. Neumann and J. T. V. Tran, p. 64. arXiv: astro-ph/0106018 [astro-ph].

Haardt, Francesco and Piero Madau (Apr. 1996). "Radiative Transfer in a Clumpy Universe. II. The Ultraviolet Extragalactic Background". In: *The Astrophysical Journal* 461, p. 20. DOI: 10.1086/177035. arXiv: astro-ph/9509093 [astro-ph].

— (Feb. 2012). "Radiative Transfer in a Clumpy Universe. IV. New Synthesis Models of the Cosmic UV/X-Ray Background". In: *The Astrophysical Journal* 746.2, 125, p. 125. DOI: 10.1088/0004-637X/746/2/125. arXiv: 1105.2039 [astro-ph.CO].

Harten, A. et al. (1983). "On Upstream Differencing and Godunov-Type Schemes for Hyperbolic Conservation Laws". In: *Siam Review* 25, pp. 53–79.

Helmholtz, Professor (1868). "XLIII. On discontinuous movements of fluids". In: *The London, Edinburgh, and Dublin Philosophical Magazine and Journal of Science* 36.244, pp. 337–346. DOI: 10.1080/14786446808640073. eprint: https://doi.org/10.1080/14786446808640073. URL: https://doi.org/10.1080/14786446808640073.

Huang, Yun-Hsin et al. (Jan. 2016). "Characterizing the chemically enriched circumgalactic medium of ∼38 000 luminous red galaxies in SDSS DR12". In: *Monthly Notices of the Royal Astronomical Society* 455.2, pp. 1713–1727. DOI: 10.1093/mnras/stv2327. arXiv: 1510.01336 [astro-ph.GA].

Huang, Yun-Hsin et al. (Apr. 2021). "A complete census of circumgalactic Mg II at redshift z $\lesssim$ 0.5". In: *Monthly Notices of the Royal Astronomical Society* 502.4, pp. 4743–4761. DOI: 10.1093/mnras/stab360. arXiv: 2009.12372 [astro-ph.GA].

Hubble, E. P. (1936). *Realm of the Nebulae*.

Jeans, J. H. (Jan. 1902). "The Stability of a Spherical Nebula". In: *Philosophical Transactions of the Royal Society of London Series A* 199, pp. 1–53. DOI: 10.1098/rsta.1902.0012.

Jones, T. W. et al. (Dec. 1996). "The Magnetohydrodynamics of Supersonic Gas Clouds: MHD Cosmic Bullets and Wind-swept Clumps". In: *The Astrophysical Journal* 473, p. 365. DOI: 10.1086/178151. arXiv: astro-ph/9606106 [astro-ph].

Kacprzak, Glenn G. et al. (Sept. 2014). "New Perspective on Galaxy Outflows from the First Detection of Both Intrinsic and Traverse Metal-line Absorption". In: *The Astrophysical Journal Letters* 792.1, L12, p. L12. DOI: 10.1088/2041-8205/792/1/L12. arXiv: 1407.4126 [astro-ph.GA].

Keeney, Brian A. et al. (Mar. 2013). "HST/COS Spectra of Three QSOs That Probe the Circumgalactic Medium of a Single Spiral Galaxy: Evidence for Gas Recycling and Outflow". In: *The Astrophysical Journal* 765.1, 27, p. 27. DOI: 10.1088/0004-637X/765/1/27. arXiv: 1301.4242 [astro-ph.CO].

Keeney, Brian A. et al. (May 2017). "Characterizing the Circumgalactic Medium of Nearby Galaxies with HST/COS and HST/STIS Absorption-line Spectroscopy. II. Methods and Models". In: *Astrophysical Journal Supplement Series* 230.1, 6, p. 6. DOI: 10.3847/1538-4365/aa6b59. arXiv: 1704.00235 [astro-ph.GA].

Kereš, Dušan et al. (Oct. 2005). "How do galaxies get their gas?" In: *Monthly Notices of the Royal Astronomical Society* 363.1, pp. 2–28. DOI: 10.1111/j.1365-2966.2005.09451.x. arXiv: astro-ph/0407095 [astro-ph].

Kim, Dong-Woo et al. (Feb. 2020). "Temperature profiles of hot gas in early-type galaxies". In: *Monthly Notices of the Royal Astronomical Society* 492.2, pp. 2095–2118. DOI: 10.1093/mnras/stz3530. arXiv: 1912.06098 [astro-ph.GA].

Klein, Richard I. et al. (Jan. 1994). "On the Hydrodynamic Interaction of Shock Waves with Interstellar Clouds. I. Nonradiative Shocks in Small Clouds". In: *The Astrophysical Journal* 420, p. 213. DOI: 10.1086/173554.

Kooij, Richard et al. (Mar. 2021). "Efficiency of thermal conduction in a magnetized circumgalactic medium". In: *Monthly Notices of the Royal Astronomical Society* 502.1, pp. 1263–1278. DOI: 10.1093/mnras/stab110. arXiv: 2101.04684 [astro-ph.GA].

Krause, G. (Nov. 2019). "Hydrostatic equilibrium preservation in MHD numerical simulation with stratified atmospheres. Explicit Godunov-type schemes with MUSCL reconstruction". In: *Astronomy & Astrophysics* 631, A68, A68. DOI: 10.1051/0004-6361/201936387.

LeVeque, Randall J. (2002). *Finite Volume Methods for Hyperbolic Problems*. Cambridge Texts in Applied Mathematics. Cambridge University Press. DOI: 10.1017/CBO9780511791253.

Li, Anqi et al. (June 2021). "A kinematic analysis of ionized extraplanar gas in the spiral galaxies NGC 3982 and NGC 4152". In: *Monthly Notices of the Royal Astronomical Society* 504.2, pp. 3013–3028. DOI: 10.1093/mnras/stab1043. arXiv: 2104.05736 [astro-ph.GA].

Li, Jiang-Tao et al. (Dec. 2017). "The Circum-Galactic Medium of Massive Spirals. II. Probing the Nature of Hot Gaseous Halo around the Most Massive Isolated Spiral Galaxies". In: *Astrophysical Journal Supplement Series* 233.2, 20, p. 20. DOI: 10.3847/1538-4365/aa96fc. arXiv: 1710.07355 [astro-ph.GA].

Li, Jiang-Tao et al. (Mar. 2018). "Baryon Budget of the Hot Circumgalactic Medium of Massive Spiral Galaxies". In: *The Astrophysical Journal Letters* 855.2, L24, p. L24. DOI: 10.3847/2041-8213/aab2af. arXiv: 1802.09453 [astro-ph.GA].

Lundgren, Britt F. et al. (June 2009). "A Cross-Correlation Analysis of Mg II Absorption Line Systems and Luminous Red Galaxies from the SDSS DR5". In: *The Astrophysical Journal* 698.1, pp. 819–839. DOI: 10.1088/0004-637X/698/1/819. arXiv: 0902.4003 [astro-ph.CO].

Mac Low, Mordecai-Mark et al. (Oct. 1994). "Shock Interactions with Magnetized Interstellar Clouds. I. Steady Shocks Hitting Nonradiative Clouds". In: *The Astrophysical Journal* 433, p. 757. DOI: 10.1086/174685.

Marasco, A. et al. (Nov. 2019). "HALOGAS: the properties of extraplanar HI in disc galaxies". In: *Astronomy & Astrophysics* 631, A50, A50. DOI: 10.1051/0004-6361/201936338. arXiv: 1909.04048 [astro-ph.GA].

Marcolini, A. et al. (Sept. 2005). "The dynamics and high-energy emission of conductive gas clouds in supernova-driven galactic superwinds". In: *Monthly Notices of the Royal Astronomical Society* 362.2, pp. 626–648. DOI: 10.1111/j.1365-2966.2005.09343.x. arXiv: astro-ph/0506645 [astro-ph].

Marinacci, Federico et al. (May 2010). "The mode of gas accretion on to star-forming galaxies". In: *Monthly Notices of the Royal Astronomical Society* 404.3, pp. 1464–1474. DOI: 10.1111/j.1365-2966.2010.16352.x. arXiv: 1001.2446 [astro-ph.GA].

Marinacci, Federico et al. (Aug. 2011). "Galactic fountains and the rotation of disc-galaxy coronae". In: *Monthly Notices of the Royal Astronomical Society* 415.2, pp. 1534–1542. DOI: 10.1111/j.1365-2966.2011.18810.x. arXiv: 1103.5358 [astro-ph.GA].

McCourt, Michael et al. (Feb. 2012). "Thermal instability in gravitationally stratified plasmas: implications for multiphase structure in clusters and galaxy haloes". In: *Monthly Notices of the Royal Astronomical Society* 419.4, pp. 3319–3337. DOI: 10.1111/j.1365-2966.2011.19972.x. arXiv: 1105.2563 [astro-ph.CO].

McCourt, Michael et al. (Feb. 2018). "A characteristic scale for cold gas". In: *Monthly Notices of the Royal Astronomical Society* 473.4, pp. 5407–5431. DOI: 10.1093/mnras/stx2687. arXiv: 1610.01164 [astro-ph.GA].

McGaugh, Stacy S. et al. (Jan. 2010). "The Baryon Content of Cosmic Structures". In: *The Astrophysical Journal Letters* 708.1, pp. L14–L17. DOI: 10.1088/2041-8205/708/1/L14. arXiv: 0911.2700 [astro-ph.CO].

McKee, Christopher F. and Mitchell C. Begelman (Aug. 1990). "Steady Evaporation and Condensation of Isolated Clouds in Hot Plasma". In: *The Astrophysical Journal* 358, p. 392. DOI: 10.1086/168995.

Mignone, A. et al. (May 2007). "PLUTO: A Numerical Code for Computational Astrophysics". In: *Astrophysical Journal Supplement Series* 170.1, pp. 228–242. DOI: 10.1086/513316. arXiv: astro-ph/0701854 [astro-ph].

Mignone, A. et al. (Jan. 2012). "The PLUTO Code for Adaptive Mesh Computations in Astrophysical Fluid Dynamics". In: *Astrophysical Journal Supplement Series* 198.1, 7, p. 7. DOI: 10.1088/0067-0049/198/1/7. arXiv: 1110.0740 [astro-ph.HE].

Miller, Matthew J. and Joel N. Bregman (Feb. 2015). "Constraining the Milky Way's Hot Gas Halo with O VII and O VIII Emission Lines". In: *The Astrophysical Journal* 800.1, 14, p. 14. DOI: 10.1088/0004-637X/800/1/14. arXiv: 1412.3116 [astro-ph.GA].

Mo, Houjun et al. (2010). *Galaxy Formation and Evolution*.

Muller, C. A. et al. (Jan. 1963). "Hydrogène neutre dans la couronne galactique?" In: *Academie des Sciences Paris Comptes Rendus* 257, pp. 1661–1662.

Murray, Stephen D. et al. (Apr. 1993). "Dynamical Instabilities in Two-Phase Media and the Minimum Masses of Stellar Systems". In: *The Astrophysical Journal* 407, p. 588. DOI: 10.1086/172540.

Navarro, Julio F. et al. (Aug. 1995). "Simulations of X-ray clusters". In: *Monthly Notices of the Royal Astronomical Society* 275.3, pp. 720–740. DOI: 10.1093/mnras/275.3.720. arXiv: astro-ph/9408069 [astro-ph].

Nelson, Dylan et al. (Oct. 2020). "Resolving small-scale cold circumgalactic gas in TNG50". In: *Monthly Notices of the Royal Astronomical Society* 498.2, pp. 2391–2414. DOI: 10.1093/mnras/staa2419. arXiv: 2005.09654 [astro-ph.GA].

Nipoti, Carlo and Lorenzo Posti (Sept. 2014). "On the Nature of Local Instabilities in Rotating Galactic Coronae and Cool Cores of Galaxy Clusters". In: *The Astrophysical Journal* 792.1, 21, p. 21. DOI: 10.1088/0004-637X/792/1/21. arXiv: 1404.5638 [astro-ph.GA].

Oosterloo, Tom et al. (Sept. 2007). "The Cold Gaseous Halo of NGC 891". In: *The Astronomical Journal* 134.3, p. 1019. DOI: 10.1086/520332. arXiv: 0705.4034 [astro-ph].

Orlando, S. et al. (Dec. 2005). "Crushing of interstellar gas clouds in supernova remnants. I. The role of thermal conduction and radiative losses". In: *Astronomy & Astrophysics* 444.2, pp. 505–519. DOI: 10.1051/0004-6361:20052896. arXiv: astro-ph/0508638 [astro-ph].

Pezzulli, Gabriele et al. (May 2017). "The angular momentum of cosmological coronae and the inside-out growth of spiral galaxies". In: *Monthly Notices of the Royal Astronomical Society* 467.1, pp. 311–329. DOI: 10.1093/mnras/stx029. arXiv: 1701.01442 [astro-ph.GA].

Pillepich, Annalisa et al. (Feb. 2015). "Building Late-type Spiral Galaxies by In-situ and Ex-situ Star Formation". In: *The Astrophysical Journal* 799.2, 184, p. 184. DOI: 10.1088/0004-637X/799/2/184. arXiv: 1407.7855 [astro-ph.GA].

Planck Collaboration et al. (Sept. 2020). "Planck 2018 results. VI. Cosmological parameters". In: *Astronomy & Astrophysics* 641, A6, A6. DOI: 10.1051/0004-6361/201833910. arXiv: 1807.06209 [astro-ph.CO].

Prochaska, J. Xavier et al. (Mar. 2017). "The COS-Halos Survey: Metallicities in the Low-redshift Circumgalactic Medium". In: *The Astrophysical Journal* 837.2, 169, p. 169. DOI: 10.3847/1538-4357/aa6007. arXiv: 1702.02618 [astro-ph.GA].

Putman, M. E. et al. (Dec. 2011). "Head-tail clouds: drops to probe the diffuse Galactic halo". In: *Monthly Notices of the Royal Astronomical Society* 418.3, pp. 1575–1586. DOI: 10.1111/j.1365-2966.2011.19524.x. arXiv: 1110.0013 [astro-ph.GA].

Putman, M. E. et al. (Sept. 2012). "Gaseous Galaxy Halos". In: *Annual Review of Astronomy and Astrophysics* 50, pp. 491–529. DOI: 10.1146/annurev-astro-081811-125612. arXiv: 1207.4837 [astro-ph.GA].

Rayleigh (1882). "Investigation of the Character of the Equilibrium of an Incompressible Heavy Fluid of Variable Density". In: *Proceedings of the London Mathematical Society* s1-14.1, pp. 170–177. DOI: https://doi.org/10.1112/plms/s1-14.1.170. eprint: https://londmathsoc.onlinelibrary.wiley.com/doi/pdf/10.1112/plms/s1-14.1.170. URL: https://londmathsoc.onlinelibrary.wiley.com/doi/abs/10.1112/plms/s1-14.1.170.

Ryden, Barbara (2016). *Introduction to Cosmology*.

Salz, M. et al. (Apr. 2015). "TPCI: the PLUTO-CLOUDY Interface . A versatile coupled photoionization hydrodynamics code". In: *Astronomy & Astrophysics* 576, A21, A21. DOI: 10.1051/0004-6361/201424330. arXiv: 1502.06517 [astro-ph.IM].

Sancisi, Renzo et al. (June 2008). "Cold gas accretion in galaxies". In: *The Astronomy and Astrophysics Review* 15.3, pp. 189–223. DOI: 10.1007/s00159-008-0010-0. arXiv: 0803.0109 [astro-ph].

Sharma, Prateek et al. (Mar. 2012). "Thermal instability and the feedback regulation of hot haloes in clusters, groups and galaxies". In: *Monthly Notices of the Royal Astronomical Society* 420.4, pp. 3174–3194. DOI: 10.1111/j.1365-2966.2011.20246.x. arXiv: 1106.4816 [astro-ph.CO].

Sparke, Linda S. and III Gallagher John S. (2007). *Galaxies in the Universe: An Introduction*.

Sparre, Martin et al. (Dec. 2020). "Interaction of a cold cloud with a hot wind: the regimes of cloud growth and destruction and the impact of magnetic fields". In: *Monthly Notices of the*

Royal Astronomical Society 499.3, pp. 4261–4281. DOI: 10.1093/mnras/staa3177. arXiv: 2008.09118 [astro-ph.GA].

Spitzer Lyman, Jr. (July 1956). "On a Possible Interstellar Galactic Corona." In: *The Astrophysical Journal* 124, p. 20. DOI: 10.1086/146200.

Spitzer, L. (1962). *Physics of Fully Ionized Gases*.

Springel, V. and C.P. Dullemond (2011). *Numerische Strömungsmechanik*. [Accessed 25-February-2021]. URL: https://www.ita.uni-heidelberg.de/~dullemond/lectures/num_fluid_2011/index.shtml.

Stern, Jonathan et al. (Mar. 2020). "The maximum accretion rate of hot gas in dark matter haloes". In: *Monthly Notices of the Royal Astronomical Society* 492.4, pp. 6042–6058. DOI: 10.1093/mnras/staa198. arXiv: 1909.07402 [astro-ph.GA].

Suresh, Joshua et al. (Mar. 2017). "On the OVI abundance in the circumgalactic medium of low-redshift galaxies". In: *Monthly Notices of the Royal Astronomical Society* 465.3, pp. 2966–2982. DOI: 10.1093/mnras/stw2499. arXiv: 1511.00687 [astro-ph.GA].

Sutherland, Ralph S. and M. A. Dopita (Sept. 1993). "Cooling Functions for Low-Density Astrophysical Plasmas". In: *Astrophysical Journal Supplement Serie* 88, p. 253. DOI: 10.1086/191823.

Tang, Xiaping and Eugene Churazov (July 2018). "Sound wave generation by a spherically symmetric outburst and AGN feedback in galaxy clusters II: impact of thermal conduction". In: *Monthly Notices of the Royal Astronomical Society* 477.3, pp. 3672–3682. DOI: 10.1093/mnras/sty725. arXiv: 1801.03034 [astro-ph.GA].

Taylor, Geoffrey Ingram (1950). "The instability of liquid surfaces when accelerated in a direction perpendicular to their planes. I". In: *Proceedings of the Royal Society of London. Series A. Mathematical and Physical Sciences* 201.1065, pp. 192–196. DOI: 10.1098/rspa.1950.0052. eprint: https://royalsocietypublishing.org/doi/pdf/10.1098/rspa.1950.0052. URL: https://royalsocietypublishing.org/doi/abs/10.1098/rspa.1950.0052.

Thom, Christopher et al. (Oct. 2012). "Not Dead Yet: Cool Circumgalactic Gas in the Halos of Early-type Galaxies". In: *The Astrophysical Journal Letters* 758.2, L41, p. L41. DOI: 10.1088/2041-8205/758/2/L41. arXiv: 1209.5442 [astro-ph.CO].

Toro, E. F. et al. (July 1994). "Restoration of the contact surface in the HLL-Riemann solver". In: *Shock Waves* 4.1, pp. 25–34. DOI: 10.1007/BF01414629.

Toro, E.F. (2009). *Riemann Solvers and Numerical Methods for Fluid Dynamics: A Practical Introduction, Third Edition*.

Tumlinson, J. et al. (Nov. 2011). "The Large, Oxygen-Rich Halos of Star-Forming Galaxies Are a Major Reservoir of Galactic Metals". In: *Science* 334.6058, p. 948. DOI: 10.1126/science.1209840. arXiv: 1111.3980 [astro-ph.CO].

Tumlinson, Jason et al. (Nov. 2013). "The COS-Halos Survey: Rationale, Design, and a Census of Circumgalactic Neutral Hydrogen". In: *The Astrophysical Journal* 777.1, 59, p. 59. DOI: 10.1088/0004-637X/777/1/59. arXiv: 1309.6317 [astro-ph.CO].

Tumlinson, Jason et al. (Aug. 2017). "The Circumgalactic Medium". In: *Annual Review of Astronomy and Astrophysics* 55.1, pp. 389–432. DOI: 10.1146/annurev-astro-091916-055240. arXiv: 1709.09180 [astro-ph.GA].

van Leer, Bram (1979). "Towards the ultimate conservative difference scheme. V. A second-order sequel to Godunov's method". In: *Journal of Computational Physics* 32.1, pp. 101–136. ISSN: 0021-9991. DOI: https://doi.org/10.1016/0021-9991(79)90145-1. URL: https://www.sciencedirect.com/science/article/pii/0021999179901451.

Vieser, W. and G. Hensler (Sept. 2007). "The evolution of interstellar clouds in a streaming hot plasma including heat conduction". In: *Astronomy & Astrophysics* 472.1, pp. 141–153. DOI: 10.1051/0004-6361:20042120. arXiv: 0704.3592 [astro-ph].

Voit, G. Mark (Dec. 2018). "A Role for Turbulence in Circumgalactic Precipitation". In: *The Astrophysical Journal* 868.2, 102, p. 102. DOI: 10.3847/1538-4357/aae8e2. arXiv: 1803.06036 [astro-ph.GA].

Wakker, B. P. (Jan. 1990). PhD thesis. -.

Wakker, B. P. and H. van Woerden (Jan. 1997). "High-Velocity Clouds". In: *Annual Review of Astronomy and Astrophysics* 35, pp. 217–266. DOI: 10.1146/annurev.astro.35.1.217.

Wakker, B. P. et al. (Jan. 2008). "Distances to Galactic High-Velocity Clouds. I. Cohen Stream, Complex GCP, Cloud g1". In: *The Astrophysical Journal* 672.1, pp. 298–319. DOI: 10.1086/523845. arXiv: 0709.1926 [astro-ph].

Werk, Jessica K. et al. (Feb. 2013). "The COS-Halos Survey: An Empirical Description of Metal-line Absorption in the Low-redshift Circumgalactic Medium". In: *Astrophysical Journal Supplement Series* 204.2, 17, p. 17. DOI: 10.1088/0067-0049/204/2/17. arXiv: 1212.0558 [astro-ph.CO].

Werk, Jessica K. et al. (Sept. 2014). "The COS-Halos Survey: Physical Conditions and Baryonic Mass in the Low-redshift Circumgalactic Medium". In: *The Astrophysical Journal* 792.1, 8, p. 8. DOI: 10.1088/0004-637X/792/1/8. arXiv: 1403.0947 [astro-ph.CO].

Werk, Jessica K. et al. (Dec. 2016). "The COS-Halos Survey: Origins of the Highly Ionized Circumgalactic Medium of Star-Forming Galaxies". In: *The Astrophysical Journal* 833.1, 54, p. 54. DOI: 10.3847/1538-4357/833/1/54. arXiv: 1609.00012 [astro-ph.GA].

White, S. D. M. and M. J. Rees (May 1978). "Core condensation in heavy halos: a two-stage theory for galaxy formation and clustering." In: *Monthly Notices of the Royal Astronomical Society* 183, pp. 341–358. DOI: 10.1093/mnras/183.3.341.

White, Simon D. M. and Carlos S. Frenk (Sept. 1991). "Galaxy Formation through Hierarchical Clustering". In: *The Astrophysical Journal* 379, p. 52. DOI: 10.1086/170483.

Williams, Rik J. et al. (Oct. 2005). "Probing the Local Group Medium toward Markarian 421 with Chandra and the Far Ultraviolet Spectroscopic Explorer". In: *The Astrophysical Journal* 631.2, pp. 856–867. DOI: 10.1086/431343. arXiv: astro-ph/0504558 [astro-ph].

Wotta, Christopher B. et al. (Feb. 2019). "The COS CGM Compendium. II. Metallicities of the Partial and Lyman Limit Systems at $z \lesssim 1$". In: *The Astrophysical Journal* 872.1, 81, p. 81. DOI: 10.3847/1538-4357/aafb74. arXiv: 1811.10654 [astro-ph.GA].

Zahedy, Fakhri S. et al. (Apr. 2019). "Characterizing circumgalactic gas around massive ellipticals at $z \sim 0.4$ - II. Physical properties and elemental abundances". In: *Monthly Notices of the Royal Astronomical Society* 484.2, pp. 2257–2280. DOI: 10.1093/mnras/sty3482. arXiv: 1809.05115 [astro-ph.GA].

Zhang, Zong-Xian (2016). *Rock Fracture and Blasting. Theory and Applications.*

Zhu, Guangtun et al. (Apr. 2014). "The large-scale distribution of cool gas around luminous red galaxies". In: *Monthly Notices of the Royal Astronomical Society* 439.3, pp. 3139–3155. DOI: 10.1093/mnras/stu186. arXiv: 1309.7660 [astro-ph.CO].

Appendix A

Source code

Listing A.1: Setup of the initial- and boundary conditions (init.c).

```
#include "pluto.h"
/* ********************************************************************* */
void Init (double *us, double x1, double x2, double x3)
/*
 *
 ********************************************************************* */
{
  double rc = g_inputParam[RCLOUD]; // cloud radius in kpc
  double Mvir = pow(10, g_inputParam[M_VIR]); // 10^{13.3} virial mass in Msun
  double rvir = g_inputParam[R_VIR]; // virial radius in kpc
  double r0 = g_inputParam[R0];   // the smallest considered radius of halo in kpc
  double c = g_inputParam[concentration]; // the concentration (unitless)
  double s = g_inputParam[steepness]; // steepness of total dens. profile (unitless)
  double T_H = g_inputParam[TEMP_H]; // temperature of hot corona, i.e. halo in K
  double T_C = g_inputParam[TEMP_C]; // temperature of cold cloud
  double ne_0 = g_inputParam[NE_0]; // normalized gas density in cm^-3 for lowest point at z=10kpc
  double mu = g_inputParam[MU];   // mean molecular weight in amu
  double G = g_inputParam[GRAV];   // grav. constant in cgs units

  // Calculate distance from cloud center
  double x = x1 - g_inputParam[CLOUD_CENTERX1];
  double y = x2 - g_inputParam[CLOUD_CENTERX2];
  double z = x3 - g_inputParam[CLOUD_CENTERX3];

  double CurRad = sqrt(EXPAND(x*x , + y*y , + z*z)); //set radius with the cloud center as origin
  double rs = rvir/c;  // compute scale radius in kpc

  /* Perform calculations */
  double rho_0 = Mvir / (4 * CONST_PI*pow(rs, 3.0) * (log(1 + rvir/rs) - rvir/rs / (1 + rvir/rs))) *
      4.04641863e-8; // in amu/cm^3
  double phi_0 = -4 * CONST_PI * G * rho_0 * pow(rs, 3.0)/r0 * log(1+r0/rs) * 1.5925712e19 / (UNIT_VELOCITY
       * UNIT_VELOCITY); // in code units (not in cm^2/s^2)
  double ne_halo = ne_0 * exp(- mu * CONST_mp / (CONST_kB * T_H) * UNIT_VELOCITY * UNIT_VELOCITY * (
      BodyForcePotential(x1, x2, x3) - phi_0)); // electron dens. profile halo (cm^-3)
  double nhalo = 2.1 * ne_halo; // dens. profile of corona in cm^-3

  us[PRS] = nhalo * T_H / KELVIN; // pressure according to ideal gas law in code units

  double n_cl = nhalo * T_H / T_C; // dens. profile of cloud assuming pressure equilibrium (cm^-3)
  double n_tot = nhalo + 0.5*(n_cl - nhalo) * (1 - tanh(s * (CurRad/rc - 1))); // density profile of halo +
       cloud (cm^-3)

  double ZRad = rc / s * atanh((n_cl - 3*nhalo)/(n_cl - nhalo)) + rc; // Radius at which metallicity
      switches (radius at which the dens. is twice the halo dens.)
  //Set cloud tracer
  if (CurRad < rc)
  {
     us[TRC] = 1.0;
```

```
  }
  else
  {
      us[TRC] = 0.0;
  }
    //Set second tracer where only within it cooling can occur
  if (CurRad < 1.3*rc)
  {
      us[TRC+1] = 1.0;
  }
  else
  {
      us[TRC+1] = 0.0;
  }
  // Set third tracer for different metallicity for cloud and halo
  if (CurRad < ZRad)
  {
      us[TRC+2] = 0.05;
  }
  else
  {
      us[TRC+2] = 0.3;
  }

  us[RHO] = mu * n_tot; // dens. in code units since rho=mp g/cm^3, i.e. mp/rho = 1 so we can leave it out

  // No initial velocities
  us[VX1] = 0.0;
  us[VX2] = 0.0;
  us[VX3] = 0.0;

  g_smallDensity = 1.e-8; // set global floor for density
  g_smallPressure = 1.e-8; // set global floor for pressure
}

void UserDefBoundary (const Data *d, RBox * box, int side, Grid *grid)
/*
 * Sets inflow boundary condition at the top boundary (side == X2_END)
 * and the stellar wind region when side == 0.
 *
 *********************************************************************** */
{
  int  i, j, k, nv;
  double *x1, *x2, *x3;
  // define constants
  double rc = g_inputParam[RCLOUD]; // cloud radius in kpc (for y_core = 19 kpc)
  double Mvir = pow(10, g_inputParam[M_VIR]);   // 10^{13.3} virial mass in Msun
  double rvir = g_inputParam[R_VIR]; // virial radius in kpc
  double r0 = g_inputParam[R0];   // the smallest considered radius of halo in kpc
  double c = g_inputParam[concentration]; // the concentration (unitless)
  double s = g_inputParam[steepness]; // steepness of total dens. profile (unitless)
  double T_H = g_inputParam[TEMP_H]; // temperature of hot corona, i.e. halo in K
  double T_C = g_inputParam[TEMP_C]; // temperature of cold cloud
  double ne_0 = g_inputParam[NE_0]; // normalized gas density in cm^-3 for lowest point at z=10kpc
  double mu = g_inputParam[MU];   // mean molecular weight in amu
  double G = g_inputParam[GRAV];   // grav. constant in cgs units

  double rs = rvir/c;  // compute scale radius in kpc
  double rho_0 = Mvir / (4 * CONST_PI*pow(rs, 3.0) * (log(1 + rvir/rs) - rvir/rs / (1 + rvir/rs))) *
       4.04641863e-8; // in amu/cm^3
  double phi_0 = -4 * CONST_PI * G * rho_0 * pow(rs, 3.0)/r0 * log(1+r0/rs) * 1.5925712e19 / (UNIT_VELOCITY
        * UNIT_VELOCITY); // in code units (not in cm^2/s^2)

  x1 = grid->xgc[IDIR]; // call x1 coordinates from the grid along x1 direction
  x2 = grid->xgc[JDIR]; // Height, use in loop as y=x2[j]
  x3 = grid->xgc[KDIR];

  BodyForcePotential(-2.e7, grid[JDIR].CoM, 0); // pretending its a global value
```

```
  /* Set floorlevel for density and pressure */
  if (side == 0){ // control the solution inside the computational domain
     TOT_LOOP(k,j,i){
        if (d->Vc[RHO][k][j][i] < g_smallDensity) {d->Vc[RHO][k][j][i] = g_smallDensity;} // set limit on
            smallest allowed density
        if (d->Vc[PRS][k][j][i] < g_smallPressure) {d->Vc[PRS][k][j][i] = g_smallPressure;} // set limit
            on smallest allowed pressure
        if (d->Vc[TRC][k][j][i] < 0.0) {d->Vc[TRC][k][j][i] = 0.0;} // set minimum value of tracer at 0
        if (d->Vc[TRC][k][j][i] > 1.0) {d->Vc[TRC][k][j][i] = 1.0;} // cap tracer at a maximum value of 1
        if (d->Vc[TRC+1][k][j][i] < 0.0) {d->Vc[TRC+1][k][j][i] = 0.0;} // set negative 2nd tracer at 0
        if (d->Vc[TRC+1][k][j][i] > 1.0) {d->Vc[TRC+1][k][j][i] = 1.0;} // cap 2nd tracer at max val of 1
        if ((d->Vc[TRC+2][k][j][i] < 0.03) && (d->Vc[TRC][k][j][i] < 0.1)){d->Vc[TRC+2][k][j][i] = 0.3;}
            // only replace metallicity in corona.
     }
  }

  if (side == X2_BEG){ /* -- X2_BEG boundary -- */
    double vx1 = d->Vc[VX1][0][JBEG][0];  // copy velocities inside domain
    double vx2 = d->Vc[VX2][0][JBEG][0];
    X2_BEG_LOOP(k,j,i)
    {
        double ne_halo = ne_0 * exp(- mu * CONST_mp / (CONST_kB * T_H) * UNIT_VELOCITY * UNIT_VELOCITY * (
            BodyForcePotential(0.0, x2[j], 0.0) - phi_0)); // electron dens. profile in cm^-3
        double nhalo = 2.1 * ne_halo; // dens. profile of corona in cm^-3
        d->Vc[RHO][k][j][i] = mu * nhalo;
        d->Vc[VX1][k][j][i] = vx1;
        d->Vc[VX2][k][j][i] = vx2;
        d->Vc[PRS][k][j][i] = nhalo * T_H / KELVIN;
        d->Vc[TRC][k][j][i] = 0.0;
        d->Vc[TRC+1][k][j][i] = 0.0;
        d->Vc[TRC+2][k][j][i] = 0.3; // change border of coronal metallicity to 0.3 solar metallicity
        d->Vc[RHO][k][j][i], d->Vc[PRS][k][j][i], x1[i], x2[j]);
    }
  }
  if (side == X2_END){ /* -- X2_END boundary -- */
    double vx1 = d->Vc[VX1][0][JEND][0]; // copy velocities inside domain
    double vx2 = d->Vc[VX2][0][JEND][0];
    X2_END_LOOP(k,j,i)
    {
        double ne_halo = ne_0 * exp(- mu * CONST_mp / (CONST_kB * T_H) * UNIT_VELOCITY * UNIT_VELOCITY * (
            BodyForcePotential(0.0, x2[j], 0.0) - phi_0)); // electron dens. profile in cm^-3
        double nhalo = 2.1 * ne_halo; // dens. profile of corona in cm^-3
        d->Vc[RHO][k][j][i] = mu * nhalo;
        d->Vc[VX1][k][j][i] = vx1;
        d->Vc[VX2][k][j][i] = vx2;
        d->Vc[PRS][k][j][i] = nhalo * T_H / KELVIN;
        d->Vc[TRC][k][j][i] = 0.0;
        d->Vc[TRC+1][k][j][i] = 0.0;
        d->Vc[TRC+2][k][j][i] = 0.3; // change border of coronal metallicity to 0.3 solar metallicity
    }
  }
}

double BodyForcePotential(double x1, double x2, double x3)
/*
 Computes NFW potential as function of height x2
 */
{
    static double dist = 0.0; // initial value of dist. remembers it using static even if you close the
        function.
    if (x1 < -2.e6)
    {
        dist = x2;
        return 0.0;
    }
    else
    {
        x2 += dist; // subtract distance cloud has travelled to ensure you stay in the cloud frame
        double Mvir = pow(10, g_inputParam[M_VIR]);   // 10^{13.3} virial mass in Msun
```

```
        double rvir = g_inputParam[R_VIR]; // virial radius in kpc
        double c = g_inputParam[concentration]; // the concentration (unitless)
        double G = g_inputParam[GRAV];  // grav. constant in cgs units
        double rs = rvir/c;  // scale radius in kpc

        /* Perform calculations */
        double rho_0 = Mvir / (4 * CONST_PI*pow(rs, 3.0) * (log(1 + rvir/rs) - rvir/rs / (1 + rvir/rs))) *
             4.04641863e-8; // in amu/cm^3
        return - 4 * CONST_PI * G * rho_0 * pow(rs, 3.0) / x2 * log(1 + x2/rs) * 1.5925712e19 / (
             UNIT_VELOCITY * UNIT_VELOCITY); //NFW pot. in code units (not cm^2 /s^2)
    }
}
```

Listing A.2: Defining the parameters used in init.c for the calculations, the grid parameters, the type of Riemann solver, and the duration and output frequency of the simulation (pluto.ini).

```
[Grid]
X1-grid   1    -10.0      40     u    10.0
X2-grid   1     506     80     u    546
X3-grid   1     0         1       u    1.0

[Chombo Refinement]
Levels          6
Ref_ratio       2 2 2 2 2 2 2
Regrid_interval 2 2 2 2 2 2
Refine_thresh   0.7
Tag_buffer_size 3
Block_factor    8
Max_grid_size   32
Fill_ratio      0.9

[Time]
CFL             0.4
CFL_max_var     1.1
tstop           1.2
first_dt        1.e-6

[Solver]
Solver       hllc

[Boundary]
X1-beg       outflow
X1-end       outflow
X2-beg       userdef
X2-end       userdef
X3-beg       outflow
X3-end       outflow

[Chombo HDF5 output]
Checkpoint_interval 5.e-3 0
Plot_interval       5.e-3 0

[Parameters]
CLOUD_CENTERX1           0.0
CLOUD_CENTERX2           526
CLOUD_CENTERX3           0.0
RCLOUD                   0.7112
M_VIR                    13.3
R_VIR                    526
R0                       10
concentration            6.9
steepness                10
TEMP_H                   6.5e6
TEMP_C                   2e4
NE_0                     6e-3
MU                       0.6
GRAV                     6.6743e-8
```

Listing A.3: Specifying the geometry, number of dimensions, type of interpolation, whether it should include effects like cooling or thermal conduction etc. (definitions.h).

```
#define PHYSICS                     HD
#define DIMENSIONS                  2
#define COMPONENTS                  2
#define GEOMETRY                    CARTESIAN
#define BODY_FORCE                  POTENTIAL
#define FORCED_TURB                 NO
#define COOLING                     TABULATED
#define RECONSTRUCTION              LINEAR
#define TIME_STEPPING               CHARACTERISTIC_TRACING
#define DIMENSIONAL_SPLITTING       NO
#define NTRACER                     2
#define USER_DEF_PARAMETERS         14

/* -- physics dependent declarations -- */
#define EOS                         IDEAL
#define ENTROPY_SWITCH              SELECTIVE
#define THERMAL_CONDUCTION          EXPLICIT
#define VISCOSITY                   NO
#define ROTATING_FRAME              NO

/* -- user-defined parameters (labels) -- */
#define CLOUD_CENTERX1              0
#define CLOUD_CENTERX2              1
#define CLOUD_CENTERX3              2
#define RCLOUD                      3
#define M_VIR                       4
#define R_VIR                       5
#define R0                          6
#define concentration               7
#define steepness                   8
#define TEMP_H                      9
#define TEMP_C                      10
#define NE_0                        11
#define MU                          12
#define GRAV                        13

/* [Beg] user-defined constants (do not change this line) */
#define INITIAL_SMOOTHING           NO
#define INTERNAL_BOUNDARY           YES
#define CHAR_LIMITING               YES
#define SHOCK_FLATTENING            MULTID
#define UNIT_LENGTH                 (1.e3*CONST_pc)
#define CHOMBO_REF_VAR              RHO
/* [End] user-defined constants (do not change this line) */
```

Listing A.4: Bilinear interpolation for the cloud metallicity used for the cooling (radiat.c).

```
 int Z_status = 0 ;//0: Metallicity OK use bilinear interp, 1: Z lower than min Z, assume Z=Z_min and don'
     t interpolate in Z, 2: Z greater than max Z, assume Z=Z_max and don't interpolate in Z
 double *L_tab_loZ, *L_tab_hiZ;     // Declare them as double*
 double Z_max = 0.3; // Max metallicity of 30% solar
 double Z_min = 0.03; // Minimum metallicity of 3% solar
 double Z_mid = 0.1; // Middle metallicity of 10% solar
 double Z_hi, Z_lo;
 //define other variables needed for metallicity here, e.g. Z_max, Z_min, etc.
 //here v[TRACER_Z] is the tracer that holds the metallicity in solar units

 if (v[TRACER_Z] > Z_max) Z_status = 2; //too high
 else if (v[TRACER_Z] > Z_mid) //between Z_mid and Z_max
 {
    Z_hi = Z_max;
    Z_lo = Z_mid;
    L_tab_loZ = L_tab_10; //Whatever table corresponds to middle Z
    L_tab_hiZ = L_tab_30; //Whatever table corresponds to max Z
 }
 else if (v[TRACER_Z] > Z_min) //between Z_min and Z_mid
```

```
  {
     Z_hi = Z_mid;
     Z_lo = Z_min;
     L_tab_loZ = L_tab_3; //Whatever table corresponds to min Z
     L_tab_hiZ = L_tab_10; //Whatever table corresponds to middle Z
     //Same as above but max --> mid, mid --> min
  }
  else Z_status = 1; //too low
  double dZ = Z_hi - Z_lo;
/* ----------------------------------------------
    Compute r.h.s
   ---------------------------------------------- */
  dT      = T_tab[khi] - T_tab[klo];
  if (Z_status == 1) scrh = L_tab_3[klo]*(T_tab[khi] - T)/dT + L_tab_3[khi]*(T - T_tab[klo])/dT; //linear
      interpolation in T using Z_min table
  else if (Z_status == 2) scrh = L_tab_30[klo]*(T_tab[khi] - T)/dT + L_tab_30[khi]*(T - T_tab[klo])/dT; //
      linear interpolation in T using Z_max table
  else
  {
     //Bilinear interpolation in T and Z, this is basically just doing two interpolations, first in T then
          in Z
     double L_loZ = L_tab_loZ[klo]*(T_tab[khi] - T)/dT + L_tab_loZ[khi]*(T - T_tab[klo])/dT; //
         interpolation in T at low Z (similar formula to the one above for scrh)
     double L_hiZ = L_tab_hiZ[klo]*(T_tab[khi] - T)/dT + L_tab_hiZ[khi]*(T - T_tab[klo])/dT; //
         interpolation in T at high Z
     scrh    = L_loZ*(Z_hi - v[TRACER_Z])/dZ + L_hiZ*(v[TRACER_Z] - Z_lo)/dZ; //interpolation in Z
  }

  rhs[RHOE] = -scrh*v[RHO]*v[RHO];

  scrh      = UNIT_DENSITY/(CONST_amu*mu);
  rhs[RHOE] *= E_cost*scrh*scrh;
}
```

Listing A.5: Calculating the center of mass velocity for the comoving grid (AMR.cpp).

```
#ifdef COMOVING_FRAME
  if (a_level == 0) //If on the base level (so that all levels are synchronized)
  {
    double CenterOfMassVel = 0.0; // if not m_restartComoving or if timestep larger than first timestep,
        proceed with calculation
    if ((!m_RestartComoving) && (m_cur_step > 0)) // if statement to ensure that CoM is not calculated for
        the first timestep (or first timestep of restart)
    {
    //Loop over levels to calculate center of mass velocity on this CPU
    double RhovAllLevels = 0;
    double MassAllLevels = 0;
    for (int l = 0 ; l <= m_finest_level; l++)
    {
      //Get center of mass velocity numerator and denominator for the cells on this level
      double Rhov = 0.0; // initialize value
      double Mass = 0.0;
      m_amrlevels[l]->GetCenterOfMassVel(Rhov, Mass); // Access void data via pointer
      //Add to center of mass velocity numerator and denominator
      RhovAllLevels += Rhov;
      MassAllLevels += Mass;
    }
    //Add together the center of mass velocity numerator and denominator from all CPUs
    double RhovAllLevels_global = 0.0;
    double MassAllLevels_global = 0.0;

    int red = MPI_Allreduce(&RhovAllLevels, &RhovAllLevels_global, 1, MPI_DOUBLE, MPI_SUM, Chombo_MPI::comm
        ); // add together mass velocity here
    if (red != MPI_SUCCESS) MayDay::Error("sorry, but I had a communication error on calculating integral
        rho*v");
    red = MPI_Allreduce(&MassAllLevels,&MassAllLevels_global, 1, MPI_DOUBLE, MPI_SUM, Chombo_MPI::comm); //
         add together total cloud mass here
    if (red != MPI_SUCCESS) MayDay::Error("sorry, but I had a communication error on calculating total
        cloud mass");
```

```
    CenterOfMassVel = RhovAllLevels_global / MassAllLevels_global; // num / denom
    }

    //If restarting set up comoving grid
    if (m_RestartComoving)
    {
      for (int l = 0; l <= m_finest_level; l++)
      {
        m_amrlevels[l]->SetComovingFrame(m_cur_time, m_t_prev);
      }
      m_t_prev = 0.0;
    }
    else if (m_t_prev > 0.0) //Not restarting and not on first time step
    {
      //Request that the cloud's center of mass velocity be subtracted from cells on each level when next
          updated to change into the cloud's rest frame
      for (int l = 0 ; l <= m_finest_level; l++) // l means it loops over every grid level
      {
        m_amrlevels[l]->SubtractVelocity(CenterOfMassVel, m_t_prev);
      }
    }
    m_RestartComoving = false;
    m_t_prev = m_cur_time;
  }
#endif //COMOVING_FRAME
```

Listing A.6: The three main functions used for the comoving frame (LevelPluto.cpp).

```
void LevelPluto::GetCenterOfMassVel(double& Rhov, double& Mass, LevelData<FArrayBox>& a_split_tags)
{
  double TotRhov = 0.0; //numerator
  double TotMass = 0.0; //denominator

  //Loop over patches
  for (DataIterator dit = m_grids.dataIterator(); dit.ok(); ++dit)
  {
    int k, j, i, nv;
    double*** UU[NVAR];
    FArrayBox& curU = m_U[dit];
    Grid* grid = m_structs_grid[dit].getGrid();

    IBEG = grid->lbeg[IDIR]; IEND = grid->lend[IDIR];
    JBEG = grid->lbeg[JDIR]; JEND = grid->lend[JDIR];
    KBEG = grid->lbeg[KDIR]; KEND = grid->lend[KDIR];

    NX1 = grid->np_int[IDIR];
    NX2 = grid->np_int[JDIR];
    NX3 = grid->np_int[KDIR];

    NX1_TOT = grid->np_tot[IDIR];
    NX2_TOT = grid->np_tot[JDIR];
    NX3_TOT = grid->np_tot[KDIR];

    for (nv = 0; nv < NVAR; nv++){
      UU[nv] = ArrayMap(NX3_TOT, NX2_TOT, NX1_TOT, curU.dataPtr(nv));
    }

    FArrayBox& split_tags = a_split_tags[dit];
    double ***splitcells = ArrayBoxMap(KBEG, KEND, JBEG, JEND, IBEG, IEND, split_tags.dataPtr(0));
    //Loop over cells in patch
    DOM_LOOP(k,j,i)
    {
     if (splitcells[k][j][i] >= 0.5) //Cell is not split
     {
        double Tracer_mass = UU[TRC_cloud][k][j][i] * m_dx*m_dx; // make sure u multiply with m_dx*m_dx
            when in 2D (and m_dx*m_dx*m_dx in 3D)
        double vel = UU[MX2][k][j][i] / UU[RHO][k][j][i];
        TotRhov += Tracer_mass * vel; // momentum in terms of tracer mass (so m_trac * v)
        TotMass += Tracer_mass; // total mass using tracer mass
```

```
    }
   }

   //Deallocate memory from UU array
   for (nv = 0; nv < NVAR; nv++) FreeArrayMap(UU[nv]);
  }
  Rhov = TotRhov;
  Mass = TotMass;
}

void LevelPluto::SubtractVelocity(double vel, double t_prev)
{
  m_VelUpdated = false; //Tell the step function that frame velocity should be changed
  //Update distance that cloud center of mass has travelled, i.e. the distance that the frame has shifted
      along y
  m_vel = vel; // velocity variation in the frame
  m_dist += m_RefFrameVelocity * (g_time - t_prev); // Distance the cloud has travelled in halo frame (use
      reference frame velocity) Using S=v *Delta t
  m_RefFrameVelocity += m_vel; // Add velocity variation to get total velocity

  //Update log file if on the root process and base level
  if ((prank == 0) && (m_level == 0)) // prank=0 mean it only does this on 1 single processor (root
      processor); m_level=0 means it only does it for the base grid
  {
    FILE* f = fopen("framevel.dat", "a"); // outputs total change in velocity and distance travelled (
        needed for analysis and when you want to restart sim) (a means append)
    if (f == NULL) // quits if file is deleted (FILE* means its a pointer, if NULL its pointing to nothing)
    {
      pout() << "Could not open framevel.dat file for writing." << endl;
      QUIT_PLUTO(1);
    }
    //Output current time, reference frame velocity and distance travelled
    fprintf(f, "%.17g %.17g %.17g\n", g_time, m_RefFrameVelocity, m_dist);
    fclose(f);
  }
}

void LevelPluto::SetComovingFrame(double curtime, double& t_prev)
{
  m_RefFrameVelocity = 0.0;
  FILE *file;
  bool DefaultInit = false;
  if (curtime > 0.0) //Restarting from old run, read previous values
  {
    if (file = fopen("framevel.dat", "r")) // r means read
    {
      double time =0.0;
      double vel =0.0;
      double dist =0.0;
      double p_time =0.0;
      double p_vel =0.0;
      double p_dist =0.0;

      while (fscanf(file, "%lf %lf %lf\n", &time, &vel, &dist)!=EOF) {

          if (time> curtime) {           //
              m_RefFrameVelocity = p_vel; // p_vel is what you read from the previous line of file
              m_dist = p_dist; // m_ means youre using something outside the class (global val.)
              t_prev = p_time; // not really needed, but it's there for consistency
              break; // stop reading lines (exists the while loop)
        }

      p_time = time;
      p_vel = vel;
      p_dist = dist;

      }
      fclose(file);
      //Output values used for restart
```

```
    if (prank == 0) pout() << "time, t_prev, framevel, framedist" << curtime << ", " << t_prev << ", " <<
        m_RefFrameVelocity << ", " << m_dist << endl;
   }
   else
   {
    pout() << "WARNING: File framevel.dat not found for restart." << endl;
    DefaultInit = true;
   }
  }
  else DefaultInit = true;
  if (DefaultInit) //Not restarting, use default values
  {
   m_RefFrameVelocity = 0.0;
   m_dist = 0.0;
   t_prev = 0.0;
  }
}
```